ISSN:2661-4448(online)
2661-443X(print)
Volume 3 No.1 2021

MECHANICAL ENGINEERING SCIENCE

VISER
www.viserdata.com

COMPANY INTRODUCTION

Viser Technology Pte. Ltd. was founded in Singapore with branch offices in both Hebei and Chongqing, China. Viser focuses on publishing scientific and technological journals and books that promote the exchange of scientific and technological findings among the research community and around the globe. Despite being a young company, Viser is actively connecting with well-known universities, research institutes, and indexation database, and has already established a stable collaborative relationship with them. We also have a group of experienced editors and publishing experts who are dedicated to publishing high-quality journal and book contents. We offer the scholars various academic journals covering a variety of subjects and we are committed to reducing the hassles of scholarly publishing. To achieve this goal, we provide scholars with an all-in-one platform that offers solutions to every publishing process that a scholar needs to go through in order to show their latest finding to the world.

Mechanical Engineering Science

VISER

Publisher: Viser Technology Pte. Ltd.

ISSN: 2661-4448 (online)

2661-443X (print)

Frequency: Semi-annual

Add.:21 Woodlands Close, #08-18,

Primz Bizhub SINGAPORE (737854)

https://www.viserdata.com/

Mechanical Engineering Science

Volume 3 No.1 (2021)

CONTENTS

Mechanical Analysis for Two-layered Ultrahigh Pressure Apparatus with Interlayer Pressure 1

Mengjun ZHAO, Pengchen ZHU, Zan LIU, Chao KANG

Research on Influence Mechanism of Transmission Accuracy for Harmonic Drive Mechanism Considering Multi-factor Coupling 6

Peng ZHAO, Shuang ZHANG, Yang LIU

Theoretical and Experimental Study on The Speed-up of Freight Train with Mixed Marshaling of Light and Heavy Vehicle 12

Xing ZHANG, Li LI, Dabin CUI, Yaodong FU, Haiyang GUO

Research on Leak Location of Liquid-filled Pipe Based on Frequency Dispersion Characteristics 19

Lijun XIONG, Ping LU, Yun YANG, Li LI

Wheel Profile Optimization of Speed-up Freight Train Based on Multi-population Genetic Algorithm 28

Yaodong FU, Dabin CUI, Pengcheng LEI, Xing ZHANG, Jingkang PENG

Embedment Effect on Eliminating Damage of CFRP Pull-riveting Process by Simulation Study 39

Yiqi WANG, Zhiwei CONG, Guang XIAO, Yongjie BAO, Hang GAO

Influence of Curve Geometric Parameters on Curving Performance of Sub-frame Radial Bogie 50

Chunlei YANG, Yunhua HUANG, Junjun DING

Deformation Analysis and Fixture Design of Thin-walled Cylinder in Drilling Process Based on TRIZ Theory 57

Fulin WANG, Bo SHENG , Yongwen WU, Jiawang LI, Zhou XU, Zhaoxia ZHU

VISER

Viser Technology Pte. Ltd.
Mechanical Engineering Science
DOI: 10.33142/mes.v3i1.4330

Research Article Open Access

Mechanical Analysis for Two-layered Ultrahigh Pressure Apparatus with Interlayer Pressure

Mengjun ZHAO[1]*, Pengchen ZHU[1], Zan LIU[1], Chao KANG[1]

1 School of Mechanical Engineering, Jiangsu University of Science and Technology, Zhenjiang 212003, China

***Corresponding Author:** Mengjun ZHAO, Ph.D., E-mail: z_mj_2005@163.com*

Abstract:
To improve the bearing pressure capacity of ultrahigh pressure apparatus, the internal autofrettaged cylinder with interlayer pressure (ACCIP) is introduced, and the analytical model for the ACCIP structure and its derivation are presented as well. Calculation showed that the ACCIP method enhance bearing pressure of the apparatus obviously; optimization results revealed that under the working pressure p_w=1.07σ_s and different radius ratios, the ACCIP method can keep the apparatus in deformed-elastically state; And when the p_w=1.07σ_s, the minimum radius ratio was approximate 3.29, in this case, no yielding happened. The above results demonstrate that the ACCIP method is a promising technique to improve the bearing pressure of ultrahigh pressure apparatus, and the analytical model for the ACCIP method is also reasonable. In addition, the minimum radius ratio ro/ri under randomly specified workload can be **Fig.**d out by the analytical model proposed in this work.

Keywords: *Mechanical analysis; Ultrahigh pressure; Interlayer pressure; analytical mode*

1 Introduction

Ultrahigh pressure apparatus has a widespread application prospect in nuclear engineering, powder metallurgy, petrochemical, synthetic quartz, artificial diamond, and jet cutting technology. And bearing capacity is one of the focus problem in ultrahigh pressure apparatus. Wang, Yuan, Hu, Wang, & He (2007) built a theoretical model for shrinkage vessel and pointed out that the maximum bearing capacity of single-layer cylinders was just close to half of the yield stress; however, that of shrink-fit vessel can almost close to the yield strength. Miraje, & Patil (2011) calculated shrinkage pressures between two contacting cylinders to reduce the hoop stress and to make it more uniform over the thickness. However, Yuan & Liu (2012) revealed that the shrinkage pressures would result in reverse yielding by the method of calculation and simulation. Considering medium principal stress and brittle softening, Zhu, Zhao, Zhang, Zhang, Wang (2015), and Shufen, Mahanta and Dixit (2019) presented the elastic-brittle-plastic unified solutions of limit internal pressure for double-layered combined thick-walled cylinder. As to autofrettaged apparatus, Zhu & Yang (1998) pointed out that if its thickness was increased infinitely, an autofrettaged cylinder had limitless strength , but a larger pressure need be applied on the cylinder before its use. The study performed in Lee, Lee, Yang, Kim, Cha, & Hong (2009) revealed that due to Bauschinger effect the compressive residual stress of the strain-hardening model for the autofrettaged apparatus is lower than that of the elastic-perfectly plastic model; based on the above study, a Matlab-based GUI for the autofrettaged apparatus was developed by Yang, Lee, Lee, Kim, Cha, & Hong, (2009). The results also showed that the magnitudes of calculated hoop residual stress at the internal radius of the vessel strongly depended on the employed material model (Maleki, Farrahi, Jahromi, & Hosseinian, 2010); Ruilin Zhu, Guolin Zhu, & Aifeng Mao found out the safe and optimum workload conditions for autofrettaged cylinders by a set of simplified equations. And the hoop residual stress of the autofrettaged apparatus under different conditions, was analyzed by analytical and FE analysis (Shim, Kim, Cha, & Hong, 2010; Alexandrov, 2020). Wahi, Ayob, & Elbasheer (2011) proposed an analytical procedure of thick-walled cylinder under the aim of predicting the required autofrettaged pressure for various levels of allowable pressure and attaining optimum fatigue life. Further studies indicated that under specified geometric dimensions and materials, optimum autofrettaged pressure approached to 1.5 times the working pressure, but Bauschinger effect resulted in earlier onset of

Received 25 February 2021; Accepted 28 May 2021

reverse yielding (Hu & Puttagunta, 2012). Literatures (Zhu, Zhu, & Tang, 2012; Li, 2021) demonstrated the maximum bearing capacity of an autofrettaged cylinder was approximately equal to yielding strength of the materials on the basis of the ideal conditions.

To increase elastic-limit capacity and obtain the optimum radial dimension of the ultrahigh pressure apparatus, the autofrettaged apparatus with interlayer pressure (ACCIP) was set up and an analytical model was also presented in this work. The present work was lay out as follows: firstly, derivation of analytical model and structural optimum model was presented on the basis of the ideal conditions in literature (Zhu, Zhu, & Tang, 2012); next, the total radius ratios were presented at the limit workload of the $p_w = 1.07\sigma_s$; afterwards, the stresses field on the ACCIP method under the different total radius ratios and total radius ratio were analyzed. Results demonstrated that the limit workload were close to 1.5 times of the yield strength σ_s by the using ACCIP method, besides the optimum total radius ratio was approximately equal to 3.29 under the limit workload of the 1.07 σ_s.

2 Theoretical model

2.1 Geometric model

The ultrahigh pressure apparatus with ACCIP method consisted of internal cylinder, the external cylinder, and interlayer medium liquid, which was shown schematically in Fig. 1, where the Δ is near to zero.

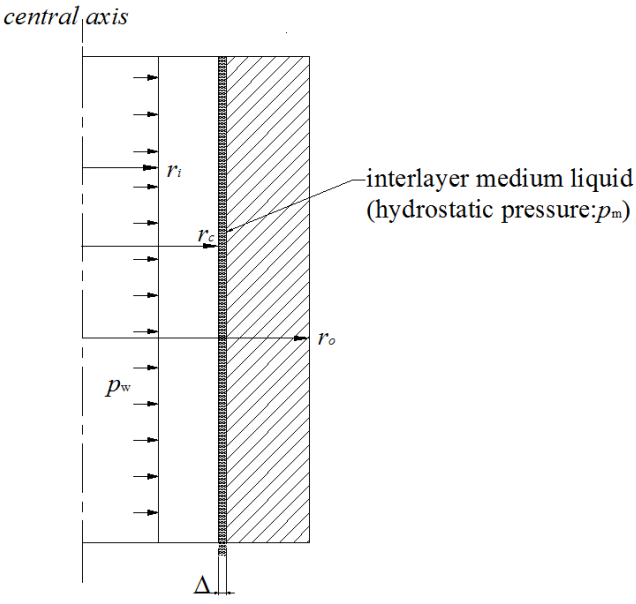

Fig.1. Schematic view

2.2 Mathematical model

Since it was autofrettaged before use, the autofrettaged cylinder underwent the interlayer workload of the pressure p_m, as well as residual stresses. The resultant stresses were listed as follows:

$$\sigma_r^{total} = \sigma_r + \sigma_r^r \tag{1a}$$

$$\sigma_\theta^{total} = \sigma_\theta + \sigma_\theta^r \tag{1b}$$

where σ_r^{total}, σ_θ^{total} are the resultant radial, hoop stresses; σ_r^r, σ_θ^r are the residual radial, hoop stresses; and σ_r, σ_θ are the radial, hoop stresses, respectively.

Furthermore, according to Lame's solution (Miraje, & Patil, 2011), stress components of the internal cylinder were derived as below:

$$\sigma_r = \frac{p_w r_i^2 - p_m r_c^2}{r_c^2 - r_i^2} - \frac{(p_w - p_m) r_i^2 r_c^2}{(r_c^2 - r_i^2) r^2} \tag{2a}$$

$$\sigma_\theta = \frac{p_w r_i^2 - p_m r_c^2}{r_c^2 - r_i^2} + \frac{(p_w - p_m) r_i^2 r_c^2}{(r_c^2 - r_i^2) r^2} \tag{2b}$$

where r_i was internal radius, r_c was the radius of interlayer medium liquid referring to Fig. 1, r was radius variable, p_m was the interlayer pressure, and p_w was the workload when the internal surface of the internal cylinder was at elastic limit state.

When internal cylinder was autofrettaged, the residual stresses in plastic region were as followings:

$$\sigma_r^r = \sigma_s \ln(r/r_c) - p_p(1 - r_c^2/r^2)/[1 - (1/K_i)^2] \tag{3a}$$

$$\sigma_\theta^r = \sigma_s[1 + \ln(r/r_c)] - p_p(1 + r_c^2/r^2)/[1 - (1/K_i)^2] \tag{3b}$$

where the K_i was equal to r_c/r_i.

And the residual stresses in elastic region were as following:

$$\sigma_r^r = [(\sigma_s r_m^2/2r_c^2) - p_p/(K_c^2 - 1)](1 - r_c^2/r^2) \tag{4a}$$

$$\sigma_\theta^r = [(\sigma_s r_m^2/2r_c^2) - p_p/(K_c^2 - 1)](1 + r_c^2/r^2) \tag{4b}$$

where the r_m was the radius of elastic-plastic interface in the internal cylinder, p_p was the corresponding pressure on internal wall of internal cylinder when the radius of elastic-plastic interface in the internal cylinder was r_m and the K_c was equal to r_c/r_c.

On the basis of the third strength theory (Borei, Sidebottom, Seely, & Smith, 1978) the equivalent stress was expressed as follows:

$$\sigma_{eq}^{III} = \sigma_\theta - \sigma_r = 2\tau_{max} \le \sigma_s \tag{5}$$

where σ_{eq}^{III} is the equivalent stress, τ_{max} is the maximum shear stress, and the σ_{eq}^{III} is equal to the yield strength σ_s, when the cylinder is in plastic state.

Substituting the Eqs. (2a) and (2b) into Eq. (5) obtained the shear stress Eq. (6) as follows:

$$\tau = \frac{(p_w - p_m) r_i^2 r_c^2}{(r_c^2 - r_i^2) r^2} \tag{6}$$

When the r was equal to r_i, the τ obtained the maximum on the inner wall of the internal cylinder, as follows:

$$\tau_{max} = \frac{(p_w - p_m) r_c^2}{(r_c^2 - r_i^2)} \tag{7}$$

Substituting the Eqs. (3a) and (3b) into Eq. (5) obtained the Eq. (8a) of the shear stress in plastic zone, as follows:

$$\tau^{rp} = 0.5\sigma_s - p_p(r_i/r)^2/[1 - (1/K_i)^2] \tag{8a}$$

According to Eq (8a), the τ^{rp} obtained the maximum on the inner wall of the internal cylinder, when the r was equal to r_i.

Substituting the Eqs. (4a) and (4b) into Eq. (5) obtained the Eq. (8b) of the shear stress in plastic zone, as follows:

$$\tau^{re} = [(\sigma_s r_m^2 / 2r_c^2) - p_p /(K_i^2 - 1)](r_c^2 / r^2) \quad (8b)$$

According to Eq (8b), it can be known that the τ^{re} reached a maximum on the inside wall of the internal cylinder, when the r was equal to r_i.

According to Eqs. (8a)- (8b), we can obtain the following equation:

$$\tau^{rp} - \tau^{re} = 0.5\sigma_s - p_p (r_i / r)^2 /[1 - (1/K_i)^2]$$

$$-[(\sigma_s r_m^2 / 2r_c^2) - p_p /(K_i^2 - 1)](r_c^2 / r^2) = 0.5\sigma_s - \sigma_s r_m^2 / 2r_c^2 \quad (9)$$

Since, $r_i^2 < r_m^2 < r_c^2$, so Eq. (9) satisfied the following inequality:

$$\tau^{rp} - \tau^{re} = 0.5\sigma_s - \sigma_s r_m^2 / 2r_c^2 > 0 \quad (10)$$

That is, τ^{rp} is always greater than τ^{re}_{max}.

Substituting the $r=r_i$ into Eq. (8a) obtained the equation as follows:

$$\tau^{rp}_{max} = 0.5\sigma_s - p_p /[1 - (1/K_i)^2] \quad (11)$$

In order to avoid reverse yielding, Ref. (Wang, Yuan, Hu, Wang, & He, 2007) gives the formula as follows:

$$p_{pmax} = \sigma_s (1 - 1/K_i^2) \quad (12)$$

Substituting the Eq. (12) into Eq. (11) obtained the equation as follows:

$$\tau^{rp}_{max} = 0.5\sigma_s - \sigma_s (1 - 1/K_i^2)/(1 - 1/K_i^2) = -0.5\sigma_s \quad (13)$$

Substituting the Eqs. (1a) and (1b) into Eq. (5) obtained the equation as follows:

$$\tau^{total} = (\sigma_\theta^{total} - \sigma_r^{total})/2$$

$$= (\sigma_\theta - \sigma_r)/2 + (\sigma_\theta^r - \sigma_r^r)/2 = \tau + \tau^r \quad (14)$$

where τ^{total} was the resultant shear stress.

From the inequality (10), it was known that τ^{rp} was always greater than τ^{re}, therefore the τ^{rp}_{max} was also always greater than the τ^{re}_{max}. Substituting the Eqs. (7) and (11) into Eq. (5) obtained the resultant maximum shear stress τ^{total}_{max}, as follows:

$$\tau^{total}_{max} = \tau_{max} + \tau^r_{max} = \frac{(p_w - p_m) r_c^2}{(r_c^2 - r_i^2)} - 0.5\sigma_s \quad (15)$$

When the inside wall of the internal cylinder just happen to yield, based on Eq. (5), τ^{total}_{max} is equal to $0.5\sigma_s$, that is,

$$\tau^{total}_{max} = \frac{(p_w - p_m) r_c^2}{(r_c^2 - r_i^2)} - 0.5\sigma_s = 0.5\sigma_s \quad (16)$$

According to Eq. (16), the elastic-limit pressure equation of the internal cylinder was expressed as below:

$$p_w = \sigma_s \left(1 - \left(\frac{1}{K_i}\right)^2\right) + p_m \quad (17a)$$

The external cylinder was only underwent the interlayer pressure p_m, meanwhile, it was also a conventional thick cylinder. According to Ref. (Wang, Yuan, Hu, Wang, & He, 2007), the plastic-limit pressure equation of the external cylinder was expressed as follows:

$$p_m = \frac{\sigma_s}{2}\left(1 - \left(\frac{1}{K_o}\right)^2\right) \quad (17b)$$

On the basis of Eqs (17a) and (17b), the plastic-limit workload p_w can be obtained, and it is obvious that the elastic-limit pressure p_w can approach 1.5 times yield strength σ_s of the materials, when K_o tends to infinity.

2.3 structrual optimum model

According to Eqs.(17a) and (17b), Eqs(18a) and (18b) were obtained respectively as follows:

$$K_i = \left[\sigma_s /(p_m + \sigma_s - p_w)\right]^{0.5} \quad (18a)$$

$$K_o = \left[\sigma_s /(\sigma_s - 2p_m)\right]^{0.5} \quad (18b)$$

$$K = K_i K_o \quad (18c)$$

where Eq.(18c) expressed the dimension relation between the radii, and K was total radius ratio: the outside radius r_o of the external cylinder to internal radius r_i of the internal cylinder.

Objective fuction (19a) can be derived by substituting the Eqs.(18a) and (18b) into Eq.(18c).

$$K = \left[\sigma_s /(p_m + \sigma_s - p_w)\right]^{0.5} \cdot \left[\sigma_s /(\sigma_s - 2p_m)\right]^{0.5} \quad (19a)$$

$$\left[\sigma_s /(p_m + \sigma_s - p_w)\right]^{0.5} > 1 \quad (19b)$$

$$\left[\sigma_s /(\sigma_s - 2p_m)\right]^{0.5} > 1 \quad (19c)$$

where Eqs.(19b) and (19c) were dimension constraint of radius ratios: K_i and K_o.

Eqs.(19a)-(19c) were the optimization model. Based on the above model, it can be obtained that the relation cureves between radius ratio and interlayer pressure under a specified working pressure.

3 Results and analysis

Suppose the material (tool steel H13) of cylinders in the ACCIP method were elastic-perfectly plastic, and its mechanical properties were as follows: the yield strength is 1542 MPa, the ultimate strength is 1884 MPa and the Possion's ratio is 0.3. If the elastic-limit workload p_w equaled 1650 MPa, and then the stresses of the ACCIP method under different K_i of 5.45, 2.83, 2.16, 1.81 and 1.59 were simulated.

The internal cylinder was autofrettaged before use, when it was autofrettaged, its residual stresses distribution of the internal autofrettaged cylinders was shown in Fig. 3 (a), (b) and (c). The end abscissas of the curves was the radius ratio r_c/r_i of the internal autofrettaged cylinders. It can be seen in Fig. 3 (a) that the maximum absolute value of the residual radial stress was less than 250 MPa, and when K_i=5.45, 2.83, 2.16, the internal autofrettaged cylinder was basically in full plastic state, therefore it can be seen in Fig. 3 (b) that there was obvious difference in the residual hoop stress between K_i=5.45, 2.83, 2.16, 1.81 and 1.59. Meanwhile, it can be seen in Fig. 3 (c) that all the residual shear stresses were lower than the shear yield of its materials, therefore it didn't happen to yield reversely. When the workload of the 1650 MPa was applied on the inner surface of the internal autofrettaged cylinder, the resultant shear stresses of whole apparatus was below than the shear yield strength line shown in Fig. 2.

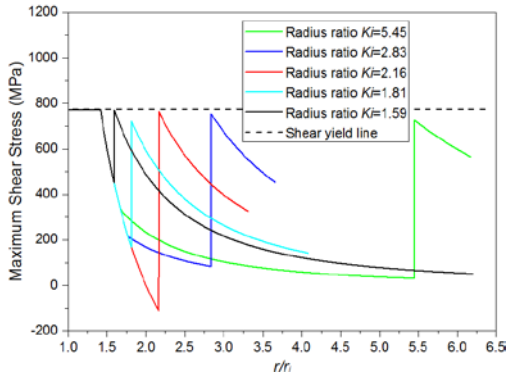

Fig. 2 Resultant shear stress of the cylinder when working pressure $p_w = 1650\text{MPa}$

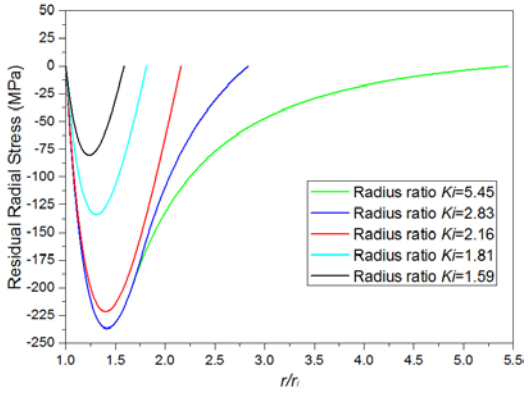

(a) Residual radial stress

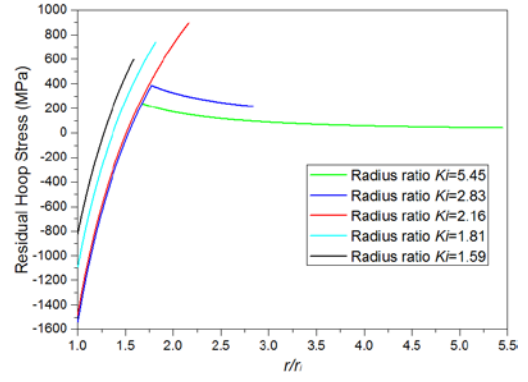

(b) Residual hoop stress

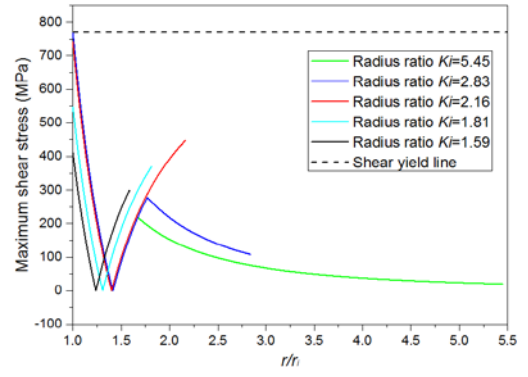

(c) Residual shear stress

Fig. 3 Residual stress of the internal autofrettaged cylinder

It can be seen from the above Fig. 2, when the workload p_w exceeded the yielding strength, the whole apparatus do not happen to yield; furthermore, outside radius r_o reached the minimum, when the radius ratio K_i was approximately equal to 2.16.

Interlayer pressure has effect on resultant shear stresses of the apparatus. Suppose the radius ratio K_i was approximately equal to 2.16, and the total radius ratio K reached the minimum 3.29. The interlayer pressures were 160, 300, 440, 580 and 720 MPa, respectively, and when the workload of 1650 MPa ($p_w = 1.07\sigma_s$) was applied on the inner surface of internal cylinder, the resultant shear stresses in the internal cylinder were shown in Fig. 4. When interlayer pressure p_m was 580 and 720 MPa, the corresponding resultant shear stresses were above than the shear yield strength limit and the external cylinder happened to yield; when interlayer pressure p_m was 160 and 300 MPa, the corresponding resultant shear stresses of the external cylinder were below than its shear yield strength, although the external cylinder didn't happen to yield, the internal cylinder did; and only when the interlayer pressure p_m was equal to 440 MPa, did neither the internal nor the external cylinder happen to yield. From the above analyses, the conclusion can be drawn that the interlayer pressure of the $p_m = 440$ MPa was the optimum interlayer pressure under the given working pressure of the $p_w = 1650\text{MPa}$, which avoid both the yield of the external cylinder and of the internal cylinder.

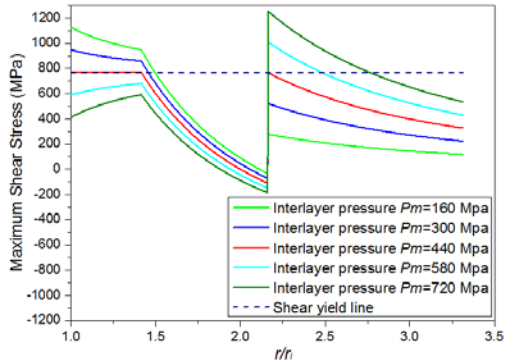

Fig. 4 Resultant Shear Stress vs interlayer pressure when working pressure $p_w = 1650\text{MPa}$

5 Conclusions

Many studies centered on shrinkage and autofrettage methods. Nevertheless, less attention has been payed to the ultrahigh pressure apparatus with interlayer pressure (ACCIP method). Therefore, the present work presented the general theoretical study of the ACCIP method.

In the present work, calculation of the stresses were on the basis of the ideal conditions, and the calculated results revealed the plastic-limit workload p_w can be as high as 1.5 times the yielding strength σ_s, which was much larger than those of shrink-fit vessel and autofrettaged cylinder. When the working pressure of the $p_w = 1.07\sigma_s$, the apparatus can remain within the elastic domain of the materials;

furthermore, the minimum radius ratio r_o/r_i was equal to 3.29. Analyses also showed that under the minimum radius ratio, the residual and resultant stresses were lower than the yielding strength respectively. Meanwhile, the studies also indicated that there was an optimum interlayer pressure when the total radius ratio takes the minimum. Overall, the ACCIP method can both increase elastic-limit workload of ultrahigh pressure apparatus and optimize its structure.

Acknowledgments: This work was supported by the Natural Science Foundation of Jiangsu Province of China (Grant No. BK20200999), meanwhile I am also grateful to Prof. Renshu Yuan for his help.

References

[1] Wang, Z., Yuan, S., Hu, L., Wang, Z., and He, Z. (2007), Fundamentals of elasticity OF and plasticity, (2nd Edition). Harbin: Harbin institute of technology press.

[2] Miraje, A. A and Patil, S. A. (2011) "Minimization of material volume of three layer compound cylinder having same materials subjected to internal pressure", International Journal of Engineering, Science and Technology, 3(8), 26-40. http://doi.org/10.4314/ijest.v3i8.3.

[3] Yuan, G. and Liu, H. (2012), "An analytical solution of residual stresses for shink-fit two-layer cylinders after autofrettage based on actual material behavior", Journal of Pressure Vessel Technology, 134(6), 061209. http://doi.org/10.1115/1.4006121.

[4] Zhu, Q., Zhao J., Zhang, C., Zhang, D. and Wang, S. (2015), "Elastic-brittle-plastic unified solutions of limit internal pressure for double-layered combined thick-walled cylinder", Engineering Mechanics, 32 (9), 68-75. http://doi.org/10.6052/j.issn.1000-4750.2013.07.0627.

[5] Shufen, R. , N. Mahanta , and U. S. Dixit . "Development of a Thermal Autofrettage Setup to Generate Compressive Residual Stresses on the Surfaces of a Cylinder." Journal of Pressure Vessel Technology 141.5(2019). DOI: 10.1115/1.4044119.

[6] Zhu, R. and Yang, J. (1998), "Autofrettage of thick cylinders", International Journal of Pressure Vessels & Pining, 75(6), 443-446. http://doi.org/10.1016/S0308-0161(98)00030-1.

[7] Lee, E. Y., Lee, Y. S., Yang, Q. M., Kim, J. H., Cha, K. U. and Hong, S. K. (2009), "Autofrettage Process analysis of a compound cylinder based on the elastic-perfectly plastic and strain hardening stress-stain curve", Journal of Mechanical Science and Technology, 23(12), 3153-3160. http://doi.org/10.1007/s12206-009-1009-9.

[8] Yang, Q. M., Lee, E. Y., Lee, Y. S., Kim, J. H., Cha, K. U. and Hong, S. K. (2009), "A residual stress analysis program using a Matlab GUI on an autofrettaged compound cylinder", Journal of Mechanical Science and Technology, 23(11), 2913-2920. http://doi.org/10.1007/s12206-009-0820-7.

[9] Maleki, M., Farrahi, G. H., Jahromi, B. H. and Hosseinian, E. (2010), "Residual stress analysis of autofrettaged thick-walled spherical pressure vessel", International Journal of Pressure Vessels & Piping, 87(7), 396-401. http://doi.org/10.1016/j.ijpvp.2010.04.002.

[10] Zhu, R., Zhu G. and Mao, A. (2010), "Mechanical analysis of autofrettaged high pressure apparatus", Journal of Theoretical and Applied Mechanics, 55(1), 17-27. http://doi.org/10.15632/jtam-pl.55.1.17.

[11] Shim, W. S., Kim, J. H., Lee, Y. S., Cha, K. U. and Hong, S. K. (2010), "A study on Hydraulic Autofrettage of Thick-Walled Cylinders Incorporating Bauschinger Effect", Experimental Mechanics, 50(5), 621-626. http://doi.org/10.1007/s11340-009-9255-4.

[12] Alexandrov, S., et al. "Description of Residual Stresses in Autofrettaged Open-Ended Cylinders Made of High-Strength Steel." Materials 13.13(2020):2940.DOI: 10.3390/ma13132940.

[13] Wahi, N., Ayob, A. and Elbasheer, M. K. (2011), "Effect of Optimum Autofrettage on Pressure Limits of Thick-Walled Cylinder", International Journal of Environmental Science and Development, 2(4), 329-333. http://doi.org/10.7763/IJESD.2011.V2.146.

[14] Hu, Z. and Puttagunta, S. (2012), "Computer modeling of internal pressure autofrettage process of a thick-walled cylinder with the bauschinger effect", American Transactions on Engineering & Applied Sciences, 1(2), 143-161.

[15] Zhu, R. L., Zhu, G. L. and Tang, F. (2012), "Analysis on autofrettage of cylinders", Chinese Journal of Mechanical Engineering, 25(3), 615-623. http://doi.org/10.3901/CJME.2012.03.615.

[16] Li, G. , et al. "Research on Autofrettage Mechanism in Ultra-High Pressure Thick-walled Vessel." Journal of Physics: Conference Series 1802.2(2021):022001 (6pp). http://doi.org/10.1088/1742-6596/1802/2/022001.

[17] Miraje, A. A. and Patil, S. A. (2011), "Minimization of material volume of three layer compound cylinder having same materials subjected to internal pressure", Internal Journal of Engineering, Science and Technology, 3 (8), 26-40.http://doi.org/10.4314/ijest.v3i8.3.

[18] Boresi, A. P., Sidebottom, O. M., Seely, F. B. and Smith, J. O. (1978), Advanced Mechanics of Materials, (3rd Edition.), John Wiley & Sons, New YorK: John Wiley & Sons.

Viser Technology Pte. Ltd.
Mechanical Engineering Science
DOI: 10.33142/mes.v3i1.4331

Research Article Open Access

Research on Influence Mechanism of Transmission Accuracy for Harmonic Drive Mechanism Considering Multi-factor Coupling

Peng ZHAO*, Shuang ZHANG, Yang LIU

Academy of China Changfeng ELectro-mechanical Technology, Haidian District, Beijing 100039

***Corresponding Author:** Peng ZHAO, E-mail: blackhouse02@126.com*

Abstract:
The influence mechanism of transmission accuracy for harmonic drive mechanism considering multi-factor coupling was studied. According to analysis of influence factors of transmission accuracy for harmonic drive mechanism, it was obtained that the transmission errors of harmonic drive mechanism include processing errors and installation errors. The transmission error is produced by eccentric vector, it directly affects the rotation angle of output shaft and it makes harmonic drive mechanism produce backlash. Then analyze the movement error caused by the rigid wheel machining error, the flexible wheel machining error, the assembly error of the rigid wheel and the flexible wheel, the wave generator component, and the comprehensive expression method of motion error generated by each error source was obtained. The performance test device of space drive mechanism was used to test, and the law of the transmission accuracy of harmonic drive mechanism with temperature, speed and assembly clearance was obtained. The test results show that the transmission accuracy of harmonic drive mechanism decreases with increasing temperature, and the speed has little effect on the transmission accuracy of harmonic drive mechanism; the assembly quality has a significant impact on harmonic drive accuracy.

Keywords: *harmonic drive mechanism; transmission accuracy; error source*

1 Introduction

With the continuous development of aerospace technology and continuous improvement of space mission requirements, the application of space harmonic drive mechanisms is becoming more and more extensive, it shows a diversified development trend. The harmonic drive mechanism has a large transmission ratio and a wide range; stable transmission, high carrying capacity, small volume and weight for transmitting unit torque; small and uniform tooth surface wear, high transmission efficiency, and high transmission accuracy; small backlash and achievable Zero backlash transmission; can ensure the transmission of movement to the confined space. Due to its many advantages, harmonic drive has been widely used.

The spatial harmonic drive mechanism is a highly reliable and long-life product. Its system composition is very complex. Operating conditions such as load, working conditions, temperature, and vacuum will affect its performance. Its performance will gradually degrade with the prolonged use of time. Reliability and life will gradually decrease [1-2]. The space drive mechanism has poor observability and detection in the space operating environment, difficult to accumulate information, and less available information. It is also difficult to simulate and verify on the ground. It is a real poor information and small sample product. It is necessary to study the reliability of the space drive mechanism. There is enough scientific experiment to support, and through the organic combination of experimental data and related theories, it can accurately grasp the influence mechanism of the transmission accuracy and reliability of the space drive mechanism.

2 Analysis of Influencing Factors on Transmission Accuracy of Harmonic Drive Mechanism

According to the motion principle of the harmonic drive mechanism, the cross-section of flexible wheel is a circle before assembly. When the wave generator and the flex bearing are installed in the flexible wheel, the flexible wheel is forced to deform, and the teeth and rigid The teeth of the wheel are completely meshed, the teeth at the short shaft are completely disengaged, and the teeth in different sections along the circumference of the flexible wheel between the long and short shafts are in different transition states that are meshing in or meshing out. Therefore, when

Received 1 April 2021; Accepted 16 May 2021

the rigid wheel is fixed, the wave generator is input, and the flexible wheel is output, the meshing depth of the teeth of the flexible wheel and the rigid wheel will affect the output angle of the flexible wheel to a certain extent [3].

Obviously, when there is an error in the size or assembly of the various components that make up the harmonic reducer, it will directly or indirectly affect the coaxiality of the rigid wheel axis and the flexible wheel axis. If the theoretical axis of the rigid wheel and the theoretical axis of the flexible wheel do not coincide, the meshing of the gear teeth will change. Therefore, the offset between the axis of the three major parts and their theoretical axes can be used to quantify the transmission errors caused by different machining errors and assembly errors [4].

The main components of the harmonic reducer are the flexible wheel, rigid wheel and wave generator. The rigid wheel of the reducer is fixed, the driving part is the wave generator, and the driven part is the flexible wheel. According to its structure, it can be seen intuitively that the machining and installation errors of various parts and their shapes have the following main effects on the transmission error: 1) Transmission error is generated by the eccentric vector; 2) It directly affects the rotation angle of the output shaft; 3) Make the harmonic reducer produce hysteresis.

3 Transmission error caused by the error source of the harmonic drive mechanism

Combining the meshing characteristics of the harmonic drive, according to its transmission principle, analyze the size and frequency of the motion error that each error source can produce.

According to the working principle of harmonic gear transmission, there are two meshing areas at both ends of the cam long shaft. In each area, there are multiple pairs of gear teeth participating in meshing at the same time, but the meshing degree of each pair of gear teeth is different (as shown in Fig. 1). Now the cam long shaft is used as the dividing line to divide the meshing into two parts: the working tooth side and the non-working tooth side. Among them, the working tooth side plays a transmission role. The correct meshing area of the harmonic gear drive can only be carried out in a local area. The teeth participating in the meshing outside this area are in sharp point contact or no contact at all. Although the flexible wheel has elasticity and can play a certain deformation coordination effect, it is possible to expand the correct meshing area, but this expansion is extremely limited, and it is generally larger under load, and under no load. The next is smaller. When there is an eccentricity error in the flexible or rigid wheel, the eccentric error vector has different effects on the gear tooth meshing degree of the two meshing areas. In the area close to the eccentric error vector, the eccentricity makes the meshing area expand, that is, the correct meshing tooth pair As the number increases, the number of sharp point contacts decreases; however, the effect is just the opposite in the other meshing area. Due to the influence of various eccentric errors in the harmonic gear transmission, the above-mentioned situation is bound to occur in the meshing characteristics of the harmonic gear transmission [5].

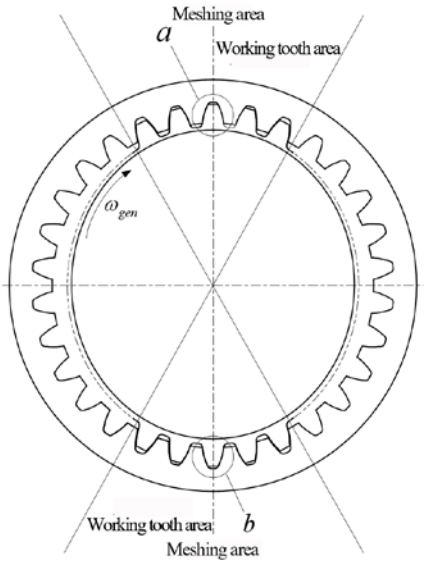

Fig.1 Harmonic gear drive transmission principle diagram

3.1 Motion error caused by rigid wheel machining error

Due to the geometric eccentricity and movement eccentricity of the rigid wheel during processing, the base circle and index circle center of the rigid wheel do not coincide with the center of rotation, resulting in a comprehensive error vector $_{21}$. Since the rigid wheel is fixed, the comprehensive error vector e_{21} will remain unchanged during meshing process. Suppose the comprehensive error vector e_{21} is exactly on the *OY* axis (as shown in Fig. 2), and the angle θ is between the long axis of cam and the eccentric error vector e_{21}. The eccentricity error vector can be divided into two parts at the gear tooth meshing node: normal displacement and tangential displacement. The normal displacement in the *n-n* direction is the increment along the meshing line, which will produce movement errors; the tangential displacement in the τ - τ does not produce motion error [6].

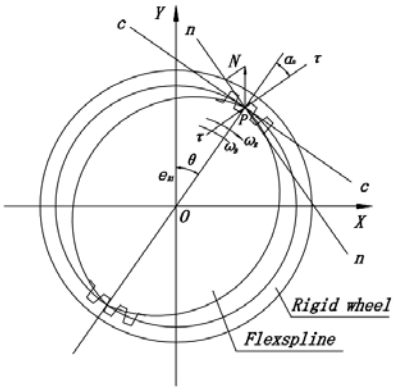

Fig.2 Influence of Rigid Wheel Eccentricity on Transmission Error

If the rotation angular velocity ω_b of wave generator is used as the independent variable, the expression of the motion error due to the machining error of the rigid wheel can be obtained as:

$$\Delta_G = \Delta_{21} + \Delta_{22} = \frac{1}{2}\Delta F_{p2}\sin\left(2\omega_b t\right) + \frac{1}{2}\Delta f_{f2}{}'\sin\left(2\omega_b z_G t\right)$$

where, $\Delta f_{f2}{}'$ ——Comprehensive error of adjacent teeth in tangential direction of rigid wheel;

z_G——Teeth number of rigid wheel;

t——time.

3.2 Motion error caused by flexible wheel machining error

The flexible wheel also has a comprehensive eccentricity caused by geometric eccentricity and movement eccentricity during processing, so that the centers of the base circle and the index circle do not coincide with the center of rotation. Suppose its comprehensive eccentricity is e_{11}. Since the transmission of the harmonic gear is relatively large, the comprehensive eccentric vector can be regarded as constant during the half-turn of the wave generator. Since the flexible wheel is rotating, there is always a certain moment when the eccentric vector coincides with the *OY* axis. It is assumed that the integrated eccentric vector e_{11} coincides with the *OY* axis at a certain moment. Eccentric vector $_{11}$ will cause the lower meshing area of the rigid wheel and the flexible wheel to weaken and the upper meshing area to strengthen. Since the considered state is that the comprehensive eccentricity e_{11} of the flexible wheel is fixed, and the teeth of the flexible wheel actively engage with the teeth of the rigid gear during meshing, the error will cause uneven transmission of the flexible wheel and cause movement errors. Analyze the movement error caused by the integrated eccentricity e_{11} of the flexible wheel processing is the same as the movement error caused by the integrated eccentricity of the rigid wheel [7].

Therefore, the expression of the motion error due to the processing error of the flexible wheel is

$$\Delta_R = \Delta_{11} + \Delta_{12} = \frac{1}{2}\Delta F_{p1}\sin\left(2\omega_b \frac{z_G}{z_R} t\right) + \frac{1}{2}\Delta f_{f1}{}'\sin\left(2\omega_b z_G t\right)$$

Where, Δ_{11}——The motion error value caused by the processing error of the flexible wheel;

ΔF_{p1}——Cumulative error of the flexible wheel;

z_G——Teeth number of rigid wheel;

z_R——Teeth number of flexible wheel;

ω_b——The angular velocity of the wave generator;

t——time.

3.3 Motion error caused by assembly error of rigid wheel and flexible wheel

The rigid wheel and the flexible wheel have assembly errors, which cause the relative meshing position of the rigid wheel and the flexible wheel to change, and the manufacturer's various assembly eccentricities. The eccentricity will affect the accuracy of the harmonic gear transmission movement, thereby causing movement errors. The eccentricity error vector caused by various errors between the rigid wheel and the flexible wheel can be divided into two types [8].

(1) Generate a fixed eccentric vector

Such eccentric vectors include: the run out of the mounting hole of the rigid wheel, the fit clearance between the mounting hole of the rigid wheel and the rigid wheel, the radial run out of the output shaft bearing, the fit gap between the two shells, the fit gap between the output shaft bearing and the hole, and the output shaft Bearing radial run out and output shaft bearing radial clearance, etc., the movement error caused by the eccentricity formed by the fit clearance and the run out error is similar to the movement error caused by the eccentricity formed by the machining error of the rigid wheel itself. Therefore, it can be used similarly to analyze the motion error caused by the comprehensive eccentricity formed by the rigid wheel processing error, and the motion error generated by each error source can be obtained as

$$\Delta_1 = \frac{e_1 \sin 2\left(\theta + \alpha_n\right)}{\cos\alpha_n}$$

Substituting the rotational angular velocity ω_b of the wave generator into the calculation formula of the motion error

$$\Delta_1 = \frac{e_1 \sin\left(2\omega_b t + \varphi_1\right)}{\cos\alpha_n}$$

Where, Δ_1——The movement error caused by the eccentric vector of the rigid wheel installation pair produced in the rigid and flexible wheel pairs;

e_1——The value of the eccentricity error caused by the fit clearance or beating that affects the installation accuracy of the rigid wheel;

ω_b——The angular velocity of the wave generator;

φ_1——The phase angle of the corresponding eccentricity error vector.

Since the various eccentricities produced during the assembly process are random, their phase angles are also randomly distributed, so that the movement errors generated by some eccentric vectors will cancel each other out, and finally a movement error value caused by the installation eccentricity will be formed.

(2) The eccentricity error vector formed by the assembly error

This kind of vector rotates with the flexible wheel, including: the eccentric vector error formed by the beating of the output shaft and the fit clearance between the output shaft and the flexible wheel. The method of analyzing the type of error is similar to the motion error caused by the processing error of the flexible wheel itself, and the motion error generated is

$$\Delta_2 = \frac{e_2 \sin 2\left(\theta + \alpha_n\right)}{\cos\alpha_n}$$

Substituting the rotational angular velocity ω_b of the wave generator into the calculation formula of the motion error

$$\Delta_2 = \frac{e_2 \sin\left(2\frac{z_G}{z_R}\omega_b t + \varphi_2\right)}{\cos\alpha_n}$$

Where, Δ_2——The movement error caused by the eccentricity of the rigid wheel installation in the rigid and flexible wheel pairs;

e_2——The fit clearance or runout value that affects the installation accuracy of the flexible wheel;

ω_b——The angular velocity of the wave generator;

z_G——Teeth number of rigid wheel;

z_R——Teeth number of flexible wheel;

φ_2——The phase angle of the error vector.

3.4 Motion error caused by wave generator components

In the harmonic gear drive, the harmonic gear drive has an additional wave generator than the general gear drive. The manufacturing and assembly errors of the wave generator directly affect the radial change of the flexible wheel, which changes the meshing relationship between the rigid spline and the flexible wheel, which also causes movement errors. The machining and installation errors of the rigid wheel form a composite eccentricity error. The wave generator has an eccentricity error vector. Because the eccentricity error vector of the rigid wheel and the eccentricity vector of the wave generator are superimposed on each other, additional motion errors are generated [9]. The frequency generated by this eccentricity error is the same as the rotation frequency of the wave generator, that is, when the wave generator rotates one revolution, this movement error is repeated once, and its approximate mathematical expression is

$$\Delta_3 = \frac{e_{3f}\sin\left(\omega_b t + \theta_{3f}\right)}{\cos\alpha_n}$$

Where, Δ_3——Motion error caused by eccentricity error rotating with wave generator;

e_{3f}——Error factors that rotate with the wave generator, such as fit clearance or runout;

θ_{3f}——The angle between the eccentricity error vector and the OY axis.

3.5 Comprehensive expression of motion error generated by each error source

The motion errors caused by the manufacturing and assembly errors of the various parts of the harmonic gear transmission can be divided into four categories: (1) The motion errors of the frequencies generated by the eccentric error vectors of the rigid wheels with eccentric errors, including the machining of the rigid wheels Error, the fixed eccentric error vector between the rigid wheel and the flexible wheel, the fixed eccentric error vector in the wave generator component; (2) The eccentric error vector generated by the flexible wheel that rotates with the flexible wheel generates frequency Movement error; (3) The frequency movement error produced by the eccentric error vector rotating with the wave generator in the wave generator component; (4) The frequency movement error produced by the small period error formed by the rigid and flexible wheel processing errors. Therefore, the comprehensive formula for the motion error of the harmonic gear transmission is

$$\Delta = \frac{\sum e_{1f}\sin\left(2\frac{z_G}{z_R}\omega_b t + \varphi_{1f}\right)}{\cos\alpha_n} + \frac{\sum e_{2f}\sin\left(2\omega_b t + \varphi_{2f}\right)}{\cos\alpha_n} + \frac{\sum e_{3f}\sin\left(2\omega_b t + \varphi_{3f}\right)}{\cos\alpha_n} + \frac{\sum f_{ff}'\sin\left(2z_G\omega_b t\right)}{2}$$

Where, Δ——Total motion error;

e_{1f}——Corresponding to the eccentric vector value of the flexible wheel;

e_{2f}——Corresponding to the eccentric vector value of the flexible wheel;

e_{3f}——The eccentric vector value that rotates with the wave generator;

f_{ff}'——Rigid and flexible tangential comprehensive error vector value;

φ_{1f}——The initial phase angle of the eccentric vector of the rigid wheel;

φ_{2f}——The initial phase angle of the eccentric vector of the flexible wheel;

φ_{3f}——The initial phase angle of the eccentric vector of the wave generator;

z_G——Teeth number of rigid wheel;

z_R——Teeth number of flexible wheel;

ω_b——The angular velocity of the wave generator;

t——time.

4 Test and results of factors affecting transmission accuracy of harmonic drive mechanism

The assembly state of the harmonic drive mechanism is shown in Fig. 3. The rigid wheel is fixed, the wave generator is input, and the flexible wheel is output. The relative position of the rigid and flexible wheel is fixed. The relative position X of the flexible wheel and the wave generator is determined by the spacer adjustment. When the relative position of the rigid and flexible wheels is fixed, the relative position X of the flexible wheel and the wave generator determines the meshing position of the harmonic gear. In order to study the influence caused by the meshing position of the harmonic gear, two thickness pads are processed Sheet, so that the relative positions of the flexible wheel and the wave generator are 0.75mm and 0.84mm, respectively.

The test object is a 40-type harmonic drive component, the lubrication method uses space lubricating grease, and the transmission ratio is 100. There are two assembly states: 1) Normal state: the relative position of the flexible wheel and the wave generator are 0.75mm respectively; 2) The specific state: the relative position of the flexible wheel and the wave generator is 0.84mm respectively. Test conditions: 1) Speed range 20~1500r/min; 2) Load torque range 5~15N·m; 3) Temperature range -75~125℃. The test results are shown in Fig. 4.

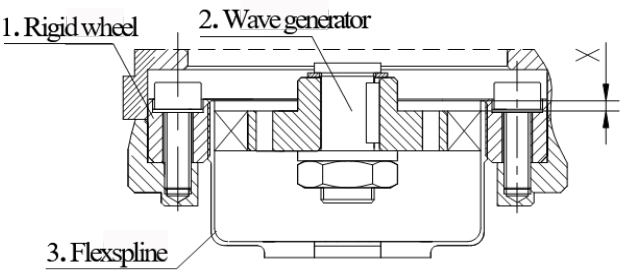

Fig.3 Schematic diagram of the assembly of the three major parts of the harmonic reducer

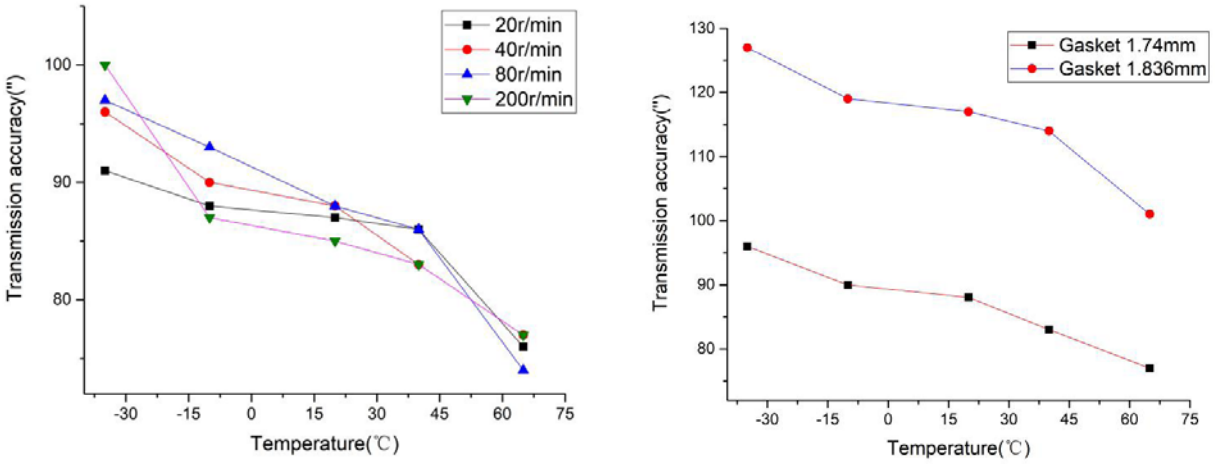

a) Transmission accuracy of harmonic drive components at different speeds and temperatures

b) Transmission accuracy of harmonic drive mechanism under different gap states

Fig.4 Transmission accuracy test of harmonic drive mechanism

According to the test plan, the transmission accuracy of the harmonic drive components in the two states was tested, and the transmission accuracy at different speeds and different temperatures was obtained. From Fig.4, comparing the transmission accuracy curves under different conditions, different speeds, and different temperatures, it can be found that:

(1) The transmission error of the harmonic reducer decreases with increasing temperature. The transmission error is 97" at -35℃, and 77" at 65℃. The transmission accuracy is greatly affected by temperature. The test results are consistent with the above mechanism analysis. It can be determined that the harmonic radial clearance is greatly affected by temperature;

(2) The transmission error of the harmonic reducer has nothing to do with the speed. The transmission accuracy curve shows that the relationship between transmission error and speed is irregular, and the transmission error values at the same temperature and different speeds are concentrated. Under the condition of excluding measurement errors, it can be considered as the transmission error value at the same temperature and different speeds. Consistent, so it can be considered that the transmission error and speed of the harmonic reducer are not significant;

(3) Assembly quality has a significant impact on the accuracy of harmonic drive. When the relative position difference between the flexible wheel and the wave generator is only 0.096mm, the difference of the harmonic drive error between the two states is about 35", so the assembly process must be strictly controlled during the product development stage.

5 Conclusions

(1) Through the analysis of the mechanism of influencing factors of transmission accuracy of the harmonic drive mechanism, it is found that the assembly error has a great influence on the transmission accuracy of harmonic drive mechanism, which can cause the accuracy of the harmonic drive mechanism to decrease, increase the stress, and increase the wear. Performance degradation and other failure modes.

(2) The transmission accuracy of the harmonic drive mechanism decreases with increasing temperature, and the speed has little effect on the transmission accuracy of the harmonic drive mechanism.

Reference

[1] KIM S Y, CASTET J F, SALEH J H. Spacecraft electrical power

subsystem: Failure behavior, reliability, and multi-state failure analyses[J]. Reliability Engineering and System Safety, 2012, 98: 55-65.

[2] Liu S, Wang Q. Studying contact stress fields caused by surface tractions with a discrete convolution and fast fourier transform algorithm[J]. Journal of Tribology, 2002, 124(1) : 36-45.

[3] PAN Bo, ZHANG Donghua, SHI Wenhua, et al. Modeling and analysis on pointing accuracy of antenna in satellite[J]. Spacecraft Engineering, 2011, 20(5): 49-54.

[4] CASTET J F, SALEH J H. Beyond reliability, multi-state failure analysis of satellite subsystems : A statistical approach[J]. Reliability Engineering and System Safety, 2010, 95: 311-322.

[5] WAYER J K, CASTET J F, SALEH J H. Spacecraft attitude control subsystem : Reliability , multi-state analyses, and comparative failure behavior in LEO and GEO[J]. Acta Astronautica, 2013, 85: 83-92.

[6] ZHANG Huibo. Pointing accuracy analysis of the two-axes-postion mechanism for satellite antenna[D]. Harbin: Harbin Institute of Technology, 2011.

[7] DENG Sier. Frictional torque characteristic of angular contact ball bearings[J]. Journal of Mechanical Engineering, 2011, 47(5): 114-120.

[8] Michael R, Johnson, Russ Gehling, Ray Head. Life Test Failure of Harmonic Gears in a Two-Axis Gimbal for the Mars Reconnaissance Orbiter Spacecraft[C]. Proceedings of the 38th Aerospace Mechanisms Symposium, Langley Research Center, 2006.

[9] Li Jun-Yang, Wang Jia-Xu, et al. Accelerated life testing of harmonic driver in space lubrication[J]. Journal of Engineering Tribology, 2015, 29(12): 1491-1502.

Viser Technology Pte. Ltd.
Mechanical Engineering Science
DOI: 10.33142/mes.v3i1.4332

Research Article Open Access

Theoretical and Experimental Study on The Speed-up of Freight Train with Mixed Marshaling of Light and Heavy Vehicle

Xing ZHANG, Li LI*, Dabin CUI*, Yaodong FU, Haiyang GUO

School of Mechanical Engineering, Southwest Jiaotong University, Chengdu, China

***Corresponding Author:** Li LI, Dabin CUI; No.111, North 1st Section, 2nd Ring Road, Chengdu City, 610031, China; lily1cn@aliyun.com, cdb1645@163.com*

Abstract:
To study the influence of the speed-up of a freight train with mixed marshaling of light and heavy vehicles on the dynamic behavior, a dynamic model of the freight train was established based on the modular method of cyclic variables, and the dynamic behavior of the freight train was simulated and analyzed under different marshaling patterns, speeds and line conditions. On-site speed-up test with different marshaling freight trains was carried out, and the stability and ride-index of the train before and after the speed-up were compared and analyzed. The feasibility of increasing the speed of freight trains with mixed marshaling of light and heavy cars was demonstrated theoretically and experimentally. The results show that the theory is in good agreement with the test, which can effectively reflect the dynamic behavior of the vehicle. The dynamic behavior of the freight train in the study meets the requirements of increasing speed to 90 km/h. This paper provides a theoretical basis and method for railway freight transportation and the speed-up of freight vehicles.

Keywords: *Mixed marshaling of light and heavy vehicle; Freight train; Dynamic behavior*

1 Introduction

As a large logistics transportation, freight train has an important impact on my country's development [1-2]. The speed of freight trains is the key factor that restricts transportation efficiency. With the increase of speed, it will greatly affect the smoothness and stability of the train operation. Some scholars have done a study on the effect of the speed-up of a freight train on the structure and dynamic performance. Liu [3] analyzed the structure, performance, and problems existing in the application of the current Z8AG, Z8G, ZK2, and swing bogies. Wu et al.[4] established the dynamic model of the nonlinear system and the finite element model of the side frame, and studied its fatigue life. Based on the Bayesian method and the reliability analysis method, Chen et al.[5] used the reliability analysis method to systematically study the lateral dynamic performance of the speed-up of a freight train on circular lines. Gong et al.[6] proposed an evaluation method for strengthening railway track structure based on the anti-derailment safety degree of a freight train. Chen et al.[7] carried out the 120 km/h comprehensive speed increase test of a freight train, and compared the test lines, vehicles, operating characteristics. Zhan et al.[8] made statistics and analysis of the problems found in various parts of a freight train in the maintenance process, and summed up the influence of the speed-up of a freight train. Qin [9] elaborated on the influence of the speed-up on a freight train and put forward targeted maintenance suggestions. To improve the safety of the vehicle operation, Xue [10] studied the lateral motion stability of the speed-raising locomotive and vehicle. Li et al.[11] improved the wheel-rail relationship of speed-increasing on the vehicle, and studied the MBS co-simulation of the dynamic design of bogies. Fu et al.[12] studied the dynamic behavior of key parameters of the steering frame on the vehicle, and gave the design scheme of speed-increasing. Under the background of speeding up and freight transport in China, Wu [13] pointed out the transformation and development direction of the speed-up of a freight train.

The above results have laid an important foundation for studying the influence of the speed-up on the dynamic performance of freight trains with mixed marshaling of light and heavy cars. However, most of the previous studies focused on the vehicle system and tended to focus on the influence of the speed-up on vehicle structure. Few studies have been conducted on the combination of theoretical calculation and experimental verification of the speed-up of empty-heavy mixed freight trains.

Received 25 February 2021; Accepted 28 April 2021

To improve the transportation capacity, this paper takes section lines and mixed freight trains with mixed marshaling of light and heavy cars as the object, and establishes the dynamic model of the long and large marshaling train based on the modular method of cyclic variables. The simulation analysis of the dynamic performance of the freight train is carried out. Under the guidance of a theoretical study, the test on the speed-up of the freight train in this section is completed.

2 Theoretical study

2.1 The modeling of vehicle dynamics

A freight train consists of at least dozens of vehicles. If a train contains n vehicles, and each vehicle has m degrees of freedom, then the whole system has $m \times n$ degrees of freedom. The equation of the system is expressed as follows:

$$[M]\ddot{Y} + [C]\dot{Y} + [K]Y = \{P\} + \{F\} \quad (1)$$

Among them, $[M]$is the mass matrix of the system, $[C]$ is the damping matrix of the system, $[K]$ is the stiffness matrix of the system, Y is the degree of freedom variable of the train, $\{P\}$ is the external force of the train, $\{F\}$ is the interaction force between vehicles.

Due to the long marshaling of freight trains, the traditional multi-rigid body dynamics modeling method will lead to " freedom explosion " and bring great difficulties to the calculation and analysis. Therefore, a modular method based on cyclic variables is developed to model and solve the dynamics of the long marshaling train [14]. Equation (1) could be decomposed into n sub-equations:

$$[m_i]\{\ddot{Y}_i\} + [c_i]\{\dot{Y}_i\} + [k_i]\{Y_i\} = \{p_i\} + \{f_i\} \quad (2)$$

Where, $\{Y_i\}$ is the set of the degree of freedom of the i^{th} vehicle, $[m_i]$ is the mass matrix of the i^{th} vehicle, $[c_i]$ is the damping matrix of the i^{th} vehicle, $[k_i]$ is the stiffness matrix of the i^{th} vehicle, $[p_i]$ is the external force acting on the i^{th} vehicle, and $[f_i]$ is the interaction force between the vehicles.

According to equation (2), a train can be regarded as an integral unit, and the system is divided into n basic integral units for calculation separately, and the calculation of each vehicle uses the same set of the degree of freedom variables. After the calculation of each vehicle is completed, the result is stored in the transfer variable, then the degree of freedom variable is released for the calculation of the next vehicle until all vehicles have completed the calculation. The next integration step is still carried out in the mode of the previous integration step until all the integration calculations are completed. In the integral calculation of the whole train, the degree of freedom variable will not increase with the increase of train formation, so it can solve the problem caused by the "degree of freedom explosion" of the long marshaling train. This method is called the "cyclic variable method".

The cyclic variable method is only good at solving the modeling of long marshaling train with only one type, but it is difficult to solve mixed train with many types. In the actual operating train, especially freight train, mixed marshaling often occurs. For this purpose, a locomotive and rolling stock model library (which can include all types of rolling stock) is established, and the dynamic simulation of the whole train can be performed by setting the sequence number of the corresponding vehicle type according to the train composition. When the train formation changes, there is no need to remodel and modify the program, just modify the definition of the formation, which greatly facilitates the modeling of the mixed train. This method is called "modular modeling".

Based on the modular modeling method of cyclic variables, the TPL train multi-body dynamics software is used for modeling, in which K2 bogie is selected for the empty train bogie, and the dynamics of a mixed freight train with light and heavy cars are simulated.

2.2 The analysis of dynamic performance

Using the American pentad spectrum for excitation, the dynamics of different trains when passing through the straight line and curve at the speed of 80 km/h, 85 km/h, and 90 km/h, as well as the dynamics of common braking and the emergency braking, are simulated. The stability of the train in the process of the speed-up is analyzed comprehensively, and the maximum value of the evaluation indexes of each group is calculated under different operating conditions and line conditions. The marshaling situation is as follows:

Croup 2: locomotive +16 heavy vehicles +5 empty vehicles +23 heavy vehicles +5 empty vehicles +16 heavy vehicles;

Group 3: locomotive +5 empty vehicles +55 heavy vehicles +5 empty vehicles;

Group 4: locomotive +55 heavy vehicles +10 empty vehicles;

Group 5: locomotive +27 heavy vehicles +10 empty vehicles +28 heavy vehicles.

The whole train is numbered with the locomotive as the starting position, that is, the locomotive number is 0, and the tail train number is 65.

The straight line is used to calculate the stability. Each group passes at the speed of 80 km/h, 85 km/h, and 90 km/h respectively in three passing modes (traction condition, common braking, and emergency braking) to obtain lateral and vertical stability. By comparing the stability at a different speed, it is found that the lateral stability and the vertical stability both increase with the increase of speed. Therefore, the maximum value of the lateral stability and the vertical stability of each marshaling is taken, as shown in Fig.1 and Fig.2 respectively. The red line with the value of 3.5 indicates that the index of a freight train is "excellent".

As can be seen from Fig.1, in the traction condition, for empty vehicles in the middle position, the lateral stability of group 2 decreases in the part of empty vehicle number (17-21, 45-49), while that of group 5 decreases in the first half of empty vehicle number (28-32), and increases in the latter part of empty vehicle number (33-38). However, for the empty vehicles at both ends of the position, the lateral stability of group 3 and group 4 increases when the

empty vehicles are numbered respectively. In the traction condition, empty vehicles should be placed in the middle position as far as possible, and the number of continuous empty vehicles should not be too many, which can effectively reduce the lateral stability. In common braking and emergency braking, the lateral stability of each group increases in the number of their respective empty vehicles. In common braking, because the speed reduces slowly, the vibration of the empty part is more balanced, so the lateral stability of the empty part of each group is not much different; However, in emergency braking, the pressure of the empty part becomes larger due to the extrusion of the front vehicle by the rear vehicle, resulting in the lateral stability of the empty vehicle with the rear number being greater than that of the empty vehicle with the front number. The maximum lateral stability of each group does not exceed the prescribed limit, reaching the "excellent".

As can be seen from Fig.2, for group 3 and group 4 with empty vehicle numbers at the rear, the vertical vibration becomes larger due to the lightweight of empty vehicles at the end. Under traction conditions, common braking, and emergency braking, the vertical stability of group 3 and group 4 decreases successively, and the vehicle number when the vertical stability begins to increase gradually falls back. When the two ends of empty vehicles are connected with heavy vehicles, the vertical vibration of empty vehicles will be suppressed, so the vertical stability of group 2 and group 5 is small. The maximum vertical stability of each group does not exceed the prescribed limit, reaching the "excellent".

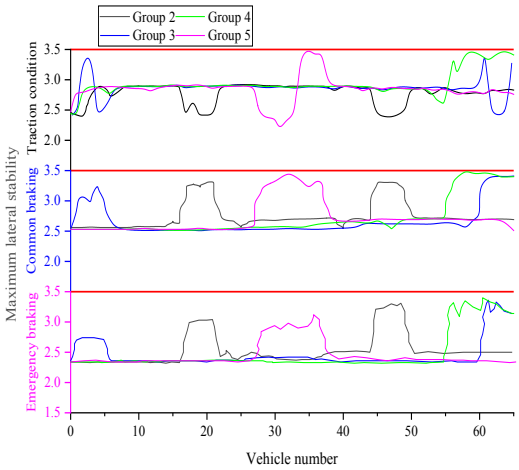

Fig.1 Maximum lateral stability

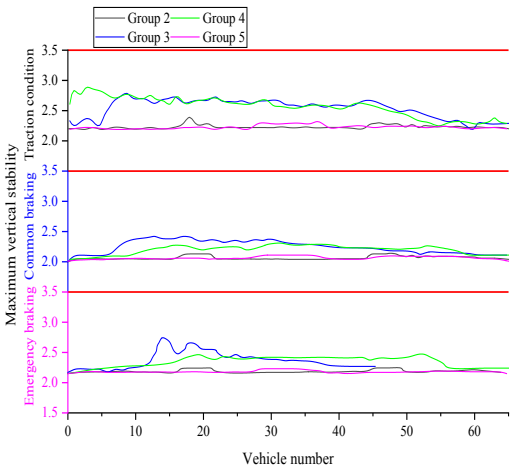

Fig.2 Maximum vertical stability

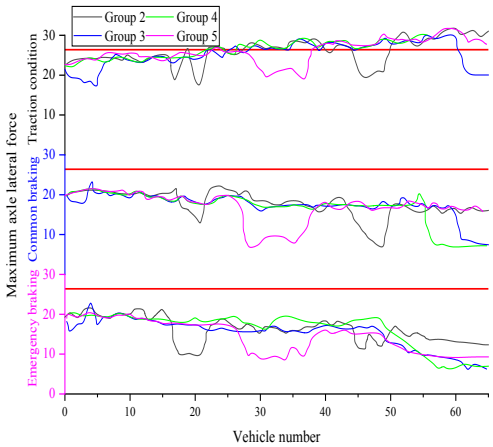

Fig.3 Maximum axle lateral force

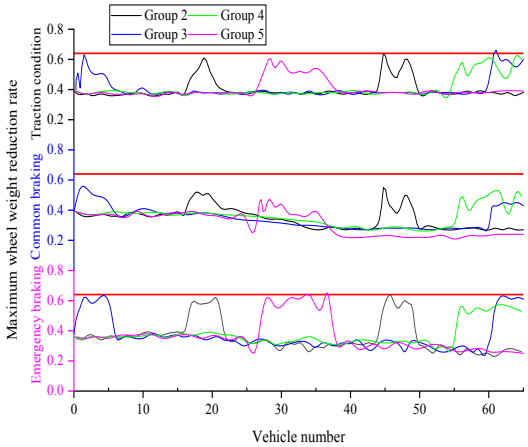

Fig.4 Maximum wheel weight reduction rate

When the axle lateral force is calculated, it is divided into a straight line and curve. The radius of the curve is R=600 m, and the length of the transition curve is 110 m. In common braking, the decompression is 70 kPa. Each group passes through the straight line and curve at the speed of 80 km/h, 85 km/h, and 90 km/h under three passing modes (traction condition, common braking, and emergency braking), and the lateral force of the three passing modes are obtained respectively. After the statistics are done, it is found that at the same speed, the higher the speed is when crossing the curve, the more obvious it is squeezed by the outer rail. Therefore, under the three passing modes, the lateral force reaches its maximum value at the curve and the speed of 90 km/h. Therefore, this state represents the

maximum lateral force, as shown in Fig.3. The red line with the value of 26.4 represents the upper limit of the calculated lateral force as “excellent”.

As can be seen from Fig.3, in the three passing modes, the axle lateral force of each group decreases in the number part of the empty vehicle. When passing through the curve without braking, the extrusion of the outer rail is the most obvious because of the high speed. As for the common braking and emergency braking, the lateral force of the rear wheel is significantly reduced due to the gradual decrease of the speed when passing through the curve. In the case of traction condition, the maximum axle lateral force of each group is close to the value of 26.4, and the other cases do not exceed the upper value of 26.4, reaching the “excellent”.

When calculating the wheel weight reduction rate, it is divided into straight lines and curves, the radius of the curve is R=600 m, and the length of the transition curve is 110 m. In common braking, the decompression is 70 kPa. Each group passes through the straight line and curve at the speed of 80 km/h, 85 km/h, and 90 km/h under the three passing modes (traction condition, common braking, and emergency braking), and the wheel reduction rate of the three passing modes are obtained respectively. After the statistics, it is found that at the same speed, the wheel weight reduction rate is larger when crossing the curve. The higher the speed is, the greater the wheel weight reduction rate is. Under the three passing modes, the wheel weight reduction rate reached its maximum value at the curve and the speed of 90 km/h, so this state is taken to represent the maximum wheel weight reduction rate, as shown in Fig.4. The red line with a value of 0.64 in the Fig. indicates that the wheel weight reduction rate is the "first limit".

As can be seen from Fig.4, in the three passing modes, due to the lightweight of the empty vehicle, the wheel weight reduction rate of each group increases in its empty vehicle number part. Under the traction condition, because the speed remains unchanged, the wheel weight reduction rate of each group remains unchanged. Under common braking and emergency braking, the wheel weight reduction rate of each group decreases gradually due to the decrease of speed. The maximum wheel weight reduction rate of each group in the empty vehicle number part is close to 0.64, and the other cases do not exceed the upper limit, reaching the “first limit”.

When calculating the derailment coefficient, it is divided into the straight line and curve, the radius of the curve is R=600 m, and the length of the transition curve is 110 m. In common braking, the decompression is 70 kPa. Each group passes through the straight line and curve at the speed of 80 km/h, 85 km/h, and 90 km/h under three passing modes (traction condition, common braking, and emergency braking), and the derailment coefficient of the three passing modes are obtained respectively. The derailment coefficient when passing through the curve at the speed of 90 km/h is the maximum under the three passing modes, as shown in Fig.5. The red line with the value of 1.2 indicates that the calculated derailment coefficient is the “first limit”.

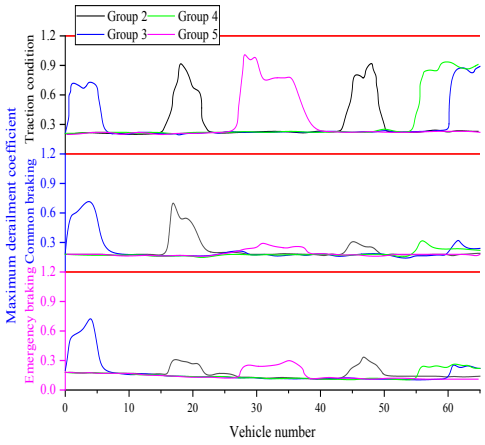

Fig.5 Maximum derailment coefficient

As can be seen from Fig.5, under the traction condition, the derailment coefficients of all groups in the empty part increase as the train pass through the curve at the speed of 90 km/h. For common braking and emergency braking, the speed begins to decrease when crossing the curve, so the part at the back of the empty train number decreases rapidly, finally is close to the derailment coefficient of the heavy train part. The maximum derailment coefficient of each group does not exceed the upper limit, reaching the “first limit”.

3 Experimental study

3.1 Experimental method

Vehicle dynamics test refers to the calculation of derailment coefficient and other dynamic performance based on the measured data of <GB/T 5599-1985 Code for Dynamic Performance Evaluation and Test Identification of Railway Vehicles> using a force measuring wheelset. Fig.6 shows the force measuring wheelset and data acquisition equipment in the test site.

(a) Force measuring wheelset

(b) Data acquisition equipment

Fig.6 Vehicle dynamics test site drawing

The wheel-rail lateral force Q and wheel-rail vertical force P are measured by force measuring wheels [15-16]. 4 force measuring wheelsets are selected, and the tread wear state is 2 new spins, and the other 2 wheels is abrasion value of 3mm. The measuring patch layout is shown in Fig.7.

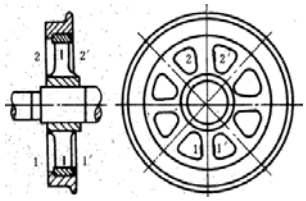

(a) Vertical force measurement

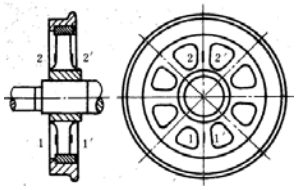

(b) Lateral force measurement

Fig.7 The measuring patch position

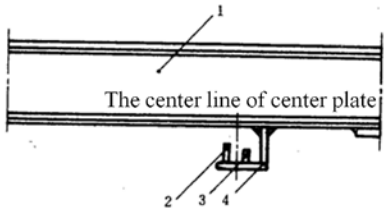

Fig.8 Acceleration sensor installation diagram

Fig.8 shows the installation diagram of the acceleration sensor. The acceleration sensor for measuring the vertical and lateral acceleration of the train body is installed on the lower cover plate of the middle beam of the chassis of the 1 or 2 inner core plate which is less than 1000 mm from the centerline of the core plate. Among them, 1 is the middle beam, 2 and 3 are the vertical and lateral acceleration sensors, and 4 is the installation iron.

After getting data, the proportional coefficient $K_p$and K_q of vertical and lateral force and their mutual influencing factors E_{qp} and E_{pq} can be obtained from Equation 3-6.

Vertical force proportional coefficient:

$$K_p = \varepsilon_{pp}/P \tag{3}$$

Lateral force proportional coefficient:

$$K_q = \varepsilon_{qq}/Q \tag{4}$$

The influence coefficient of vertical force on lateral force bridge:

$$E_{qp} = \varepsilon_{qp}/P \tag{5}$$

The influence coefficient of lateral force on vertical force bridge:

$$E_{pq} = \varepsilon_{pq}/Q \tag{6}$$

You can get the coefficient matrix $K = \begin{vmatrix} K_p & E_{qp} \\ E_{pq} & K_q \end{vmatrix}$, and calculate its inverse matrix K^{-1}, and take the first group of the strain of the right wheel as an example, the calculation formula of vertical force P and lateral force Q is as follows:

$$P = K^{-1}(1,1) \times A(:,1) + K^{-1}(1,2) \times A(:,2) \tag{7}$$

$$Q = K^{-1}(2,1) \times A(:,1) + K^{-1}(2,2) \times A(:,2) \tag{8}$$

In the equation, *A(:,1)* is the first group of the vertical strain of the right wheel, and *A(:,2)* is the first group of the lateral strain of the right wheel.

3.2 The analysis of data

To select the most dangerous test section for the subsequent reciprocating test, the vertical force and lateral force of the wheels are collected through the whole line pull test with no load. Vehicle dynamics tests are carried out on group 2, group 3, group 4, and group 5, and the measured results are averaged, and the maximum value of the data in this group is taken as the upper limit of the error bar. The result is shown in Fig.s 10-15. In Fig. 2, Fig. 3, Fig. 4, and Fig. 5 represent group 2, group 3, group 4, and group 5 respectively; NB, CN, and EB respectively represent traction condition, common braking, and emergency braking; CT4 and CT5 represent the whole-course pull test of group 4 and group 5, respectively.

Fig.9 and Fig.10 respectively show the axle lateral forces of group 2, group 3, group 4, and group 5 when passing through straight lines and curves. The red line of 26.4 represents the upper limit of the calculated axle lateral force. Under the same condition, the axle lateral force at the curve is larger, the reason is that the lateral component force generated by centrifugal force is larger. When passing through the straight line, the axle lateral force of group 3 and group 4 is relatively small under the traction condition, the reason is that there is no extrusion of the front and rear vehicles, and the vehicles run smoothly. Under common braking, the rear train will squeeze the front train, causing the axle lateral force larger; In emergency braking, its characteristics are similar to those of common braking in the absence of relatively insufficient rear braking. However, in the case of relatively insufficient rear braking, the rear wheels of the test vehicle will be squeezed and the axle lateral force will increase. When passing through the curve, the axle lateral force is small under the common braking, and the reason is that the speed decreases and the wheel subjected to the rail force decreases. Due to the whole pull-on test of group 4 and group 5, their lines contain straight lines and curves, and their maximum value appears in the curve section, so their derailment coefficient is larger. There is no obvious rule for each test parameter of the vehicles running at different speed levels, which might be similar running speed levels, and there is a certain speed error in the actual running, that is, 80 km/h is between 79-82 km/h, 85 km/h is between 83-87 km/h, and 90 km/h is between 88-90 km/h. The maximum axle lateral force of each group does not exceed 26.4, reaching the "excellent".

Fig.11 and Fig.12 respectively show the wheel weight reduction rate of group 2, group 3, group 4, and group 5 when passing through the straight line and curve. The red line with the value of 0.64 represents the "first limit" of the wheel weight reduction rate. In the same case, due to the greater effect of the outer rail on the wheel when

passing through the curve, the vertical component force between the wheel and the rail increases, then the wheel weight changes greatly. When passing through the straight line, the wheel weight reduction rate is small under the traction condition, because the extrusion pressure of each group is small before and after the vehicle in the absence of braking. In common braking and emergency braking, the rear vehicle squeezes the front vehicle, resulting in a larger wheel weight reduction rate. With the increase of the speed of each vehicle, the wheel weight reduction rate becomes larger. When passing the curve, the higher the speed is, the higher the wheel weight reduction rate is. At the same speed, the wheel weight reduction rate in the traction condition is higher than that in the braking condition. This is because the wheelset load reduction caused by the vehicle passing at a higher speed is greater than that caused by the extrusion of the front and rear vehicles due to braking. Since group 4 and group 5 are carried out the whole pull-on test, their lines contain a straight line and curve, and its maximum value appears in the curve section, so the maximum value is obtained when passing through the straight line and the curve. The wheel weight reduction rate of each group is no more than 0.64, reaching the "first limit".

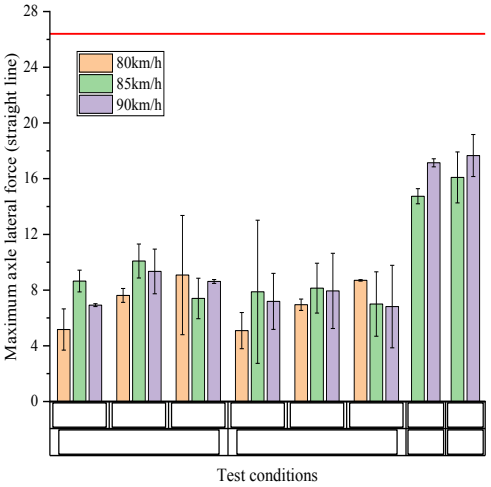

Fig.9 Maximum axle lateral force (straight line)

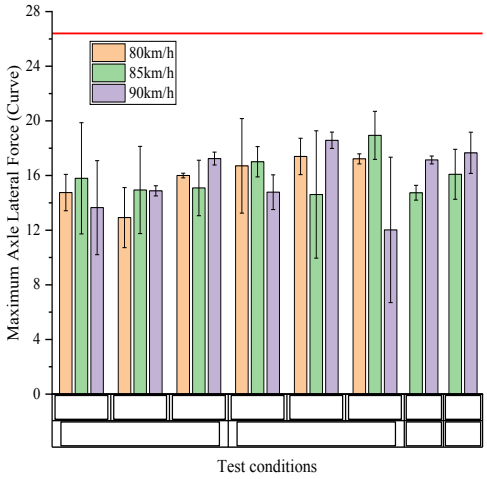

Fig.10 Maximum axle lateral force (curve)

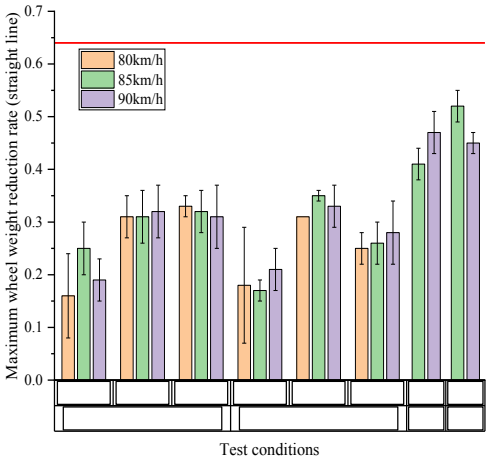

Fig.11 Maximum wheel weight reduction rate (straight line)

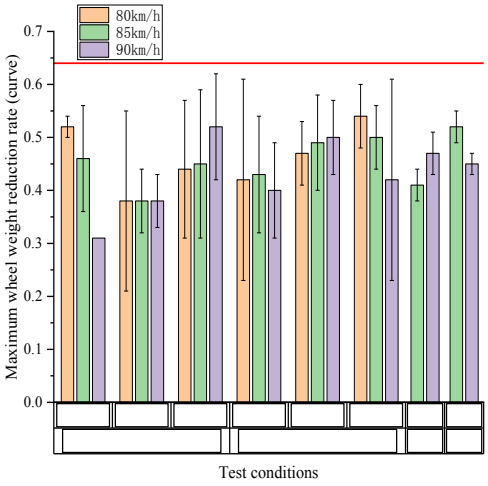

Fig.12 Maximum wheel weight reduction rate (curve)

Fig.13 and Fig.14 respectively show the derailment coefficient of group 2, group 3, group 4, and group 5. The red line with the value of 1.2 indicates that the derailment coefficient is the "first limit". In the same case, the derailment coefficient is larger when passing through the curve than when passing through the straight line. When passing through the straight line, under the same marshaling mode, there is no obvious rule of test parameters for each marshaling vehicle running at different speed levels. When passing through the curve, compared with the traction condition, the speed of common braking decreases gradually, so the derailment coefficient is low. Compared with emergency braking, the extrusion pressure of front and rear vehicles under common braking is smaller, so the derailment coefficient is smaller. Group 4 and group 5 are carried out the whole pull-on test. The circuit of

group 5 included the straight line and the curve, and its maximum value appeared in the curve section. Therefore, the maximum value is obtained when passing through the straight line and the curve, so the value in Fig.13 and Fig.14 is the same. The derailment coefficient of each group does not exceed the upper limit, reaching the "first limit".

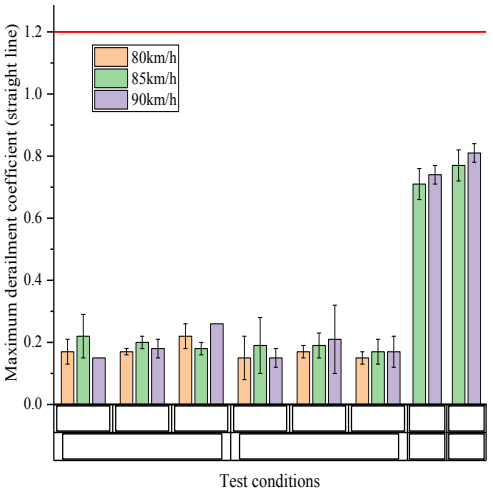

Fig.13 Maximum derailment coefficient (straight line)

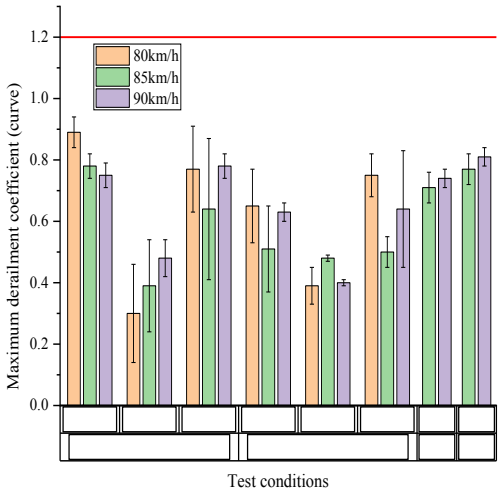

Fig.14 Maximum derailment coefficient (curve)

4 Conclusion

Based on the modular modeling method, the dynamic model of the long marshaling empty-heavy mixed freight train is established, and the dynamic characteristics of the vehicle system under different marshaling modes and operating conditions are discussed theoretically. The result shows that the dynamic performance of empty freight trains is lower than that of heavy freight trains due to the longitudinal impulse action during the traction and braking process, and the dynamic performance of empty freight trains is the worst when it is in the rear position. Based on the theoretical calculation, the experimental tests are carried out under conditions with bad dynamic performance. The result shows that the theoretical calculation is in good agreement with the experimental tests. In the selected speed-up section, all the dynamic performance indexes of the empty-heavy mixed freight train meet the speed-up requirements. Therefore, theoretical calculation and experimental test can complement and verify each other, and provide an important guarantee for reasonable speed-up of freight train.

Acknowledgments: The authors gratefully acknowledge the support of the School-enterprise cooperation projects (No.20200203)

References

[1] Zhai W, Cai C, Wang Q, Lu Z, Wu X. Dynamic effects of speed-raise train on the track and the countermeasures 2000(03): 13-22.

[2] Yu S. Analysis on the influence of railway freight train speed increase on vehicles and study on maintenance opinions 2019(05): 154-155.

[3] Liu Z. Bogie structures of speed-rising freight train 2003(03): 286-289.

[4] Wu P, Wen S, Wang J, Lan Q. Fatigue life prediction on the side frame of ZK2 bogie of the speed-increased freight train 2009, 30(01): 91-95.

[5] Chen L, Lu K, Yu W, Wang H. Reliability analysis method for the lateral dynamics performance of the speed-increased wagon 2009, 30(03): 97-102.

[6] Gong K, Xiang J, Liu L. Track strengthening measures assessment of heavy haul railway based on freight train anti-derailment safety degree 2020, 51(03): 832-841.

[7] Chen L, Wang X. Analysis of the dynamic performance of the 120 km/h speed increased comprehensive testing freight trains 2007(08): 27-34+55-56.

[8] Zhan H. Influence analysis and maintenance suggestions of railway freight train speed increase on vehicles 2015, 13(10): 56.

[9] Qin Z. Influence of speed boost of the railway on freight trains 2014(04): 208-209.

[10] Xue P. Research and application of lateral movement stability of accelerated locomotive and vehicle 2019, 5(09): 193-194.

[11] Li T, Wang Q, Piao M. Wheelset self-stability and MBS simulations of speeding-up railway 2021, 38(02): 103-109.

[12] Fu B, Luo S, Ma W, Tang Y. Dynamic analysis of key parameters of bogie to speed-raising metro vehicle 2018(01): 12-14+18.

[13] Wu Y. Improvement and development direction of railway freight train speedup in china under the background of speedup 2008, 24(3): 70-71.

[14] Chi M, Jiang Y, Zhang W, Wang Y. System dynamics of long and heavy haul train 2011, 11(03): 34-40.

[15] Yang X, Chen J. Wheel rail force measurement method based on wheel and axle strain 2014(08): 141-142.

[16] Ren Y, Chen J, Lin J. A blind signal separation based measurement of the wheel/rail force of an instrumented wheelset 2010, 29(3): 289-292.

Viser Technology Pte. Ltd.
Mechanical Engineering Science
DOI: 10.33142/mes.v3i1.4333

Research Article Open Access

Research on Leak Location of Liquid-filled Pipe Based on Frequency Dispersion Characteristics

Lijun XIONG[1], Ping LU[2]*, Yun YANG[1], Li LI[1]

1 School of Mechanical Engineering, Southwest Jiaotong University, Chengdu, China
2 State Key Laboratory of Traction Power, Southwest Jiaotong University, Chengdu, China

***Corresponding Author:** Ping LU, No.111, North 1st Section,2nd Ring Road, Chengdu City,610031, China; 277717386@qq.com*

Abstract:
Due to the material problems and force majeure factors, the leakage will be occurred on the liquid-filled pipe resulting in waste of resources, environmental pollution and even endangering safety. Acoustic wave detection technology is widely used in buried pipeline leak detection, this technology mainly uses the wave (n=0, s=1) in the pipeline acoustic wave to locate the leak. When the leakage acoustic signal propagates along the liquid-filled pipe, the frequency dispersion characteristics can be obtained by wavelet decomposition. And there is a time delay (time difference) value between the leaky acoustic signals collected by the sensors at both ends of the leak. The outputs show that the results obtained by wavelet decomposition are in good agreement with the theoretical calculation results. Based on the obtained dispersion relation, the time delay values at different characteristic frequencies are analyzed by the cross-correlation method, and the leak location accuracy is discussed. This research content provides theoretical support and engineering application guidance for pipe leakage location technology.

Keywords: *Liquid-filled pipe; Frequency dispersion characteristics; Leak location; Time delay estimation value*

1 Introduction

With the progress of urbanization in China, the number of underground liquid-filled pipes in cities and towns is increasing. According to statistics, the total length of liquid-filled pipe is 8668.2 million kilometers, the annual water supply volume is 61.5 billion cubic meters in China[1].In the context of urbanization, buried water supply pipelines are inevitably damaged due to self-aging or force majeure factors. When the liquid-filled pipe is leaking and cannot deal with it in time, it may cause waste of resources and major safety accidents. Moreover, according to relevant statistics, the average leakage rate of the urban water supply system is 21.5% in China[2], but the standard leakage rate needs to be controlled at 10%[3]. The leakage rate of the water supply pipelines is not up to the standard. To cut down the waste of water resources and prevent safety accidents, it is important to locate the leakage point of liquid-filled pipe in time and accurately.

At present, there are many kinds of research results on acoustic leak detection and positioning. J M Muggleton[4] *et al* proposed that the acoustic generated by the leakage of buried pipe propagates at a relatively low frequency, it includes axisymmetric waves with n=0 and n=1. Here, the n=0, s=1 wave occupies the main part of the leakage acoustic signal. R J Pinnington[5] *et al* had studied the coupling equation of the axisymmetric wave in the buried liquid-filled pipes, introduced the mathematical correlation between the speed of the axisymmetric wave and the wavenumber of free fluid. The determination of the wavenumber depends on the pipeline parameters, and these parameters do not have enough time to determine in actual engineering. By studying the coupling equation of buried liquid-filled pipe under vacuum, Fuller and F J Fahy[5] obtained the dispersion characteristic curve of acoustic signal of leakage point at low frequency. The dispersion characteristics are limited to vacuum pipelines, it may vary in the actual pipeline. By studying plastic pipes, Osama Hunaidi[7] *et al* found that the frequency characteristic of leakage acoustic signals is different in different environments and the leakage signal of plastic pipes has dispersion characteristics. The frequency range of the research is small, the frequency can increase appropriately. Based on the cross-correlation location algorithm, Shuaiyong Li[8] *et al* proposed the wave speed of the signal can be determined by the frequency of the signal in gas pipes, then determined the location of the leakage point. Using the above article for reference, it can

Received 25 February 2021; Accepted 13 April 2021

be clarified that the wave speed of the leakage acoustic signal of the liquid-filled pipe can be determined by its dispersion characteristics. Gao Y[9] *et al* proposed to use spectral analysis algorithm to determine the location of the leakage point, Yan Hongmei[10] studied the propagation characteristics of leakage acoustic signals in the buried liquid-filled pipeline, located the leakage point according to its propagation characteristics. According to references 9 and 10, it can be used to analyze the characteristics of the leakage signal and select the characteristic frequency band. The above researches show, the leakage acoustic signal has dispersion characteristics, and the dispersion characteristics can be solved by numerical calculation with the help of some parameters.

After obtaining the dispersion characteristics and characteristic frequency bands of the leakage sound signal, try to locate the leakage point. Before locating the location of the leakage point on the underground liquid-filled pipe, it is necessary to predetermine the dispersion characteristics of the leakage acoustic signal under actual conditions. An intrinsic property of the pipeline and the environment related to the wave speed, which needs to study and get the actual pipe dispersion characteristics.

Regarding the determination of the location of the leakage point of the liquid-filled pipe, the main difficulty lies in the calculation of the wave speed and the time delay. If the wave speed or the time delay produces errors, it will affect the determination of the leak location of the liquid-filled pipe. The study found that the frequency distribution of leakage acoustic signal in the low-frequency portion, and leaked acoustic signals may be covered by noise at low frequencies. To ensure the accuracy of locating the leakage point of the liquid-filled pipe, a band-pass filter is used to de-noising the measured signal based on the power spectral density characteristics of the measured signal. Then, try to obtain the dispersion characteristics and time delay. After obtaining the wave speed and time delay according to the actual situation, the accuracy of locating the leakage point of the liquid-filled pipe can be improved.

2 Theoretical research

In urban liquid-filled pipes, due to the presence of fluid, the water pressure is inevitable. When the pipe is damaged due to some reasons, a leakage acoustic signal will be generated at the damaged place due to the pressure difference between the inside and outside, and the leakage acoustic signal will propagate along the liquid-filled pipe to both ends of the leakage point. For the location of the leakage point of the liquid-filled pipe, the key is to determine the wave speed and time delay of the leakage vibration signal. If the calculated wave speed and time delay values are close to the actual situation, the accuracy of the leakage point location will be improved.

2.1 Positioning theory

When the pipe leaks, sensors are arranged at both ends of the leak point, then the sensors will collect the leakage acoustic signals that propagate along the pipeline to the measuring point. The leak location theory bases on propagation characteristics of the leakage acoustic signal, and liquid-filled pipe leak location model as shown in Fig.1.

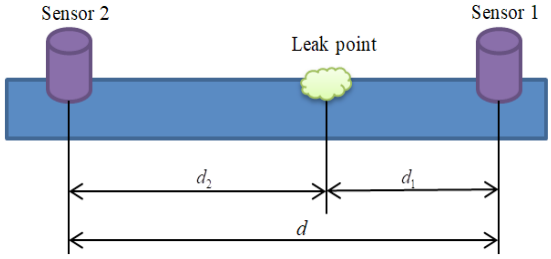

Fig.1 Liquid-filled pipe leak location model

In Fig. 1, two sensors are arranged at measuring point 1 and point 2, and the signals collected by the two sensors are $x_1(t)$ and $x_2(t)$, the distance between the two measuring points and the leak point is d_1 and d_2; the distance between the two measuring points is d. The model of the vibration signal collected by the sensors at the two measuring points is:

$$\begin{cases} x_1(t) = \alpha_1 s(t) + n_1(t) \\ x_2(t) = \alpha_2 s(t-\tau) + n_2(t) \end{cases} \quad (1)$$

Among them, $s(t)$ is the acoustic signal that generates at the leak point,n_1(t) and n_2(t)are uncorrelated noise signals, α_1 and α_2 are the attenuation of the leakage vibration signal propagate to the measuring points 1 and 2. Assuming that the time taken for the leakage acoustic wave signals to propagate to sensor 1 is t_1, the time taken to propagate to sensor 2 is t_2, the time delay value is $\tau=t_1-t_2$, which represents the time difference between the acoustic signal at the leak point reaching the sensor 1 and sensor 2.

Assuming that the acoustic signal at the leak point propagates along the pipe to both sides of the pipe at a constant wave speed, set this speed as v, and the time delay obtained by an algorithm is τ.

$$d_1 = \frac{d + v\tau}{2} \quad (2)$$

$$d_2 = d - d_1 \quad (3)$$

In the project, the time delay is calculated by using the cross-correlation algorithm[11], adaptive algorithm[12] and generalized cross-correlation algorithm, etc. The cross-correlation algorithm is easy to use and takes a short time, the cross-correlation algorithm is taken to determine the time delay estimation value here.

It can be seen from Fig.1 and formula 1, the acoustic signals measured by the sensor are $x_1(t)$ and $x_2(t)$ respectively. Before using the cross-correlation algorithm to determine the time delay estimation value, it is necessary to perform de-noising processing on the measured signal, and the signals that are obtained after de-noising processing are $X_1(t)$, $X_2(t)$.In fact, $X_1(t)$ and $X_2(t)$are discrete signals, but when the sampling frequency is high, it can be regarded as a continuous signal during calculation. The cross-correlation function of the two signals after de-noising processing is $R_{X_1X_2}(\tau)$, and the cross-correlation coefficient is $\rho_{X_1X_2}(\tau)$.

$$R_{X_1X_2}(\tau)=\int_0^{+\infty}X_1(t)X_2(t+\tau)dt \tag{4}$$

$$\rho_{X_1X_2}(\tau)=\frac{R_{X_1X_2}(\tau)-\overline{X_1}\,\overline{X_2}}{\sqrt{D(X_1)}\sqrt{D(X_2)}} \tag{5}$$

In formula 5, $\overline{X_1}$ and $\overline{X_{1(t)}}$respectively the mean of $X_1(t)$ and $X_2(t)$; $\sqrt{D(X_1)}$ and $\sqrt{D(X_2)}$ respectively the standard deviation of $X_1(t)$ and $X_2(t)$; τ is the time delay estimation value.

From the definition of the correlation coefficient, if the leakage vibration signal $X_1(t)$ and $X_2(t)$ is correlated, a series of correlation coefficients can be obtained, and there is $|\rho_{X_1X_2}(\tau)|\le 1$. When the correlation coefficient of the two leakage vibration signals reaches the maximum, the most accurate time delay estimation value can be obtained, and $\tau_{\max}=\arg\max(\rho_{X_1X_2}(\tau))$.

In the actual application of the location of the leakage point of the liquid-filled pipe, the wave speed v is related to the pipe and the surrounding environment of the pipe and is not a constant value. Three sensors are arranged on the liquid-filled pipe, two of which can be used to determine the wave speed of the leakage vibration signal [13], but the wave speed is measured by this method inaccurately. According to the material properties of the pipe and the coupling equation, the propagation speed can be derived [14], and the speed on some parameters is difficult to get in a short time. Given the shortcomings of the above two methods, a method that can determine the wave speed at the corresponding frequency according to the dispersion characteristics can be adopted.

2.2 Axisymmetric wave propagation characteristics

In the leakage point positioning model of the liquid-filled pipe, when calculating the distance between the measuring point 1 and the leakage point, the propagation speed of the vibration signal of the leakage point is a certain value theoretically, but in actual engineering applications, the wave speed is changing. By the coupling equation of buried liquid-filled pipes, the propagation characteristics of the leaky acoustic signal in a liquid-filled pipe can be derived, and the propagation speed of the leakage acoustic signal in the pipe can be determined.

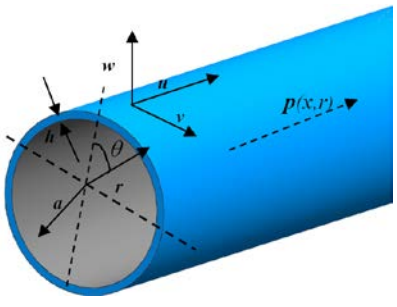

Fig.2 The coordinate system of buried liquid-filled pipe

In the coordinate system, the buried liquid-filled pipe shown in Fig.2, u represents the axial displacement of the shell, w represents the radial displacement of the shell, v represents the tangential displacement of the shell, $p(x,r)$ represents the fluid pressure, a represents the shell radius, h represents the shell wall thickness.

In the buried liquid-filled pipe, the axial force and radial force inside the pipe are in a balanced state, which can be obtained:

$$\rho\ddot{u}=-\partial\sigma_x/\partial x \tag{6}$$

$$p(a/h)=\sigma_\theta+\rho a\ddot{w} \tag{7}$$

$$\sigma_\theta=\frac{E}{1-v^2}\left(\frac{w}{a}+v\frac{\partial u}{\partial x}\right) \tag{8}$$

$$\sigma_x=\frac{E}{1-v^2}\left(\frac{\partial u}{\partial x}+v\frac{w}{a}\right) \tag{9}$$

In the above formulas, E is Young's modulus of the pipe, w/a is the circumferential strain, v is the Poisson's ratio, $\partial u/\partial x$ is the axial strain, and ρ is the pipe density; σ_θ is the axial stress, σ_x is the circumferential stress.

Combining formula 6 and formula 9, get:

$$\rho\ddot{u}+\frac{E}{1-v^2}\left(\frac{\partial^2u}{\partial x^2}+\frac{v}{a}\frac{\partial w}{\partial x}\right)=0 \tag{10}$$

Combining formula 7 and formula 8, get:

$$\frac{E}{1-v^2}\left(\frac{w}{a}+v\frac{\partial u}{\partial x}\right)+\rho a\ddot{w}=\frac{pa}{h} \tag{11}$$

In formula 10 and formula 11, the axial displacement u, the radial displacement w, and the amplitude of the axial motion of the soil medium U_s, the amplitude of the radial motion W_s have the following relationship: $u=U_s e^{i(\omega t-k_s^r x)}$, $w=W_s e^{i(\omega t-k_s^r x)}$. And $(k_s^r)^2=k_f^2-k_s^2$, in here: k_s^r is the radial wave number, k_f is the free fluid wave number, k_s represents the wavenumber of axisymmetric wave s=1 or s=2.

Combining formula 7 and formula 8, get:

$$\left(\Omega^2-\alpha_s^2\right)U_s=\mathrm{i}v\alpha_sW_s \tag{12}$$

$$W_s\left(1-\Omega^2\right)-\mathrm{i}v\alpha_sU_s=\left(\frac{P_sa^2}{hE}\right)\left(1-v^2\right)\mathrm{J}_0\left(\alpha_s^r\right) \tag{13}$$

In formula 12 $a_s=k_sa$, and $\Omega=k_La$, the compression wave number $k_L^2=w^2\rho(1-v^2)/E$. In formula 13, the relationship is $p=\sum_{s=1}^{2}P_sJ_0\left(k_s^rr\right)e^{i(\omega t-k_s^rx)}$ between p and P_s.

Combining formula 12 and formula 13, get:

$$W_s=\left(1/\rho_f\omega^2\right)P_s\left(\alpha_s^r/a\right)J_0'\left(\alpha_s^r\right) \tag{14}$$

$$P_s=\frac{-2B}{1-\left(\alpha_s/\alpha_f\right)^2}\frac{W_s}{a} \tag{15}$$

In the buried liquid-filled pipe, the first type of s=1 wave in the axisymmetric wave (n=0) accounts for most of the leakage acoustic signal, $k_1^2\gg k_L^2$.When studying the dispersion characteristics, only the s=1 wave is discussed. By combining formula 11 and formula 15, get the wavenumber of s=1, $k_1=k_f^2(1+2Ba/(Eh+i\alpha Eh))$ [15], and B is the bulk elastic modulus of the fluid in the pipe, and α is the attenuation factor. From the expression, k_1 is a complex number, and the real and imaginary parts have a mathematical relationship with the wave speed and attenuation coefficient respectively. By calculating, the specific corresponding relationship can be seen In Fig. 3 and Fig. 4.

In Fig. 3 and Fig. 4, the real and imaginary parts of the s=1 wave are both curves which indicate that the wave speed and attenuation change with the frequency at all times, that is the leakage acoustic signal exists dispersion characteristics when it propagates in the pipe. The situation in Fig.3 shows that in the process of locating the leakage point of the liquid-filled pipe, the wave speed of the acoustic signal leaking in the pipe cannot be regarded as a constant value. Otherwise, it will have a great impact on the accuracy of the positioning. In Fig.4, the imaginary part of the s=1 wave does not all gradually increase. In the vicinity $k_f a = 0.06$, the imaginary part of the s=1 wave reaches a peak, which may be due to resonance between the liquid-filled pipe and the earth, and it can be used to measure the frequency of the earth. According to the propagation characteristics of the leakage acoustic signal, its dispersion characteristics can be deduced, which can improve the positioning accuracy.

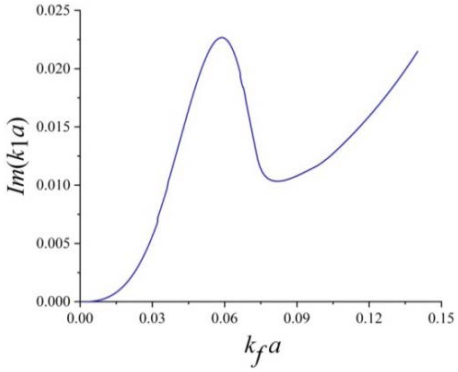

Fig.3 The relationship between the real part of s=1 wave and $k_f a$

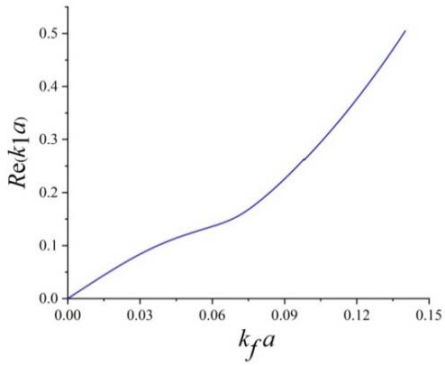

Fig.4 The relationship between the imaginary part of s=1 wave and $k_f a$

To obtain the frequency dispersion characteristics of the leakage vibration signal, the relationship among $k_f a$, $Re(k_1 a)$ and $Im(k_1 a)$ can be converted into the relationship between angular frequency, wave speed, and attenuation, and the results are shown in formula 16 and formula 17.

$$c_1 = a\,w/\mathrm{Re}(k_1\,a) \tag{16}$$

$$Loss(dB/m) = -20\frac{\mathrm{Im}(k_1 a)}{\ln(10)} \tag{17}$$

In formula 14, $w = k_f c_f$ is the angular frequency, c_f is the speed of the free fluid, k_f is the free fluid wave number. In here, $c_f = \sqrt{B_f/\rho_f}$, and B_f is the elastic modulus of the fluid, ρ_f is the density of the fluid.

The calculation results of formula 14 and formula 15 showed that the leakage acoustic signal has the frequency dispersion characteristic. The dispersion characteristics are related to the characteristics of the pipe material. Some material characteristics of the pipe can see Table 1.

Table 1 Material characteristics

Material	Density(kg/m^3)	Young's modulus (N/m^2)	Bulk's modulus (N/m^2)	Poisson's ratio	Loss
Fluid	1000	--	2.25×10^9	--	--
Pipe	2000	5.0×10^9	--	0.4	0.065
Medium	2000	--	4.5×10^9	--	--

3 Experimental Research

From a theoretical point of view, the determination of the location of the leakage point lies in the determination of the wave speed and the time delay. Combining the dispersion characteristics and characteristic frequency bands, the wave speed of the leaking acoustic signal can be obtained. The frequency spectrum analysis of the signal is used to find the characteristic frequency band that contains the most information of the leakage vibration signal, and filter out the signals of the remaining frequencies by the band-pass filter. The final signal should contain less noise information and more leakage acoustic signal information. Use a cross-correlation algorithm to do correlation analysis of two final signals, and obtain the cross-correlation function. When the degree of cross-correlation function between the two signals is the largest, the corresponding time is the time delay. The wave speed in the characteristic frequency band can be obtained by the dispersion characteristic curve, then under the condition of obtaining the wave speed and time delay in the characteristic frequency band, the leakage point of the liquid-filled pipe can be located.

To verify the feasibility of the theory, a field experiment was done in the school. Taking the school's water supply pipelines as the experimental object, the situation when the fire hydrant is opened is regarded as a pipe leakage condition, a sensor is arranged on the pipe under the manhole cover at the left and right ends of the fire hydrant to measure the pipe leakage acoustic signal. Try to keep the surroundings quiet during the experiment to prevent sudden noise interference. The distribution of sensors and the opening of the fire hydrant during the experiment are shown in Fig.5 and Fig.6.

During the experiment, keep the two sensors located at the left and right ends of the fire hydrant respectively,

and name the sensors on the left and right sides of the fire hydrant as measuring point 1 and measuring point 2. Four sets of data were measured during the experiment: the first set: d_1=21.6, d_1=28.7; the second set d_1=21.6, d_2=42.3; the third set: d_1=32.9, d_2=28.7; the last set: d_2=32.9, d_2=42.3.

Fig.5 Open fire hydrant to simulate pipe leakage

Fig.6 Place sensors downhole

3.1 Signal acquisition and analysis

During the experiment, a sensor was arranged at the fire hydrant to measure the leakage acoustic signal. The time-domain signal collected by the sensor is shown in Fig.7. The power spectrum density of the signal at the fire hydrant can be calculated by the period diagram method, as shown in Fig.8. In Fig.8, there are three frequency bands with prominent peaks in the power spectral density (PSD). These three frequency bands may contain the information of leakage signal, and it can be seen from Fig.8 that the frequency ranges of band 1, band 2, and band 3 are 450 Hz. to 530Hz, 560Hz to 790Hz, and 1000Hz to 1200Hz, respectively.

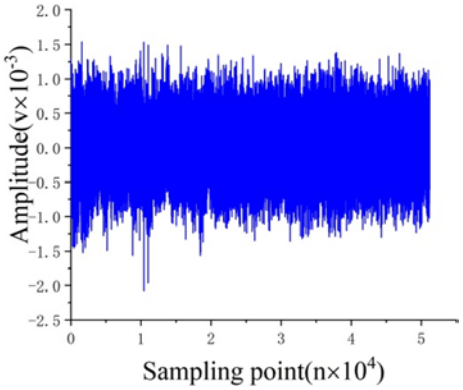

Fig.7 The time-domain signal measured at a fire hydrant

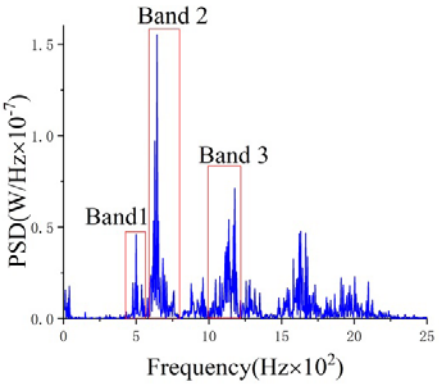

Fig.8 PSD of a signal at a fire hydrant

In the experiment, the leakage of a fire hydrant can simulate the leakage of pipe in water supply pipelines, and the signal measured by the sensor arranged at the fire hydrant can best represent the leakage acoustic signal. As shown in Fig.8, the PSD of the measured signal at the fire hydrant contains the three most representative frequency bands, and the characteristic frequency band of the leakage vibration signal may be in one or more frequency bands. In the process of leakage signal propagation, due to environmental noise and attenuation in the process of propagation, the leakage acoustic signal information contained in the signal measured at the measuring point may be lost or covered by the noise information. In the course of the experiment, in addition to the spectrum analysis of the signal at the fire hydrant, the power spectral density of the four groups of measured points is also analyzed, and the three frequency bands with prominent power spectral density are selected, and the frequency range is from small to large. The specific results are shown in Table 2.

Table 2 The frequency range where the PSD at the measurement point is prominent

Test group	Measuring point	Band 1(Hz)	Band 2(Hz)	Band 3(Hz)
Group 1	Point 1	470-570	580-800	1000-1400
	Point 2	480-560	570-800	1000-1400
Group 2	Point 1	470-550	570-800	980-1400
	Point 2	470-520	580-800	1010-1370
Group 3	Point 1	420-570	575-800	1020-1370
	Point 2	460-580	580-700	--
Group 4	Point 1	475-560	570-810	1020-1375
	Point 2	470-570	580-730	--

From Table 2, the three bands where the power spectral density of the measured signal is more prominent, band 1 and band 2 are different except for some measurement points, and the other measurement points are not different. The power spectral density of the measuring point 2 of the third and fourth groups does not have a third prominent frequency band, which may be that the high-frequency part of the leakage acoustic signal attenuates too much during propagation, so the noise covers the acoustic signal.

Based on band 1, band 2, and band 3 obtained from the spectrum analysis of the signal at the fire hydrant, the prominent frequency range of the power spectrum density at the measuring point and the fire hydrant is compared. For band 1, most of the frequency range obtained by measuring point signal includes the frequency range of the signal power spectrum density at the fire hydrant, which indicates that the leakage acoustic signal in this frequency range will not have a great change in the frequency range. For band 2, compared with the two frequency ranges, it is found that except for a few measuring points, the other points are not different, which indicates that although the leakage signal will be affected by the external environment during the propagation of the pipe, it is still within a reasonable frequency range. For band 3, the frequency range of the measured signal is larger than the standard frequency range or there is no prominent power spectrum density in the third segment, which indicates that the attenuation is too large here. That meant that band 3 is affected by noise and the pipe, the corresponding portion of the original signal and there is a big difference.

From the comparison results, the frequency range between the measuring points 1 and 2 and the fire hydrant is partially out of the way. In engineering, the use of a frequency characteristic of the measured signal would be difficult to select the frequency band. The frequency distribution range will be affected by human or environmental factors, and it's difficult to choose the right one. To make the result close to reality, the frequency distribution range at the fire hydrant can be assumed to be the frequency distribution of the measuring point.

3.2 Propagation characteristics verification

In the course of the experiment, the signal collected at point 1, point 2, and fire hydrant are decomposed by wavelet with the same number of layers, and the detail coefficient and approximate coefficient of the signal can be obtained respectively. Each set of coefficients corresponds to a specific frequency range; To calculate easily, regard the average frequency within that frequency range as the frequency range.

In theory, the relationship between angular frequency and wave speed and attenuation can be calculated by formulas 16 and 17 respectively, as shown in Fig.9 and the blue line in Fig.10. By the wavelet decomposition, the measurement signal is decomposed into signals at different frequencies. Then try to calculate the time delay by cross-correlation algorithm, get the wave speed of corresponding frequency finally.

In Fig.9, the average wave speed calculated by the four groups of corresponding measuring points is taken as the wave speed of the measuring point. In the experiment, the amplitude of the signal after wavelet decomposition can be used to calculate the attenuation at the corresponding frequency. In Fig.10, the attenuation calculated by the four groups of corresponding measuring points is taken as the average attenuation coefficient of the measuring point.

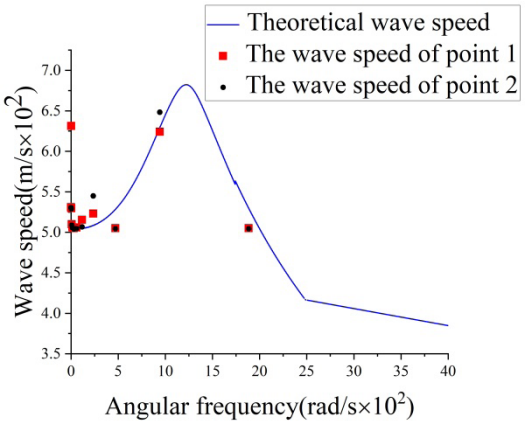

Fig.9 The relationship between angular frequency and wave speed

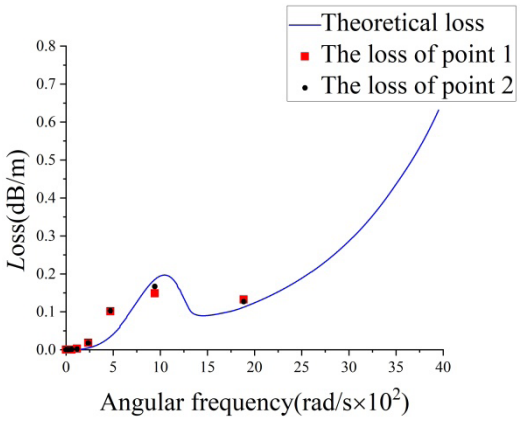

Fig.10 The relationship between angular frequency and loss

From Fig.9 and Fig.10, it can be seen that the results obtained by theoretical calculation and experimental calculation show that there is a dispersion characteristic when the leakage acoustic signal propagates in the liquid-filled pipe. The above-mentioned phenomenon indicates that when locating the leakage point of the pipe, the wave speed needs to be determined according to the characteristic frequency of the signal. Compared with the theoretical results, it is found that the experimental results and theoretical results of wave speed and attenuation are mostly consistent with the overall trend. In the aspect of wave speed, the place where there is a large deviation at low frequencies, and the reason may be the noise attached to the acoustic signal affects the calculation of the time delay, which will cause errors in calculating the wave speed.

3.3 Signal analysis

Before calculating the time delay by cross-correlation algorithm, the signal collected at the measuring point should be de-noised. From Fig.8, it can be seen that there are three bands with high power spectrum density in the measured signal, and the three bands have the possibility of containing the information of leakage acoustic signal. To determine the characteristic frequency band of leakage acoustic signal, take a frequency band as the research object individually. De-noising the measured signal based on the frequency domain characteristics of the leakage signal, which can retain the information of the leakage vibration signal to the greatest extent and reduce the influence of noise. After de-noise, the time delay can be obtained by cross-correlation algorithm, and take the average wave speed calculated from the measuring point as the propagation speed in the corresponding frequency range. Then the location of the leakage point can be determined by formula 2.

After the signal at the measuring point in the four groups of experiments is processed, the correlation between the degree of correlation $R_{X_1X_2}(\tau)$ and time τ is obtained by cross-correlation algorithm, the experimental calculation results as shown in Fig.11, Fig.12, Fig.13, and Fig.14. To make the calculation results clear, the time delay and the corresponding leakage point location error rates are listed in Table 3.

Table 3 Analysis of time delay calculation results of four sets of experiments

Test group	Band	TDE (s)	Wave speed (m/s)	Distance(m)	Error rate (%)
Group 1	Band1	0.02453	404.242	9.92	39.72
d1=21.6m	Band2	0.00672	942.243	6.33	10.84
d2=28.7m	Band3	0.01586	1220.000	19.35	172.54
Group 2	Band1	0.05828	404.242	23.56	13.82
d1=21.6m	Band2	0.02117	942.243	19.95	3.62
d2=42.3m	Band3	0.06695	1220.000	81.68	294.59
Group 3	Band1	0.00336	404.242	1.36	67.62
d1=32.9m	Band2	0.00523	942.243	4.93	17.38
d2=28.7m	Band3	0.01336	1220.000	16.30	288.10
Group 4	Band1	0.03031	404.242	12.25	30.32
d1=32.9m	Band2	0.00922	942.243	8.69	7.55
d2=42.3m	Band3	0.03766	1220.000	45.95	388.83

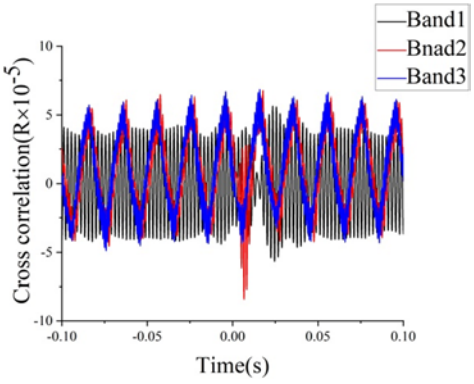

Fig.11 Estimated time delay of the first set

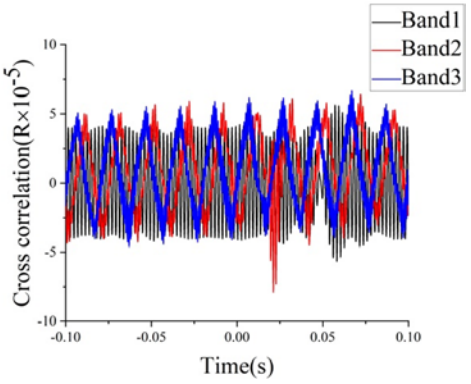

Fig.12 Estimated time delay of the second set

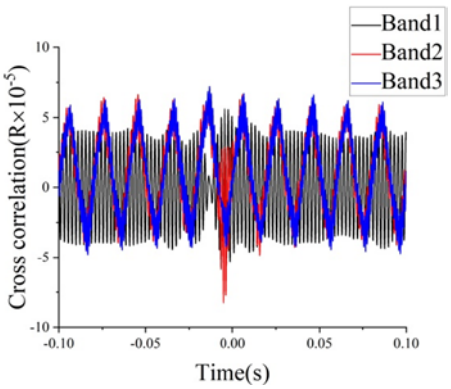

Fig.13 Estimated time delay of the third set

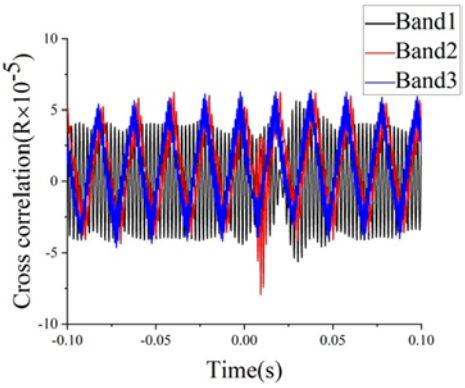

Fig.14 Estimated time delay of the last set

In Table 3, the predicted wave speed is calculated by the theoretical angular frequency and wave speed curve in Fig.9, and the average wave speed in the corresponding frequency range represents the wave speed of the frequency band. Since the frequency range given in Fig.9 is limited, so the wave speed that is not in the frequency range can take the experience wave speed is based on the nature of the pipe. After a series of processes, the wave speed can be obtained and the wave speeds of band 1, band 2, and band 3: 404.242 m/s,942.243m/s, and 1220 m/s respectively. In Table 3, TDE is the time delay estimation value.

In the field experiment, the layout of the sensor is determined according to the position of the manhole cover on the campus. Two manhole covers are taken on each side of the fire hydrant, and the two-by-two combination can be four groups of experiments.

From the results in Table 3, among the four sets of experiments, the positioning results obtained from band 2 are the most accurate, followed by band 1, and band 3 is the worst. The results obtained from the positioning to see band 1, after analysis, the distribution in the band 1, the signal and interference signal modulated signal ground vibration, plus the effect of noise, resulting in positioning accuracy is not high. Judging from the positioning results of band 3, the positioning accuracy is very low and the error is large; After analysis, it is believed that due to the large signal attenuation in band 3, when the signal propagates to the sensor, the leakage acoustic signal attenuates greatly, and the noise covers the leakage acoustic signal, resulting in inaccurate final calculation results. From Fig.8, the PSD in band 2 is the largest, indicating that the energy of the leakage signal is the largest in band 2, that is, most of the leakage acoustic signal is in band 2. The calculation result obtained by frequency band 2 is the most accurate, indicating that the information in band 2 contains the most leaked signals. Among the four groups of experiments, the positioning result of the second group is the most accurate, and the positioning result of the third group is the least accurate. In the third set of experiments, the distance difference between the two measuring points and the leaking point is the smallest, the wave speed is very fast, and the resolution of the equipment is not high, the time delay obtained has errors, which leads to the accuracy of the final result. In the second set of experiments, the distance between the two measurement points and the leakage point is very large, which reduces the influence of the error of the time delay on the positioning result.

In engineering application, apply research results to acoustic leak detection engineering. Also, it provides a theoretical basis for future research and technical guidance for engineering practice.

4 Conclusion

In theory, the pipe's dispersion characteristics of axisymmetric waves are derived from the coupling equations of buried liquid-filled pipe. In the field test, the characteristic frequency was obtained with the help of sensors and computers. Wave speed and attenuation under characteristic frequency are solved by wavelet decomposition. Theoretical analysis and test results are in agreement with each other, both showed that the dispersion characteristic of axisymmetric wave exists in the characteristic frequency band of leakage signal. By using the obtained dispersion relation, the acoustic signals with different characteristic frequencies are studied by cross-correlation method, the time delay of the leakage signal is carried out, and the accuracy of leakage location is discussed. The output shows that the accuracy is low when the high-frequency signal is used to leakage location, which attributes to the fast attenuation of the high-frequency signal. The characteristic signal with low amplitude in the low-frequency band is easily affected by the propagation path and is not suitable for leakage location. The vibration signal with high energy in the low-frequency band has higher accuracy for leakage location, and the average error is 9.86%, which meets the engineering requirements.

Acknowledgments: The authors gratefully acknowledge the support of the National Nature Science Foundation of China (No.11774378)

References

[1] Shengyong Mao,Zhicai Ye. China Statistical Yearbook[M]. China Statistics Press,2019;4-5.

[2] Xiaoming Zheng.Current situation of leakage of urban water supply pipe network[J]. Urban and rural construction, 2015;(11):20-21.

[3] China Town Water Supply Association. Urban water supply industry technology development plan in 2010 and long-term goals in 2020[M].China Construction Industry Press,2005;

[4] J M Muggleton, M J Brennan, P W Linford. Axisymmetric wave propagation in fluid-filled pipes: wavenumber measurements in vacuo and buried pipes[J]Journal of Sound and Vibration,2004;270(1-2):171-190.

[5] R J Pinnington, A R Briscoe, Externally applied sensor for axisymmetrical waves in a fluid-filled pipe[J]. Journal of Sound and Vibration,1994; (173):503–516.

[6] Fuller, F J Fahy. Characteristics of wave propagation and energy distributions in cylindrical elastic shells filled with fluid, Journal of Sound and Vibration, 1982; (81): 501-518.

[7] Hunaidi O, Chu W T. Acoustical characteristics of leak signals in plastic water distribution pipes[J] Applied Acoustics, 1999;58(3):235-254.

[8] Li S, Wen Y, Li P, et al. Leak location in gas pipes using cross-time-frequency spectrum of leakage-induced acoustic vibrations[J]. Journal of Sound and Vibration, 2014;333(17): 3889-3903.

[9] Gao Y, Brennan M J, Joseph P F. A comparison of time delay estimators for the detection of leak noise signals in plastic water distribution pipes[J]. Journal of Sound and Vibration, 2006;292(3-5): 552-570.

[10]Hongmei Yan. Characteristic Analysis of Leakage Signal of Underground Water Pipe[D].Changchun: Changchun University of Science and Technology,1999.

[11]Shangshang Ji. Research on Leakage Monitoring System of Water Supply Network[D]. Handan: Hebei University of Engineering, 2018.

[12]Yumei Wen,Ping Li,Jing Yang. Signal correlation function estimation in adaptive time delay estimation value[J] Signal processing,2006(06):774-777.

[13]Yajun Guo, Rongwei Nie, Jinan Zhu et al. Correlation location algorithm for pipe leakage based on 3 sensors[J].Journal of Nanjing University of Science and Technology,2003,27(6):682-685.

[14]Xiaohong Gu, Guangxin Zhang, Dibo Hou, et al. Determining the Leakage Location of Water Pipes by Combining Wavelet Packet Decomposition and Energy Feature Extraction[J]. Journal of Sichuan University,2005,37(6):145-149.

[15] Yan Gao, Yuyou Liu, Yifan Ma, et al. Application of the differentiation process into the correlation-based leak detection in urban pipe networks[J]. Mechanical Systems and Signal Processing. 2018;(112) 251–264.

[16]Jing Yang. Research on Signal Analysis and Processing in Leak Detection and Location of Liquid-filled pipe[D]. Chongqing: Chongqing University,2007.

[17]Jianli Zhang, Kai Tong, Fang Ma. Experimental Research on Pipe Leak Point Location System with Correlation Analysis Method[J]. Journal of Harbin Institute of Technology, 2007; (06):875-878.

Viser Technology Pte. Ltd.
Mechanical Engineering Science
DOI: 10.33142/mes.v3i1.4334

Research Article Open Access

Wheel Profile Optimization of Speed-up Freight Train Based on Multi-population Genetic Algorithm

Yaodong FU, Dabin CUI*, Pengcheng LEI, Xing ZHANG, Jingkang PENG

School of Mechanical Engineering, Southwest Jiaotong University, Chengdu, China

***Corresponding Author:** Dabin CUI, No.111, North 1st Section, 2nd Ring Road, Chengdu City, 610031, China; cdb1645@163.com*

Abstract:
The geometric shape of the wheel tread is mathematically expressed, and geometric parameters affecting the shape of the wheel were extracted as design variables. The vehicle dynamics simulation model was established based on the vehicle suspension parameters and track conditions of the actual operation, and the comprehensive dynamic parameters of the vehicle were taken as the design objectives. The matching performance of the wheel equivalent conicity with the vehicle and track parameters was discussed, and the best equivalent conicity was determined as the constraint condition of the optimization problem; a numerical calculation program is written to solve the optimization model based on a multi-population genetic algorithm. The results show that the algorithm has a fast calculation speed and good convergence. Compared with the LM profile, the two optimized profiles effectively reduce the wheelset acceleration and improve the lateral stability of the bogie and vehicle stability during straight running. Due to the optimized profile increases the equivalent conicity under larger lateral displacement of the wheelset, the lateral wheel-rail force, derailment coefficient, wheel load reduction rate, and wear index are reduced when the train passes through the curve line. This paper provides a feasible way to ensure the speed-up operation of a freight train.

Keywords: *Speed-up freight trains; Wheel profile optimization; Dynamic performance; Equivalent conicity*

1 Introduction

Railway has always been the main supporting my country's economic development. In 2020, our country's railway freight volume will account for 9.9% of the total social freight volume, and both railway freight volume and freight turnover will rank first in the world[1]; the rapid development of the social economy. At the same time, there are higher requirements for the efficiency of railway transportation, and the most effective way to improve the competitiveness of railway transportation is to increase the speed of freight trains on existing lines. At present, some railway bureaus have proposed optimization of the speed of freight trains for some lines. Plan and implement verification. Under the existing conditions, the speed-up of the vehicle will inevitably increase the force between the wheel and the rail, accelerate wheel-rail wear, reduce the dynamics of the train, and even threaten the safe operation of the vehicle [2-4]. It is very effective to optimize the wheel profile to improve the wheel-rail contact characteristics, improve the dynamic performance of the train, reduce wheel-rail wear, and enhance the production capacity and economic benefits of railway transportation.

Up to now, many achievements have been made in the research of wheel profile optimization design. After analyzing the distribution of tangential and normal forces of the contact model and the influence on wear, Wu [5] took the maximum contact stress, overall wear index, and uniform wheel-rail tread wears as the design objective, based on the existing railhead shape Carry out extended profile design. Cui et al.[6-7] established a weighted normal gap method based on vehicle-track coupling dynamics. According to the given vehicle and track parameters, the weight range of the lateral movement is divided according to the probability of the lateral movement to conveniently optimize the tread surface. Shen et al. [8-9] designed the wheel profile based on the contact angle characteristic curve and the inverse algorithm of the railhead shape combined with software development and applied this method to design a variety of wheel profiles. In Shevtsov et al.[10] wheel profile optimization design method based on the rolling circle radius difference curve, the vertical coordinate of the wheel profile is used as the design variable, the optimal rolling circle radius difference curve is used as the control curve, and the numerical solution of the inverse function problem is used to design the new surface. Jahed et al.[11] uses cubic

Received 25 February 2021; Accepted 28 May 2021

splines to connect the curve segments of the wheel profile in the optimization design method based on the difference of the rolling circle radius to ensure the convexity and concavity and monotony of the wheel profile. Five control parameters are used to improve the design efficiency. Liu [12] used numerical simulation as the main method to study the matching relationship between high-speed wheel and rail profiles in my country. Based on the Chebyshev curve fitting method, he proposed a design method for high-order curve wear-shaped treads, and the wheel wear performance was improved. Cheng et al.[13] proposed a multi-objective profile optimization method based on the response surface of the Gaussian radial basis function. The wheel profile arc parameters were used as the design variables, and the critical speed was used as the objective function. The profile wear index after optimization for the specific vehicle model was improved. Low, better dynamic performance.

Most of the wheel profiles obtained by the above research methods are smooth high-order smooth curves, which can make the wheel-rail contact more smooth and the vehicle dynamics performance is better. However, as the wheel wears, the smooth wheel profile is quickly ground. Roughly, the dynamic performance decreases, and it is difficult to process the wheel profile with discrete high-order curves in actual engineering. This paper takes the wheel profile of freight trains as the research object, establishes the vehicle system dynamics model, and finds the optimal equivalent conicity of the simulated vehicle. The geometric relationship of the wheel tread profile curve is derived, the tread arc parameter is used as the design variable, the dynamic performance of the vehicle is used as the objective function, and the optimal mathematical model of the wheel profile is established, and the model is solved by the multi-population genetic algorithm. The optimized profile was compared and verified with the actual LM profile.

2 Optimal mathematical model

2.1 Design variables

Most standard wheel profiles are arc-shaped wheel profiles, with a definite analytical relationship in geometric expression, and controllable uniformity of wheel-rail contact. By changing the arc parameters of the wheel profile to optimize the wheel profile in engineering applications feasible. Fig.1 shows the geometric expression of the standard wear-type wheel tread. First, the main area in contact with the rail when the vehicle is running determines the optimal area to be 4 arcs between A and E; point A is in phase with the 70° line of the flange tangent, point E is tangent to a straight line segment with a slope of 1:8, B, C, and D are the tangent points of 4 arcs in pairs, O_1~O_4 is the center of each arc, R_1 ~R_4 is the radius of each arc, Z_1 and Z_2 are the contact points with the rail when the wheelset is moved 3mm left and right; Using the wheel-rail geometric contact calculation program of the research group, the coordinates x_{Z1}, y_{Z1}, x_{Z2}, y_{Z2} of Z_1 and Z_2 are obtained from the conical tread surface with the best equivalent conicity of the simulated vehicle. Taking these two points as the fixed points of the optimized profile can make the equivalent conicity of the optimized profile better approximate the best equivalent conicity. Because the tread is in contact with the CN60 rail, R_1 mainly provides the rolling radius difference for the curve with a too-small radius. Keep the fixed value of R_1 unchanged at 14mm. R_4 has less contact with the rail during normal driving and keeps its fixed value unchanged at 220mm, x_D defaults. The distribution intervals of Z_1 and Z_2 points on different wheel profiles are different. For example, LM profiles Z1 and Z2 are distributed in the BC and CD zones respectively, and the LM_A and other profiles are distributed in the CD zone. Therefore, the two cases will be discussed and deduced separately the geometric relationship of the arc parameters in the tread profile in the two cases.

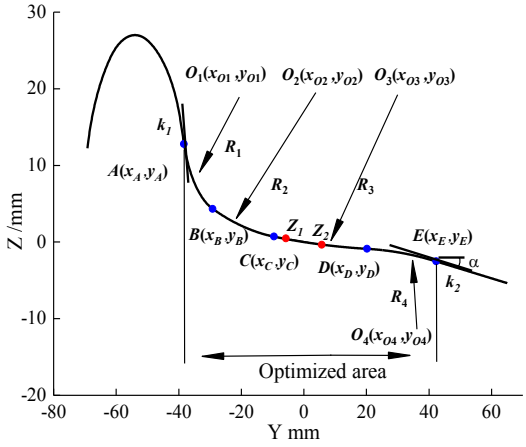

Fig.1 Geometric expression of wheel profile

2.1.1 When Z1 and Z2 are distributed on the arc CD:

If the AB segment is tangent to the -70° straight line segment, its center can be calculated as:

$$\begin{cases} b=y-x\cdot tan(-70^\circ) \\ y_{O1}=tan(-70^\circ)\cdot x_{O1}+b+14\sqrt{1+(tan(-70^\circ))^2} \end{cases} \quad (1)$$

In the formula, y and x are the coordinates of any point on the -70° straight line segment on the wheel flange, and b is the equation constant.

The tangent point A of the arc AB and the -70° straight line segment can be obtained by the following formula:

$$\begin{cases} k_{01}=(-1)/(tan(-70^\circ)) \\ b_{01}=-k_{01}x_{O1}+y_{O1} \\ y_A=tan(-70^\circ)x_A+b \\ y_A=k_{01}x_A+b_{01} \end{cases} \quad (2)$$

In the formula, k_{01}, b_{01} are the slope of the vertical line of the -70° straight line passing the center of the arc AB and the equation constant.

If the arc CD passes through points Z_1 and Z_2, the center O_3 can be calculated by the following formula:

$$\begin{cases} R_3^{\,2} = (x_{O3} - x_{Z1})^2 + (y_{O3} - y_{Z1})^2 \\ R_3^{\,2} = (x_{O3} - x_{Z2})^2 + (y_{O3} - y_{Z2})^2 \end{cases} \quad (3)$$

The arc *BC* is tangent to the arc *AB* and *CD*, and its center O_2can be calculated by the following formula:

$$(x_{O2} - x_{O1})^2 - (y_{O2} - y_{O1})^2 - (R_3 - R_2)^2 + (x_{O3} - x_{O2})^2 + (y_{O3} - y_{O2})^2 = 0 \quad (4)$$

The tangent point of the arc AB and BC is at the intersection of the straight line O_1O_2 and the arc. Point B can be obtained by the following formula:

$$\begin{cases} k_{12} = (y_{O2} - y_{O1}) / (x_{O2} - x_{O1}) \\ b_{12} = -k_{12} x_{O1} + y_{O1} \\ y_{O1} = y_B + \sqrt{R_1^{\,2} - (x_{O2} - x_B)^2} \\ y_B = k_{12} x_B + b_{12} \end{cases} \quad (5)$$

In the formula, k_{12} and b_{12} are the slopes of the straight line O_1O_2 and the equation constant.

The tangent point of the arc BC and CD is at the intersection of the straight line $O_2O_3$and the arc. Point C can be obtained by the following formula:

$$\begin{cases} k_{23} = (y_{O3} - y_{O2}) / (x_{O3} - x_{O2}) \\ b_{23} = -k_{23} x_{O2} + y_{O2} \\ y_{O2} = y_C + \sqrt{R_2^{\,2} - (x_{O2} - x_C)^2} \\ y_C = k_{23} x_C + b_{23} \end{cases} \quad (6)$$

In the formula, k_{23} and b_{23} are the slopes of the straight line O_2O_3 and the equation constant.

The arc CD and DE are tangent at point D, and y_D can be obtained from the following formula:

$$y_D = y_{O3} - \sqrt{R_3^{\,2} - (x_{O3} - x_D)^2} \quad (7)$$

k_{34} is the slope of the straight line O_3O_4 can be obtained by the following formula:

$$k_{34} = (y_{O3} - y_D) / (x_{O3} - x_D) \quad (8)$$

β is the angle between the straight line O_4 and the horizontal line, β can be calculated by k_{34}, and the center O_4 of the arc *DE* can be obtained by the following formula:

$$\begin{cases} \beta = arctan(|\, k_{34} \,|) \\ x_{O4} = x_D - R_4 \cos\beta \\ y_{O4} = y_D - R_4 \sin\beta \end{cases} \quad (9)$$

The arc and the straight line segment with slope k_2 intersect at point E, which can be obtained by the following formula:

$$\begin{cases} \alpha = arctan(|\, k_2 \,|) \\ x_E = x_4 + R_4 \sin\alpha \\ y_E = y_4 + R_4 \cos\alpha \end{cases} \quad (10)$$

At this point, each arc parameter in the optimized area of the wheel profile can be expressed by the arc radius R_2, R_3, and the abscissa x_{o1} of the arc AB's center. These three unknowns are used as the optimization variables of the model:

$$\boldsymbol{v} = [R_2, R_3, x_{O1}] \quad (11)$$

The 4 tangent arcs can be expressed as:

$$C_i = f_i(\boldsymbol{v}) \quad (12)$$

In the formula, $f_i(i = 1,2,3,4)$is the analytical equation of each arc.

Given the four-segment arc equation, the profile curve of the optimized wheel area can be expressed as:

$$C_{\text{wheel}} = f_w(\boldsymbol{v}) \quad (13)$$

In the formula, f_w is the analytical equation of the optimized area profile curve.

2.1.2 When Z1 and Z2 are respectively distributed on the arcs BC and CD:

The arc *CD* passes *C*, Z_2 points, then the circle center O_3 can be calculated by the following formula:

$$\begin{cases} R_3^{\,2} = (x_{O3} - x_C)^2 + (y_{O3} - y_C)^2 \\ R_3^{\,2} = (x_{O3} - x_{Z2})^2 + (y_{O3} - y_{Z2})^2 \end{cases} \quad (14)$$

The arc *BC* passes through Z_1, the point *C* is tangent to the arc *CD*, and its center O_2, R_2 can be calculated by the following formula:

$$\begin{cases} k_{23} = (y_{O3} - y_C) / (x_{O3} - x_C) \\ b_{23} = -k_{23} x_{O3} + y_{O3} \\ k_{22} = -1 / ((y_C - y_{Z1}) / (x_C - x_{Z1})) \\ b_{22} = -k_{22} x_{BB} + y_{BB} \\ y_{O2} = x_{O2} \cdot k_{23} + b_{23} \\ y_{O2} = x_{O2} \cdot k_{22} + b_{22} \\ R_2^{\,2} = (x_{O2} - x_C)^2 + (y_{O2} - y_C)^2 \end{cases} \quad (15)$$

In the formula, k_{23} and b_{23} are the slopes of the straight line O_3C and the equation constants, x_{BB} and y_{BB} are the coordinates of the midpoint of the chord of the arc Z_1C, k_{22} and b_{22} are the slope of the vertical line of the chord of the arc Z_1C, and the equation constants.

The arc of segment *AB* is tangent to the -70° straight line segment, and at the same time tangent to the arc of segment *BC*, its center O_1 can be calculated as:

$$\begin{cases} b = y - x \cdot tan(-70^\circ) \\ y_{O1} = tan(-70^\circ) \cdot x_{O1} + b + 14\sqrt{1 + (tan(-70^\circ))^2} \\ (R_2 - 14)^2 = (x_{O2} - x_{O1})^2 + (y_{O2} - y_{O1})^2 \end{cases} \quad (16)$$

In the formula, y and x are the coordinates of any point on the -70° straight line segment on the wheel flange, and b is the equation constant.

The geometric derivation formulas of the remaining arc parameters and the first distribution will not be repeated. At this point, each arc parameter in the wheel profile optimization area can be expressed by the arc radius R_3 and the coordinate of point C, x_C, y_C These three unknowns are used as the optimization variables of the model:

$$\boldsymbol{v} = [R_3, x_C, y_C] \quad (17)$$

The 4 tangent arcs can be expressed as:

$$C_i = f_i(\boldsymbol{v}) \quad (18)$$

In the formula, $f_i(i = 1,2,3,4)$ is the analytical

equation of each arc.

Then the profile curve of the optimized wheel area can be expressed as:

$$C_{\text{wheel}} = f_w(\boldsymbol{v}) \tag{19}$$

In the formula, f_w is the analytical equation for optimizing the area profile curve.

2.2 Objective function

Taking the comprehensive dynamic performance index of freight trains as the objective of surface optimization design, the vehicles run at speed on existing lines, and the track irregularity of my country's mainline railway is between the fifth and sixth class railways in the United States [15]. Setting the American five-level spectrum as the line irregularity incentive. Although the straight-line accounts for a higher proportion of the total line length, refer to the actual operation situation. Because the dynamic performance of the vehicle rarely exceeds the standard when the vehicle is running in a straight line, the exceeding often occurs in the curve operation, so the simulation condition is set as: the length of the straight line is 600 m, the sampling frequency is 200 Hz, and the speed is 90km/h. The curve selects the smallest radius curve that allows vehicles to pass 90km/h. The line parameters are shown in Table 1.

Table 1. Simulation parameters of small radius curve

Serial number	parameter name	Numerical value
1	Straight length	600m
2	Easing curve length	100m
3	Curve radius	R800m
4	Circular curve length	500m
5	Super high line	100mm
6	Sampling frequency	200Hz
7	Running speed	90km/h

Since the derailment coefficient, wheel load reduction rate, and other indicators are not exceeded during straight-line running, the main concern is the straight-line running stability of the vehicle. Therefore, the RMS value of the lateral acceleration of the wheelset and the body stability is selected to measure the straight-line running performance. When the curve is running, more attention is paid to the running stability of the vehicle, so the derailment coefficient, wheel load reduction rate, and wheel axle lateral force when the train passes a small radius curve is selected to measure the curve passing performance of the train, and the objective function is established as formula (20):

$$\min \begin{cases} f_1(\boldsymbol{v}) = \max(s\ddot{y}) \\ f_2(\boldsymbol{v}) = W \\ f_3(\boldsymbol{v}) = \max(|(Q_l / P_l)|, |(Q_r / P_r)|) \\ f_4(\boldsymbol{v}) = \max(\Delta P / P) \\ f_5(\boldsymbol{v}) = \max(|Q_r - Q_l|) \end{cases} \tag{20}$$

In the formula, f_1 represents the maximum value of the RMS lateral acceleration of the left and right wheelsets during straight running, f_2 represents the train stability index during straight running, f_3 represents the maximum derailment coefficient of the left and right wheels during curve running, and f_4 represents wheel weight reduction during curve running. The maximum load factor, f_5 represents the maximum lateral force of the wheel axle when the curve is running.

Based on the importance of the five objective values and their actual operating performance, it is hoped that both the curve and straight-line performance will be improved. This example sets weighting coefficients respectively for them, among which w_1=0.25, w_2=0.15, w_3=0.2, w_4=0.2, w_5=0.2. At the same time, f_1 to f_5 are normalized with the limit of each kinetic index. The optimization objective function can be expressed as:

$$min\ f\ (\boldsymbol{v}) = w_1 \frac{f_1}{5} + w_2 \frac{f_2}{3.5} + w_3 f_3 + w_4 \frac{f_4}{0.65} + w_5 \frac{f_5}{35} \tag{21}$$

2.3 Constraint equation

The arctangent point should satisfy the following relationship in the optimization area:

$$g_1 = x_E < x_D < x_C < x_B < x_A \tag{22}$$

Considering to ensure that the wheel profile is well matched with the CN60 rail, the wheel profile R_2 and R_3 should meet the following conditions:

$$g_2 = \begin{cases} 85 \le R_2 \le 140 \\ 400 \le R_3 \le 700 \end{cases} \tag{23}$$

When the points Z_1 and Z_2 are distributed on two arcs, the wheel profile R_2 and R_3 should meet the following conditions:

$$g_2 = \begin{cases} y_C < k_z \cdot x_C + b_z \\ 85 \le R_2 \le 140 \\ 400 \le R_3 \le 700 \end{cases} \tag{24}$$

Where k_z and b_z are the slopes of the straight line Z_1Z_2 and the equation constant respectively.

At the same time, to ensure that the equivalent conicity of the optimized profile should meet the best equivalent conicity of the simulated vehicle as much as possible, the equivalent conicity of the optimized profile should meet the following conditions:

$$g_3 = \lambda_{min} < \lambda_e < \lambda_{max} \tag{25}$$

In the formula, λ_e R is the equivalent conicity when the wheelset is laterally moved by 3mm and λ_{min} λ_{max} is determined by the best equivalent conicity of the simulated vehicle.

From equation (20) ~ equation (25), the optimal mathematical model can be expressed as:

$$\begin{cases} f\ (\boldsymbol{v}) \to \min \\ st: g_1, g_2, g_3 \end{cases} \tag{26}$$

3 The optimal equivalent conicity

Based on the measured vehicle parameters of a certain

type of freight train on the East Longhai Line (the main performance parameters are shown in Table 2), CN60 rails are used, the gauge is 1435 mm, the inner distance of the wheelset is 1353 mm, the rail cant is 1/40, and the multi rigid body dynamics software [16-17] establishes the dynamics model of the vehicle system. Fig.2 shows the topology of the vehicle structure.

Table 2 Main vehicle parameters

Serial number	parameter name	Numerical value
1	Vehicle body mass	17500kg
2	Side frame quality	373.5kg
3	Wheelset quality	1154kg
4	Bolt quality	373.5kg
5	Vehicle distance	11.7m
6	Suspension span	1.956m
7	Crossbar stiffness	14.8MN/m
8	Wheelbase	1.75m
9	Wheel radius	0.42m

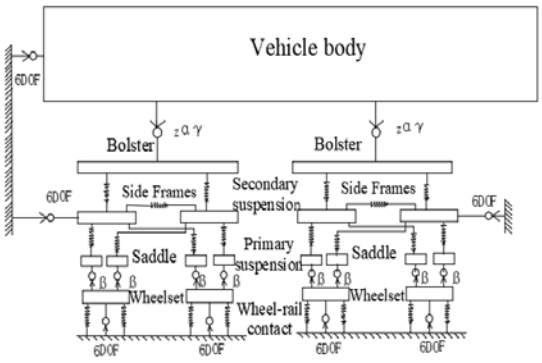

Fig.2 Topological diagram of the vehicle structure

Due to the unevenness of the track, the wheel-rail rolling contact process will form a rolling radius difference that leads to hunting motion [18]. The equivalent conicity can be obtained through a certain algorithm from the rolling circle radius difference. The equivalent conicity of the wheelset is commonly used in engineering to explain its relationship with vehicle dynamics. The straight-line section accounts for more than 80% of freight trains in speed-up operation. The critical speed of train snaking instability is the main evaluation index to measure the stability of the train system's straight-line operation. Based on the definition of equivalent conicity [19], the nominal equivalent conicity (The wheelset lateral displacement 3mm) and the hunting critical speed of the vehicle are studied. The Conical tread is equivalent to the linearization of the main tread, which can ensure that the equivalent conicity varies within a certain range and the equivalent conicity does not change. Based on the shape of the conical tread of TB449-1976 locomotive wheels [20], 13 conical treads with different equivalent conicity between 0.032-0.16 are designed. Fig. 3 only shows the equivalent conicity of the tread with equivalent t conicity of 0.032, 0.05, 0.107, and 0.16.

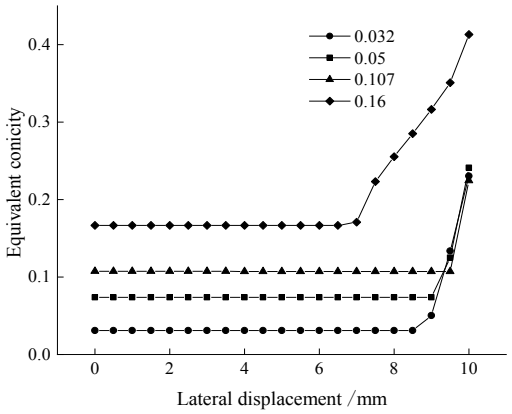

Fig.3 The equivalent conicity of different Conical treads

Using the following method to calculate the critical hunting speed of a freight train can be described as First, let the vehicle pass through an 800m long line with excitation at a certain speed. If the train derails, the speed is higher than the critical speed of the vehicle. Reduce the speed and continue driving. When the vehicle is not derailed, set the vehicle to the same speed at the ideal level. When driving on a straight track, if the wheelset of the vehicle oscillates with a constant amplitude at this time, this speed is defined as the non-linear critical speed of the vehicle. The critical speeds of different treads obtained by simulation calculation using the above-mentioned vehicle model are shown in Fig.4. As the equivalent conicity increases, the critical speed of the vehicle reaches the maximum and then decreases, which is similar to the critical hunting speed distribution proposed by Polach [21]. It is different from the traditional belief that the larger the equivalent conicity, the smaller the critical speed. This is because it is related to vehicle suspension parameters [22], When the equivalent conicity is small, the gravity suspension stiffness of the vehicle will be small, and when the wheelset deviates from a certain distance due to certain excitation, the wheels cannot provide enough guiding force to keep the wheels running along the centerline of the track. Therefore, the optimal tread equivalent conicity of this model should be designed at about 0.107.

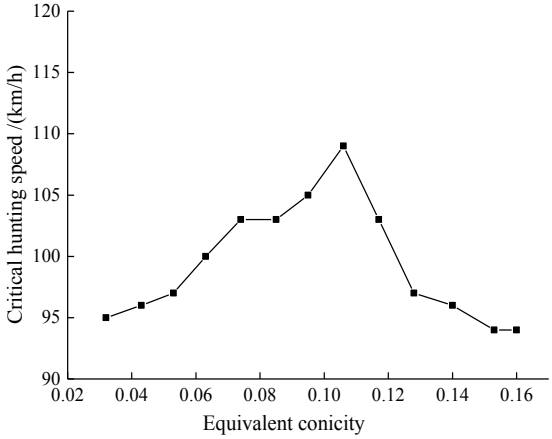

Fig.4 Critical hunting speed of different conical treads

4 Optimization method

4.1 Multi-population genetic algorithm

Multi-population genetic algorithm [23-24] is improved based on genetic algorithm, which solves the premature problem of traditional genetic algorithm. The optimization of traditional genetic algorithms is mainly reflected in the following aspects:

(1) Simultaneous optimization of multiple populations, different populations are given different control parameters to achieve different search purposes.

(2) Coordinated evolution between populations is realized through the connection of migration operators.

(3) Manually select the operator to save the optimal solution of various groups to determine the convergence of the algorithm.

The main content of the multi-population genetic algorithm is: the solution data of the solution space is expressed as the genotype string data of the genetic space through coding, and the string structure data of different combinations constitute different individuals;

Randomly generate an initial population composed of N populations. Each population contains P initial individuals. Start the evolution with the initial population as the starting point. Perform fitness evaluation on each individual and select the outstanding individuals as the parent to breed the next generation of offspring. Through the crossover operation, the new individual can inherit the characteristics of the parent individual, and at the same time, a few individuals are randomly selected to perform mutation operations to change their genes, and the populations are migrated to find the worst individuals of the target population to replace them with the best individuals of the source population, and repeat the evolution finally gets the optimal individual. The main control parameters of the multi-population genetic algorithm include population number (N), population size (P), binary digits of variables (Pr), individual length (D), optimal individual minimum retention algebra (MG), generation gap ($GGAP$), Crossover probability (Pc) and mutation probability (Pm). Among them, N and P represent the abundance of population information, which affects the calculation amount of the algorithm and the optimization speed of the optimization problem; Pr controls the accuracy of the variable; D represents the length of each vector in the population, which is determined by the number of variables; MG affects the optimal solution $GGAP$ determines the ratio of parent generation to be replaced; Pc controls the degree of information exchange between parent and offspring, affecting population diversity and the global search ability of the algorithm, Pm represents the probability of an individual's gene mutation, which affects The local search capability of the algorithm.

4.2 Wheel profile optimization

Before the algorithm starts, set the control parameters in the algorithm, and express the wheel profile variables in the optimization model in the form of population individuals:

$$\boldsymbol{v} \rightarrow \boldsymbol{x} = (d_1, d_2 \cdots d_D) \tag{27}$$

In the formula, $\boldsymbol{x}$ represents the individual vector in the population, and d represents the variables in respectively.

Then the population can be expressed as:

$$\boldsymbol{X} = \begin{cases} [\boldsymbol{x}_{11}; \boldsymbol{x}_{12}; \cdots; \boldsymbol{x}_{1P}] \\ [\boldsymbol{x}_{21}; \boldsymbol{x}_{22}; \cdots; \boldsymbol{x}_{2P}] \\ . \\ . \\ [\boldsymbol{x}_{N1}; \boldsymbol{x}_{N2}; \cdots; \boldsymbol{x}_{NP}] \end{cases} \tag{28}$$

In the formula, $\boldsymbol{X}$ represents the initial population composed of N populations, and each population is composed of P individual vectors.

The specific process is shown in Fig.5: Input the vehicle parameters and track parameters into the vehicle model, and calculate the best equivalent conicity; The initial population $\boldsymbol{X}$ is randomly generated in the constraint space. Each individual in the population corresponds to a wheel profile. The equivalent conicity of each profile is calculated. The individuals that do not meet the equivalent conicity constraints are marked as inferior individuals and their fitness is set as low. The rest of the profiles are imported into the multi-body dynamics software for simulation and the objective function value $f(\boldsymbol{v})$ is calculated, and the optimal profile is selected. When the optimal profile retention algebra is less than the set retention algebra, the fitness $Fv(i)$ of various groups is calculated, and a new population $\boldsymbol{U}$ is obtained by operations such as selection, crossover, mutation, reinsertion, and immigration based on the fitness. Continue to evolve until the optimal profile meets the minimum maintenance algebra, and the optimal wheel profile can be obtained by obtaining the optimization result. The entire solution process is carried out in a closed loop.

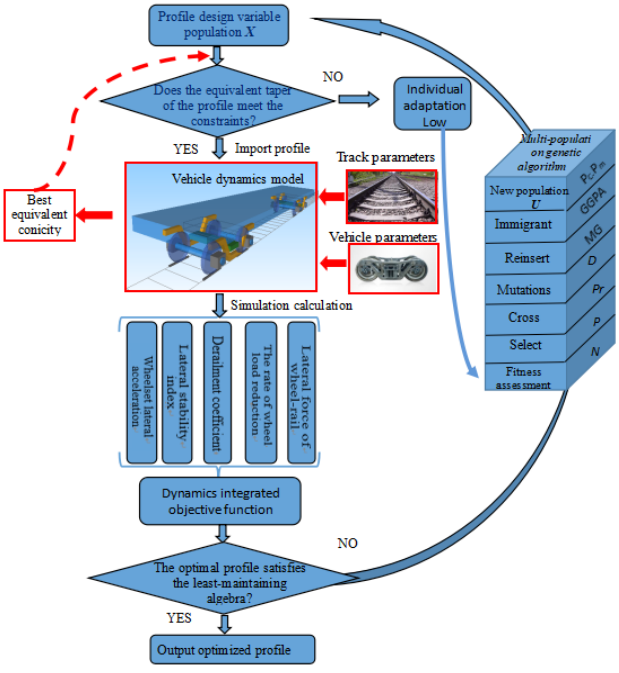

Fig.5 Flow chart of profile optimization

5 Results and analysis

5.1 Optimization Results

By programming and calculating the process shown in Fig.5, the relevant control parameters (Table 3) of a variety of genetic algorithms are selected to design the wheel profile. For the two situations where the wheelset lateral displacement is 3mm contact point pair distribution, The range of design variables is shown in Table 4、Table 5.

Table 3 Calculation parameters

Serial number	parameter name	Numerical value
1	N	5
2	P	20
3	Pr	20
4	D	3
5	MG	20
6	$GGAP$	0.9
7	P_c	(0.7-0.9)
8	P_m	(0.001~0.05)

Table 4 Design variables value

Serial number	parameter name	Numerical value
1	R_2	(85~140)
2	R_3	(400~700)
3	x_{o1}	(-25.1~-25.9)

Table 5 Design variables value

Serial number	parameter name	Numerical value
1	R_3	400~700)
2	x_C	(-8~-10.5)
3	y_C	(0.757~1)

Fig.6 shows the evolution curve of the optimization process of the two optimization profiles. It can be seen that when the number of evolutions reaches 47 and 53, the objective function has achieved the objective optimum respectively. When the optimal solution remains for 20 generations, the algorithm stops. The two optimized profiles stopped after the 66th and 74th generations respectively, which proved that the method has a better convergence speed and obtains the ideal wheel profile faster.

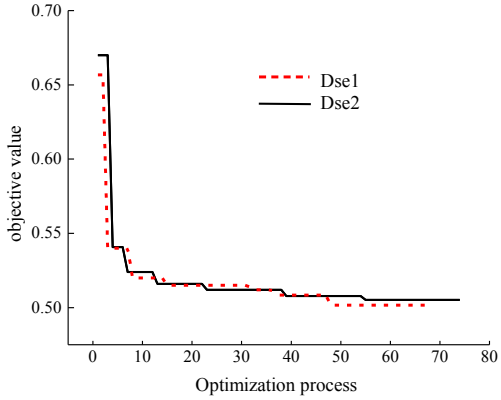

Fig.6 Des1, Des2 optimization process

5.2 Wheel-rail contact state

Fig.7 shows the LM profile and the optimized profile Des1 (the contact point of the wheelset traverses 3mm on the arc CD) and the optimized profile Des2 (the wheelset traverses the 3mm contact point on the arc BC and CD Top) Distribution map of contact point pairs with CN60 rail. It can be seen that when the Des1 profile and Des2 profile have a lateral displacement of 3mm from the left and right of the wheelset, their contact points are more concentrated on the wheel. The width of the distribution range is respectively: LM is 8.83mm, Des1 is 7.1mm, and Des2 is 8.5mm. When the two optimized profiles are running in a straight line, the change range of the contact position of the wheel tread is smaller, and the vehicle will travel more smoothly. When the wheelset lateral displacement is large, the matching characteristics at the flange of the wheel remain unchanged due to the same parameters of the wheels.

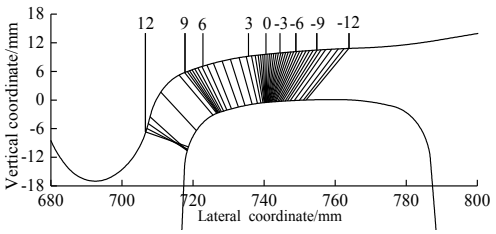

Fig.7(a) LM wheel-rail contact geometry

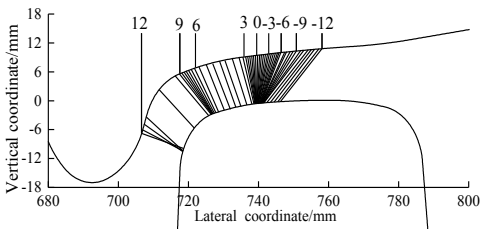

Fig.7(b) Des1 wheel-rail contact geometry

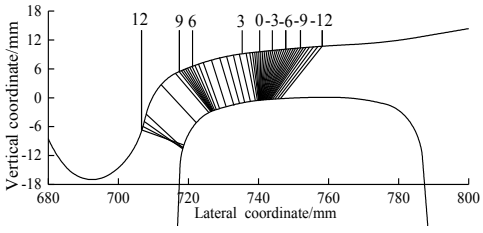

Fig.7(c) Des2 wheel-rail contact geometry

Fig.8 shows the equivalent conicity of Des1, Des2, and LM profiles. The average equivalent conicity of the three profiles at 3mm before the lateral shift of the wheelset are 0.1075, 0.104, and 0.102 respectively. The optimized profile Des1 and Des2 is closer to the optimal equivalent conicity of 0.107 for the simulated vehicle obtained in Chapter 1 and is more suitable for the simulated vehicle. It can also be seen that the equivalent conicity of the Des1 profile is slightly larger than LM when the amount of lateral movement is 6-9mm, and the equivalent conicity of the Des2 profile is significantly greater than LM. A larger equivalent conicity helps to improve the curve passing performance of the train and it can better exert the creep guiding ability between the wheel and rail.

Fig.9 shows the comparison of the rolling radius difference within 10mm of the wheelset lateral movement. It can be seen that the optimized profile increases the rolling radius difference within the range of 5-9.5mm for the wheelset lateral movement. It can be found that it is similar to the equivalent conicity. Conclusion The increase of rolling radius difference helps to improve the curve passing performance of the train and can better exert the sliding guiding ability between the wheel and the rail.

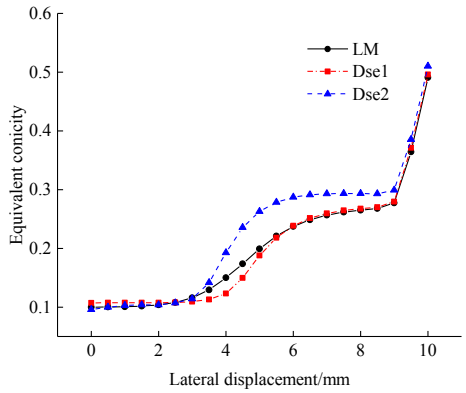

Fig.8 Comparison of equivalent conicity

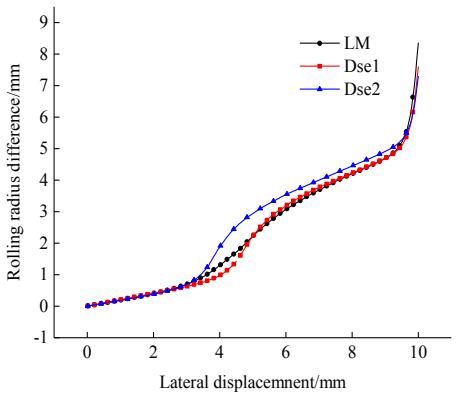

Fig.9 Comparison of rolling radius difference

5.3 Dynamic behavior on the tangent line

Use the critical hunting speed calculation method in Chapter 3 to calculate the hunting critical velocities of the three types of surfaces. The critical hunting speed of Des1, Des2, and LM profiles are 142km/h, 140km/h, and 135km/h respectively. After investigation, the bogie structure speed of this type of freight train is 120 km/h. The optimized profile is to a certain extent, the critical speed of serpentine instability of the train is increased, and all of them meet the operating requirements of 90km/h.

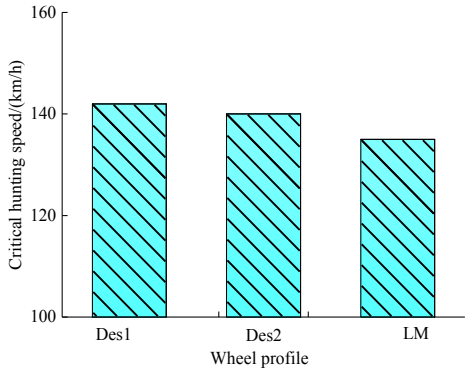

Fig.10 Critical hunting speed of three types of tread

Carry out linear running simulation calculation, set the American pentad spectrum as the line irregularity excitation, set the length of the linear line to 600 m, the sampling frequency of 200 Hz, and the passing speed of 90 km/h. Wheelset lateral vibration acceleration is an important evaluation index for train stability. UIC518 stipulates the criterion for determining the root mean square value of wheelset lateral acceleration as: $s\ddot{y}\big|_{\lim} = 5(m/s^2)$, and the $\ddot{y}$ calculation formula for acceleration root mean square is:

$$\ddot{y} = (\ddot{y}_1^{\,2} + \ddot{y}_2^{\,2} + \cdots + \ddot{y}_n^{\,2})^{0.5} \tag{29}$$

In the formula: $\ddot{y}_1, \ddot{y}_2, \cdots \ddot{y}_n$ is the lateral vibration acceleration value of the wheelset at each sampling point in the test section, and $\ddot{y}$ is the root mean square value of the lateral vibration acceleration of the wheelset in the sampling section.

According to the above formula, the root-mean-square values of the lateral vibration acceleration of the wheelset under the working condition of 90km/h are calculated as shown in Fig. 11. Among them, the maximum root means square of the LM profile is 2.96m/s^2, and the maximum root means square of the Des1 profile is 2.40m/s^2, and the maximum value of the Des2 profile is 2.42m/s^2. Two optimized types Compared with the LM profile, the maximum RMS value of the lateral vibration acceleration of the face wheel pair is reduced by 18% and 17% respectively.

According to GB/T 5599-2019 [25], the lateral stability evaluation index of freight car bogies, the obtained lateral vibration acceleration data of the side frame is subjected to 0.5~10 Hz band-pass filtering, and the result is shown in Fig.12; Evaluate whether the filtered bogie lateral vibration acceleration waveform exceeds 8 m/s^2 for 6 consecutive times, and the lateral acceleration value of the side frame when the three profiles are 90km/h running in a straight line does not exceed 8m/s^2, Des1, Des2 profiles Compared with LM, the maximum acceleration value is reduced by 10% and 8% to meet the requirements of safe operation.

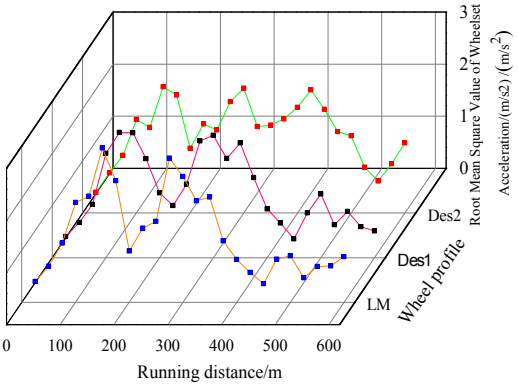

Fig.11 RMS value of lateral acceleration

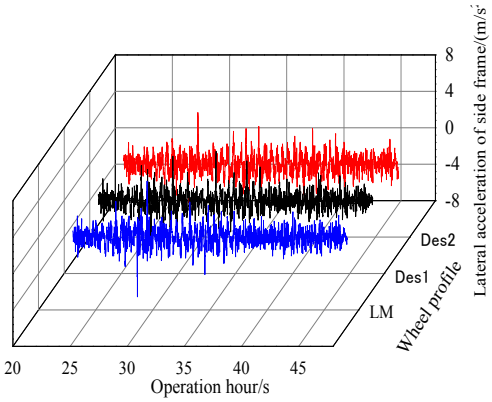

Fig.12 Lateral acceleration of bogie

The train stability index specified in my country GB/T 5599-2019 is used to evaluate the vehicle stability. The formula is:

$$W=3.57\sqrt[10]{A^3F(f)/f} \tag{30}$$

In the formula: W is the stability index, A is the lateral vibration acceleration of the vehicle body (m/s^2), f is the vibration frequency, and $F(f)$ is the weighting coefficient related to the vibration frequency f.

When calculating the vehicle stability index, first perform FFT transformation on the vehicle system acceleration response (time-domain) to obtain the acceleration frequency response function, and then calculate the respective stability index of each frequency band, and finally obtain the total frequency of the whole frequency band by formula (31) stationarity index:

$$W_{tot}=(W_1^{10}+W_2^{10}+\cdots W_n^{10})^{0.1} \tag{31}$$

The stationarity index values of the three types of surfaces are shown in Fig.13. The stationarity indicators of the three types of surfaces are 1.27, 1.19, and 1.25, respectively.

This is because the lateral vibration acceleration of the three types of wheels is not much different when running in a straight line. When the vibration is transmitted from the wheelset to the vehicle body, it is buffered and damped, and when it is transmitted to the vehicle body, the difference is further reduced.

The smoothness index of the three shapes is not higher than 3.5, and the running quality of the freight train that meets the requirements of GB/T 5599-2019 is excellent.

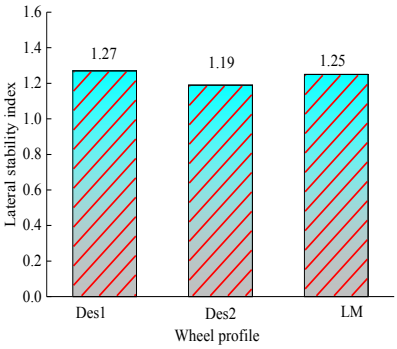

Fig.13 Lateral stability index

5.4 Curving passing performance

The American five-level spectrum is applied as the line random irregularity excitation, and the simulation parameters shown in Table 2 are used to verify the passing performance of the training curve. Process the obtained data following the data processing methods for operational stability and operational quality specified in GB/T5599-2019. Fig.14 shows the lateral force of the axle when the train passes through the R800 curve at 90km/h. The lateral forces of Des1 and Des2 are reduced compared with the LM profile. The maximum values of the lateral forces are 17% and 16% respectively. Because the two optimized profiles have a larger rolling radius difference under the same wheelset lateral displacement, the wheel-rail lateral force is reduced when crossing the curve and the derailment coefficient of the vehicle is reduced. The maximum value of the Des1 profile derailment coefficient is approximately lower than that of LM. 7%, the maximum derailment coefficient of the Des2 profile is 8% lower than that of the LM profile (Fig. 15).

The wheel load reduction rate is used to evaluate whether the train will overturn due to one wheel load reduction during train operation. The safety limit specified in GB/T5599-2019 is $(\Delta P/P)\le 0.65$, ΔP is the wheel load reduction, and P is the average net wheel weight of the axle. Fig.16 shows the schematic diagram of the wheel load reduction rate when the vehicle is assembled with three profiles at 90km/h and passes through the curve. From the Fig., it can be seen that the wheel load reduction rates of the three profiles have similar changes. The wheel load reduction rate is on the curve. The maximum difference of the maximum rate is 3%, and the maximum wheel load reduction rate of the three types of profiles is less than 0.65 when passing through the curve, which is in line with the safe operation regulations.

The lateral acceleration of the bogie when the train passes through the curve at 90 km/h is subjected to 0.5~10 Hz band-pass filtering. The lateral acceleration of the bogie is shown in Fig. 17. The lateral acceleration of the three types of profiles changes almost the same during operation. None of the bogies was unstable.

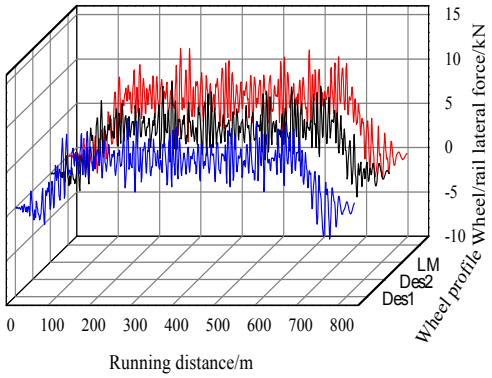

Fig.14 Lateral force of wheel-rail

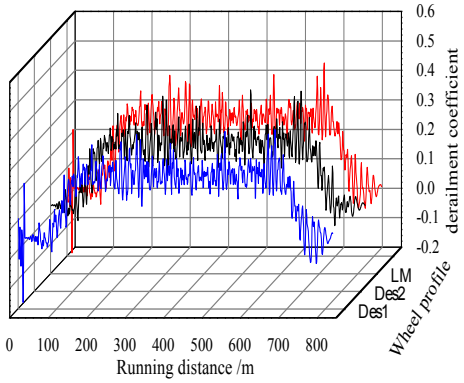

Fig.15 Derailment coefficient

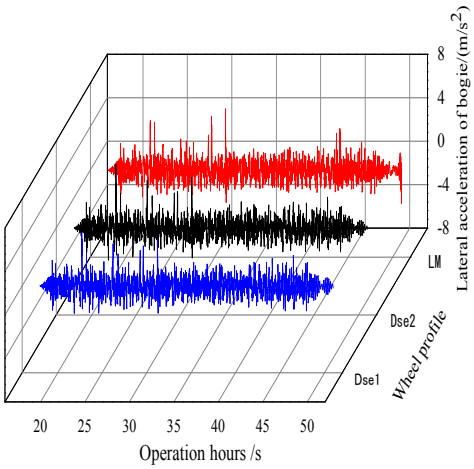

Fig.16 Rate of wheel load reduction

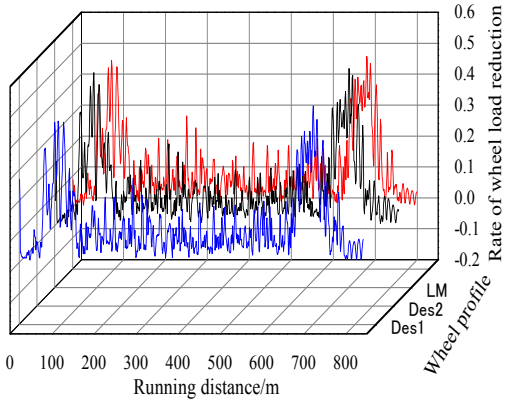

Fig.17 Lateral acceleration of bogie

The wear index is used to evaluate the wear performance of the wheel and rail, and its calculation formula is as follows:

$$We = F_x\xi_x + F_y\xi_y \tag{32}$$

In the formula, We is the wear index of the wheel and the rail at a certain time, F_x and F_y are the longitudinal and lateral creep forces of the wheel and the rail respectively; ξ_x and ξ_y are the longitudinal and lateral creep rates of the wheel and the rail respectively.

The wheel-rail wear index of the three types of profiles passing through the curve at 90km/h is shown in Fig.19. Compared with the LM profile, the average wear index of the Des1 profile and Des2 profile on the curve decreases by 5% and 2%. After the profile optimization, the dynamic performance of the training curve is improved, the creep state of the train is improved, and the wear index of the left and right wheel and rail is reduced.

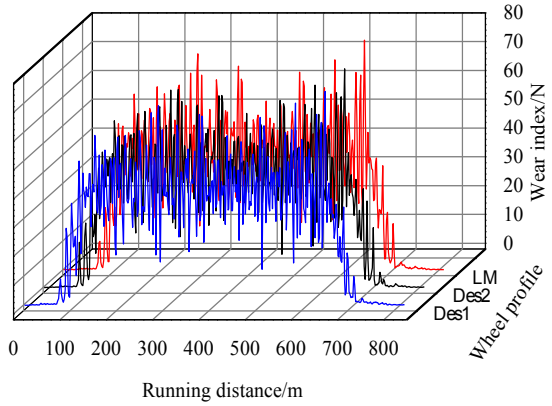

Fig.19 Wear index

6 Conclusion

The vehicle dynamics model was established based on the actual parameters and track conditions of the operating actual vehicles, and the matching performance of the equivalent conicity with the vehicle and track was analyzed, and the optimal equivalent conicity of the simulated vehicle was determined to be 0.107. The wheel profile curve is geometrically deduced, the arc parameters of the wheel profile are used as design variables, and the comprehensive objective function of the train dynamics performance index is used to establish the optimal design model of the wheel profile.

The wheel-rail contact characteristics of the optimized profile are analyzed, and the equivalent conicity of the

optimized profile is closer to the best equivalent conicity of the simulated vehicle, which ensures serpentine stability during straight-line running. Between the 6-9mm wheelset lateral displacement, the equivalent conicity and wheel diameter difference of the two optimized profiles are larger than that of the LM profile, which enables the vehicle to have a larger rolling radius difference when running in a curve, and improves the curve passing performance. Comparing and analyzing the dynamic performance of the two optimized profiles and the LM profile, it is found that when running in a straight line: the RMS value of the wheelset acceleration of the two optimized profiles is effectively reduced, the nonlinear critical speed is slightly increased, and the bogie is laterally stable. The performance and vehicle stability indicators have been improved. When the curve is running, the wheel-rail lateral force is significantly reduced, the derailment coefficient, wheel load reduction rate and wear index are reduced, and the vehicle dynamics of the optimized profile are improved to meet the speed-up operation of freight trains.

Acknowledgement: The present work was supported by Sichuan Science and Technology Program (2020YJ0308 and 2021YJ0026).

Reference

[1] China broadcasting corporation. ["Thirteenth Five-Year" Achievement Tour] the turnover of railway freight volume ranks first in the world, 2021-01-17.

[2] Jin X, Liu Q. Tribology of wheel and rail, 2004.

[3] Wang C, Luo S, Wu P, et al. Effect of hollow worn tread on dynamic performance of high-speed electric multiple units: 1-8.

[4] Jin X, Zhao G, Liang S, et al. Characteristics mechanisms influences and counter measures of high speed wheel/rail wear, 2018, 54(04): 3-13.

[5] Wu H. Investigation of wheel/rail interaction on wheel flange climb derailment and wheel/rail profile compatibility, 2000.

[6] Cui D, Li L. Wheel-rail profiles matching design considering railway track parameters, 2010(4): 410-417.

[7] Cui D, Li L, Jin X, et al. Numerical optimization technique for wheel profile considering the normal gap of the wheel and rail, 2009, 45(12): 205-211.

[8] Shen G, Ye Z. Unique design method for wheel profile considering contact angle function, 2002, 30 (9): 1095-1098.

[9] Ye Z, Shen G. Design of independently rotating wheel tread shape, 2003,41 (1): 19-21.

[10] Shevtsov I Y, Markine V L, Esveld C. Optimal design of wheel profile for railway vehicles, 2005(258): 1002-1030.

[11] Jahed, Farshi, Eshraghi, Nasr. A numerical optimization technique for design of wheel profiles, 2008, Vol.264. No.1-2: 1-10.

[12] Liu Y. Study on contact geometry and geometric profile optimization of high-speed wheel-rail, 1999.

[13] Cheng D, Wang C, Liu J, et al. Research on the mathematical model for wheel profile optimization with arc parameters as design variables, 2011,32(6): 107-113.

[14] Polach O. Wheel profile design for target conicity and wide tread wear spreading, 2011, 271: 195–202.

[15] Lian S, Li J, Yang W. Analysis of track irregularity spectrum of Shanghai-Kunming and Jinhua-Wenzhou railways, 2010,38(02): 257-262.

[16] Zhou S, Tao Y, Zhang Z. SIMPACK 9 Example Tutorial (Part 2), 2013.

[17] Miao B, Simpack Dynamic Analysis Advanced Tutorial, 2010.

[18] Zhang J. Optimal design research of railway vehicle wheel profile, 2012.

[19] Chen Z, Wang C. Railway vehicle dynamics and control, 2004.

[20] Ministry of railways of the people's republic of China. TB/T 449-1976 Wheel profile for locomotive and vehicle, 1976.

[21] Oldrich Polach, A. Vetter. methods for running stability prediction and their sensitivity to wheel/rail contact geometry. Extended abstracts of the 6th international conference on railway bogies and running gears, Budapest, September 2004: 62-64.

[22] Cui D, Li L, Jin X, et al. Influence of vehicle parameters on critical hunting speed based on Ruzicka model, 2012, 25(03): 536-542.

[23] Yu L. MATLAB intelligent algorithm 30 case analysis, 2015.

[24] Lei Y, Zhang S. MATLAB genetic algorithm toolbox and application, 2014.

[25] Standardization Administration. GB/T 5599-2019 Specification for dynamic performance assessment and testing verification of rolling stock, 2019.

Viser Technology Pte. Ltd.
Mechanical Engineering Science
DOI: 10.33142/mes.v3i1.4335

Research Article Open Access

Embedment Effect on Eliminating Damage of CFRP Pull-riveting Process by Simulation Study

Yiqi WANG*, Zhiwei CONG, Guang XIAO, Yongjie BAO , Hang GAO

Key Laboratory for Precision and Non-traditional Machining Technology of Ministry of Education, Dalian University of Technology, Dalian, China

***Corresponding Author:** Yiqi WANG, E-mail: wangyiqi@dlut.edu.cn*

Abstract:
The rivet joints have been widely applied in aerospace and vehicle fields. During the joining process of the carbon fiber reinforced plastic (CFRP) laminates, the pre-tightening force of pulling-rivet was the key factor to ensure the connection performance. To predict the impact of clamping loads on stress and failure of laminates, the value of stress and damage evolution of the wall of a hole under the pre-tightening force were simulated by the finite element method. The results of the simulation showed that excessive clamping force led to the damage and failure of CFRP in the hole edge. Connection performance together with progressive failure process and failure modes of CFRP laminates with various pre-tightening forces were investigated. A kind of metal embedded parts embedded in the laminates was designed to reduce the damage by the simulation study. Simulation results showed that embedment reduced the failure and damage efficiently. The embedment reduced about 64% of the maximum stress.

Keywords: *embedment effect; CFRP riveted; damage evolution; damage removal*

1 Introduction

As people pay more and more attention to energy-saving and pollutant emission reduction, the demand for lightweight materials is increasing. Carbon Fiber Reinforced Polymer (CFRP) has become the preferred material for current aircraft manufacturing due to its excellent properties of lightweight and high strength. CFRP consumptions of the American Boeing 787 aircraft and the European Airbus A350XWB aircraft are more than 50%, and that of the Commercial Aircraft Corporation of China C919 aircraft reaches 12% [1-3]. In recent years, CFRP is used widely in the automotive manufacturing industry [4].

However, due to the lack of relevant theoretical methods and key technologies, the connection of composite components faces many challenges. CFRP inevitably is connected by bolting [5], riveting [6], adhesive bonding [7,8], welding [9,10], and hybrid junction [11]. Bolting is the most favorite method. The main advantages of bolting connections are easy assembly and disassembly, no special surface treatment, less environmental impact, high load carrying capacity, and high connection reliability, which is the most widely used in the aviation industry [12-15]. However, the main problems of these connection methods are destroying the integrity of the structure and having high-stress concentration around the fastener holes deteriorating joint strength, which is much more complicated and severe in CFRP laminates compared to metallic counterparts as a consequence of their inhomogeneity and anisotropy [16].

Some scholars provided much information on mechanical performance and failure mechanisms about solely bonded and riveted joints. Yang et al. [17] developed a new progressive damage model to investigate the flexural behavior and the damage evolution of CFRP laminates subjected to three-point bending. Gomez et al. proposed a simple analytical model combining spring and damper that reproduces the behavior of a structural rive joint, with less than 15% error level compared with experimental curves [18]. Simplified finite element models were also proposed to analyze stress distribution and further predicted the joint performance. Pirondi et al. [19] simulated the failure behavior of riveted joints and found that the stiffness, peak load, and energy absorption of the riveted joints agree well with the corresponding experimental results. Chowdhury et al. [20] conducted a finite element study on thin carbon fiber double lap joints. The results show that the addition of fasteners in the composite joint significantly reduces the strain energy release rate compared to the single-bond joint, thereby greatly reducing the crack propagation speed.

The researchers also studied the effect of joint

Received 20 January 2021; Accepted 23 May 2021

configuration on the mechanical properties of different joints. Sadowski et al. [21] studied the effect of the rivet arrangement geometry on the mechanical properties of riveted joints under mechanical loading. The test results show that the hybrid joints arranged with 1 + 2 type rivets are the best solution for the connection of structural members under the joint action of three kinds of rivets.

The present work aims to study the failure load and failure mode in the process of riveting in different Pre-tightening forces and how to reduce the damage in the CFRP laminates. Load-displacement curves together with peak load, energy absorption, and joint stiffness were studied. A metal embedded part was designed to reduce the failure.

2 Progressive damage model

To take into account the failure and damage of CFRP laminates effectively, a three-dimensional nonlinear progressive damage analysis model at the mesoscale level was presented. In this study, the failure criterion of the CFRP pack case was analyzed with a three-dimensional composite material failure criterion based on the Hashin-type criterion.

At first, strain and damage-free stiffness matrix based on the assumption of transverse isotropy were used to calculate the initial stress by the following equation:

$$\sigma = C^0 : \varepsilon \tag{1}$$

And then, the 3D Hashin damage criteria were as follows:

Fiber tensile failure (FT), $\varepsilon_1 > 0$:

$$\left(\frac{\varepsilon_1}{X_t/C_{11}}\right)^2 + \left(\frac{\gamma_{12}}{S_{12}/C_{44}}\right)^2 + \left(\frac{\gamma_{13}}{S_{13}/C_{55}}\right)^2 = e_{FT}^2 \tag{2}$$

Fiber compressive failure (FC),$\varepsilon_1 > 0$:

$$\left(\frac{\varepsilon_1}{X_c/C_{11}}\right)^2 = e_{FC}^2 \tag{3}$$

In-plane matrix cracking (IMT), $\varepsilon_2 > 0$:

$$\left(\frac{\varepsilon_2}{Y_t/C_{22}}\right)^2 + \left(\frac{\gamma_{12}}{S_{12}/C_{44}}\right)^2 + \left(\frac{\gamma_{23}}{S_{23}/C_{66}}\right)^2 = e_{IMT}^2 \tag{4}$$

In-plane matrix crushing (IMC), $\varepsilon_2 > 0$:

$$\left(\frac{\varepsilon_2}{Y_c/C_{22}}\right)^2 + \left(\frac{\gamma_{12}}{S_{12}/C_{44}}\right)^2 + \left(\frac{\gamma_{23}}{S_{23}/C_{66}}\right)^2 = e_{IMC}^2 \tag{5}$$

Out-of-plane matrix cracking (OMT), $\varepsilon_3 > 0$:

$$\left(\frac{\varepsilon_3}{Z_t/C_{33}}\right)^2 + \left(\frac{\gamma_{13}}{S_{13}/C_{55}}\right)^2 + \left(\frac{\gamma_{23}}{S_{23}/C_{66}}\right)^2 = e_{OMT}^2 \tag{6}$$

Out-of-plane matrix crushing (OMC), $\varepsilon_3 > 0$:

$$\left(\frac{\varepsilon_3}{Z_c/C_{33}}\right)^2 + \left(\frac{\gamma_{13}}{S_{13}/C_{55}}\right)^2 + \left(\frac{\gamma_{23}}{S_{23}/C_{66}}\right)^2 = e_{OMC}^2 \tag{7}$$

Fiber-matrix shear-out (OMC),$\varepsilon_1 < 0$:

$$\left(\frac{\varepsilon_1}{X_c/C_{11}}\right)^2 + \left(\frac{\gamma_{12}}{S_{12}/C_{44}}\right)^2 + \left(\frac{\gamma_{13}}{S_{13}/C_{55}}\right)^2 = e_{FMS}^2 \tag{8}$$

The ε_i (i=1,2,3) was normal stress, and the γ_{ij} (i,j=1,2,3; i≠j) was shear strain. The C_{ij}(i,j=1,2,3,4,5,6) was stiffness coefficient in the stiffness matrix. The S_{12}, S_{13}, S_{23} were the shear strengths of the laminate. The X_t, Y_t, Z_t represented the tensile strengths in the longitudinal direction, transverse direction, and through-thickness direction, respectively. The X_c, Y_c, Z_c represented the compressive strengths in the longitudinal direction, transverse direction, and through-thickness direction, respectively. The S_{12}, S_{13}, S_{23} were the shear strengths of the laminate.

The e was the failure factor used to characterize the damage degree of the material. For arbitrary mesh style, once $e \geq 1$, it indicated that the material had been damaged. And corresponding unit property degradation was required. There were two main ways of property degradation: one was the reduction of elastic modulus, the other was the reduction of stiffness.

3 Modeling

3.1 Specimen details

In order to verify the strengthening effect of embedment, numerical simulations on comparison of laminates without embedment and laminates with embedment were conducted. The schematic diagram of the two comparison models was shown in Fig.1. Fig. 2 showed the concrete geometries and dimensions of the riveted joint specimens. The specimens' sizes were referred to as the TB/T 1335-1996 Standard.

In order to observe the simulation results, the laminate was designed to the square and the length of the side was 100mm. The pulling rivet of LMTF and LMY type rivet sleeve was chosen in the simulation and the diameter of the pulling rivet was 16mm. The length of the rivet rob was 14mm. The contact area between the rivet head and bottom laminate was 415mm^2 and the contact area between the rivet sleeve and top laminate was 548mm^2. Clearance fit between rivet and laminate was used in the assembly, so the diameter of the central hole in the laminate without embedment was set to be 17.5mm. While the diameter of the center hole in laminates with embedment was 37.5mm. As a result of the embedment was implanted in the laminates and the embedment was stair-stepped, the diameter of the cylindrical groove in the laminates was 48mm. The thickness of laminate was 7mm with a thickness of 0.2mm per ply and the stacking sequence was (0/90)2s.

In order to enhance the connection strength between embedment and laminates, designed to be ladder-like. The diameter of the central hole in the embedment was 17.5mm. The upper half part's thickness of embedment was 4mm and the thickness of the lower half part was 3mm. The diameter of the upper ladder was 1.2 times bigger than the diameter of the pulling rivet's head. The diameter of the pulling rivet's head was 28mm, and the upper ladder's diameter was 33.6mm. The bottom ladder's diameter was 48 mm. Fig.1(c) showed the sectional view of the central area of the laminate. The contact area between the embedment and laminates used adhesive to improve the strength. In this simulation, adhesive was replaced by the tie.

3.2 Material properties

The fiber material used in finite element analysis was standard modulus woven carbon fiber T300, while matrix material was unsaturated epoxy resin E54. The properties of the CFRP laminates referred from the datasheet of Toray Company's composites were listed in Table 1, in which the parameters were from the manufacturer. Pulling rivet and rivet sleeve were both used carbon structural steel

Q235B which was widely employed in railway vehicle connection. And the property of Q235B was given in Table 2. Considering the effect of ensuring connection strength and weight loss and ensuring connection strength, the embedded part employed Al-2024-T3 and the property of which was presented in Table 3.

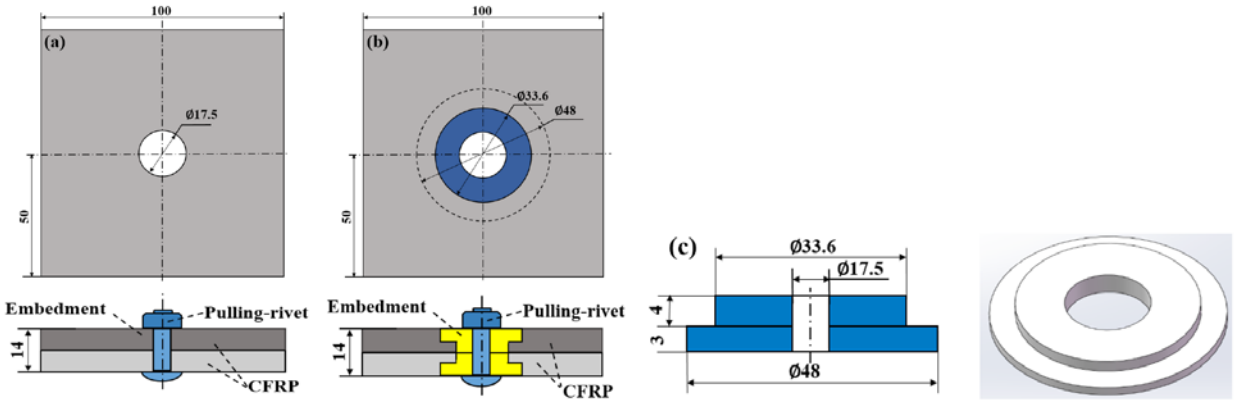

Fig.1 Geometry and dimensions of pulling riveted joint specimens: (a) CFRP laminates without embedment, (b) CFRP laminates with embedment, (c) metal embedment.

Table 1 The mechanical properties of the CFRP laminates

E1 [GPa]	E2 [GPa]	E3 [GPa]	u12	u13	u23	G12 [GPa]	G13 [GPa]	G23 [GPa]
135	8.17	8.17	0.33	0.33	0.48	4.27	4.27	2.75

Table 2 Mechanical and physical properties of Q235B

Density [g/cm3]	Tensile modulus [GPa]	Yield stress [MPa]	Tensile strength [MPa]	Poisson's Ratio
7.8	210	235	580	0.3

Table 3 Mechanical and physical properties of Al-2024-T3

Young's Modulus [GPa]	Yield Stress [MPa]	Ultimate Stress [MPa]	Poisson's Ratio
7.8	210	235	580

3.3 FE simulation

3D finite element (FE) models were established for accurate stress analyses of the specimens by the software ABAQUS 2016/Standard. Fig. 2 presented the sectional view of FE model with virtual material layers representing the rough contact surfaces. The model Ⅰ was composed of two CFRP laminates, one pulling rivet, one rivet sleeve, and model Ⅱ added two embedded parts on the basis of model Ⅰ. In order to simplify the numerical simulations and shorten the calculating time, the pulling rivet and rivet sleeves were merged into a dumbbell-shaped component.

The CFRP laminate was divided into 35 layers in the thickness direction and each ply was a single layer. The C3D8R solid elements with enhanced hourglass control were used to simulate the failure process of CFRP laminates. In order to make the calculation more accurate, the meshes of the joint-hole region were refined highly with an element size of 0.4×0.4×0.55 mm. The properties of laminates were defined by the user material. The continuum damage mechanics was implemented in ABAQUS 2016 through a UMAT subroutine for further simulation. Three contact pairs were established in the model Ⅰ, including between top laminate and bottom laminate, between the CFRP and pulling rivet, between the CFRP and rivet sleeve. In model Ⅱ, four contact pairs were established. Between top laminate and bottom laminate, between top embedment and bottom embedment, between pulling rivet and embedment, between rivet sleeve and embedment were included. In order to prevent elements interpenetration at the edges of the parts, surface-to-surface discretization was used in the contacts of various parts. In the simulation, the CFRP laminates were the master surface for the pulling rivet head-to-laminate and the surface of pulling rivet was selected as the slave surface for the rivet sleeve-to-embedment. The penalty method with hard contact, friction, small sliding, and finite sliding was used to solve the contacts. The values of frictional coefficient for laminate-to-laminate (FC1), embedment-to-embedment (FC2), pulling rivet head-to-laminate (FC3), rivet sleeve-to-laminate (FC4), pulling rivet shank-to-laminate interfaces (FC5), pulling rivet head-to-embedment (FC6), rivet sleeve-to-embedment (FC7), rivet shank-to-embedment interfaces (FC8) were 0.1, 0.3, 0.2, 0.2, 0.1 0.3,0.3,0.1 respectively, which was based on the previous experiments and studies.

Regarding the step type itself, static general analysis was used for this model. In order to apply the preload, the

bolt load plane was created in the middle of the pulling rivet. The 170 kN which was the ultimate force of pulling rivet snapped was imposed the bolted load plane. The pre-tightening force was divided into two-step to simulate fluently. The pre-tightening force was created on the propagated to the subsequent analysis step. The preload of step-1 was 1 kN and step-1 was 170 kN.

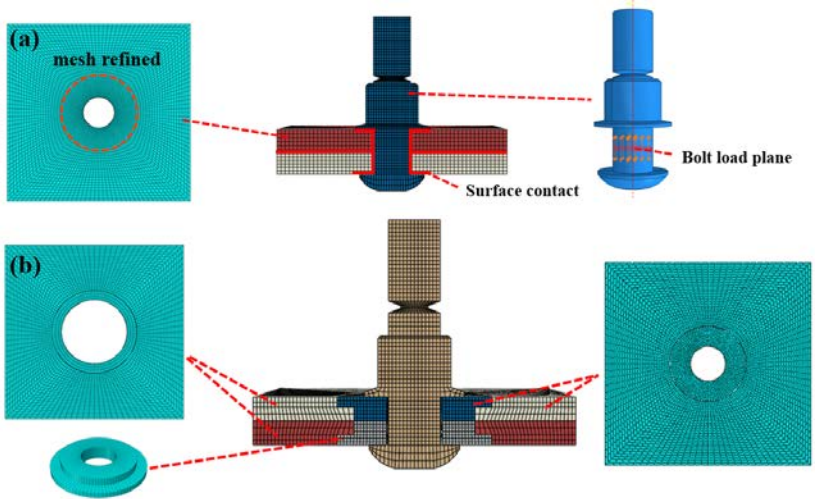

Fig.2 3D FE model of pulling riveted joint: (a) model Ⅰ: without embedment, (b) model Ⅱ: with embedment.

4 Results and discussion

The stress distribution, deformation, and damage of CFRP laminates and embedment were presented and discussed in detail. The pre-tightening force of rivet effect mechanisms was analyzed comprehensively based on the numerical results.

4.1 Stresses

4.1.1 Stresses distribution of laminates without embedment

The section view of typical stress contours around the central hole was given in Fig. 3. The critical zone for each stress component was marked by a dotted line. It could be seen from Fig. 3 and Fig. 4 that the critical zones for all stress concentrations occurred at the contact area of laminates as a result of pre-tightening force clamping, which may cause the damage and delamination of CFRP laminates. The stress S33 was taken main stress and the maximum of stress S33 was located in the contacting region between rivet and laminates because the orientation of the pre-tightening was along the Z-direction. Due to the impact of the preload from riveters, the riveting-head and the riveting sleeve-set were squeezed from both sides to the middle, stress main concentrated on the contact area. In Fig. 3(d), the value of S33 in the zone marked by the blue rectangle dotted line was negative as a result of CFRP laminates were subjected to extrusion which was opposite of the positive direction of Z-direction from pulling rivet-head and rivet sleeve. From Fig. 3(d) and Fig. 4(d), the S33 value of the red region was positive because this region expanded outward under the preload, and the expansion direction was consistent with the positive direction of the Z-direction.

The stress S11 and S22 represented respectively the stress along fiber-direction and matrix-direction. The S11 and S22 were generated because rivet contacted hardly with the hole-wall during the riveting process and the interlaminar strength of CFRP is not enough. The S11 and S12 concentrated principally in the butting area between two laminates around the central hole extended along radius direction as were depicted in Fig. 3(a) (b) and Fig. 4(a) (b). The value of S11 was higher than the value of S22 because the compressive strength of carbon fiber was lower than the matrix. The value of S12 was far lower than the value of S11 and S12 concentration areas of S12 were mainly located in the direction of 45°and -45°illustrated in Fig. 3(c) and Fig. 4(c).

Because of the ply orientation effect, the critical zones of stress were non-uniform in the laminates. In order to describe visually stress distribution around the fastener hole, some paths were set in the radius, thickness, and circumference direction. The thickness and circumference direction path was created at the contacting area between upper laminate and lower laminate. Fig. 5(a) gave the relative Mises stress along the thickness path, which was the bottom of the lower plate to the top of the upper plate along the central hole-wall. It could be seen that the radial stress was almost symmetric. It indicated that the maximum position of stress was located in the contact area between the laminates and the stress gradually decreased from the middle to both sides, which was accordant with the Figs. 3(a-c). Fig.5 (b) showed the variation of stress along the radius direction. The numerical results showed that stress was continuous. The stress curves of the bottom side of the upper laminate and the top side of the lower laminate were coincident. As the radius increased, the stress decreased gradually. When the distance from the hole wall was 10mm, the stress reduced to the safe zone. The stress of circumferential direction was depicted in Fig.5 (c), the maximum stress was at the edge of the hole wall and the stress of circle direction decreased with circumferential expanding. The stress variation trend was almost consistent with Fig.5 (c).

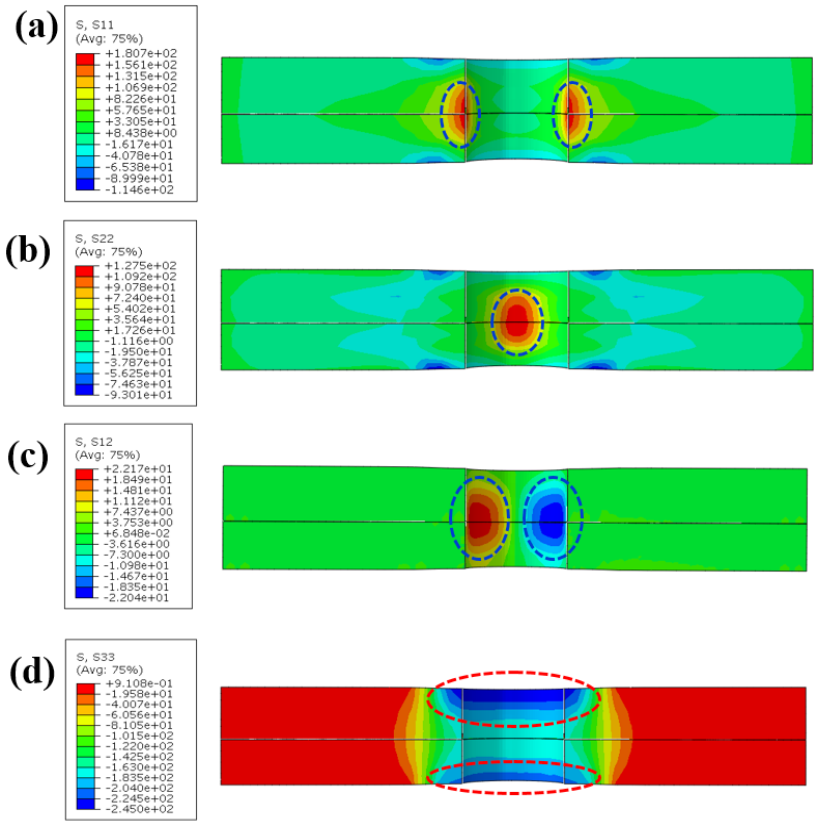

Fig.3 Stress profile view of laminate without embedment: (a) S11, (b) S22, (c) S12 (d) S33.

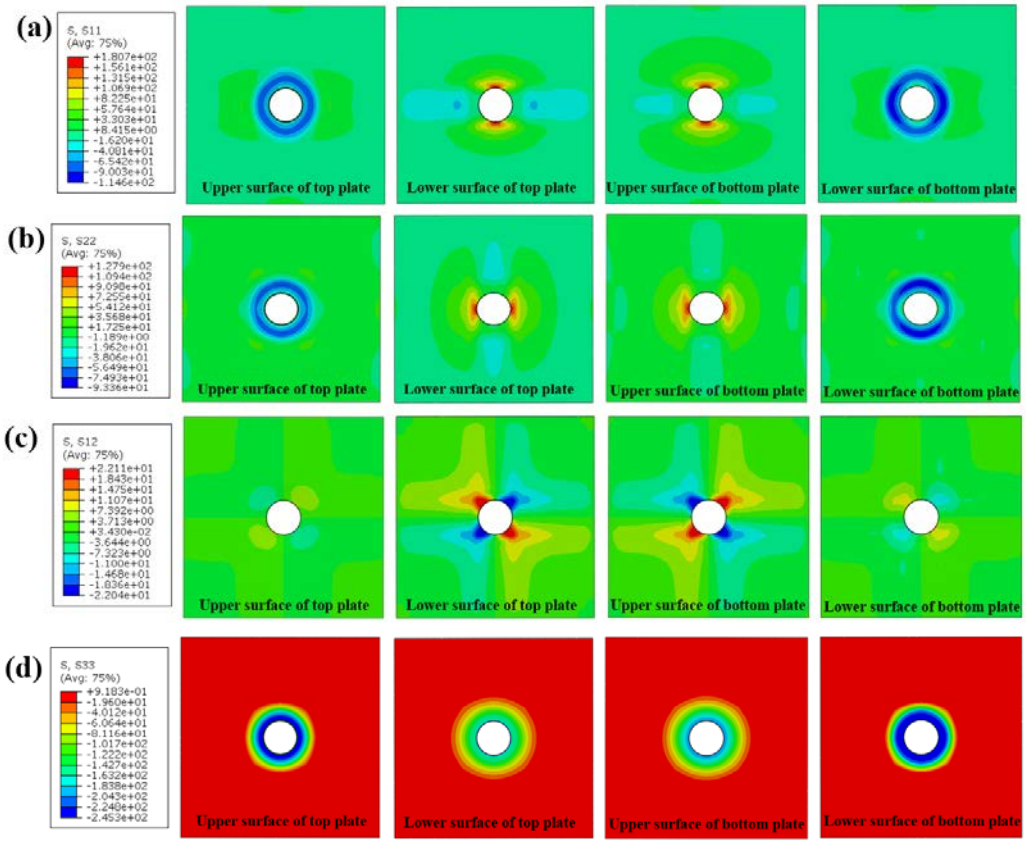

Fig.4 Surface stress distribution diagram of laminates without embedment in different directions: (a) S11, (b) S22, (c) S12, (d) S33.

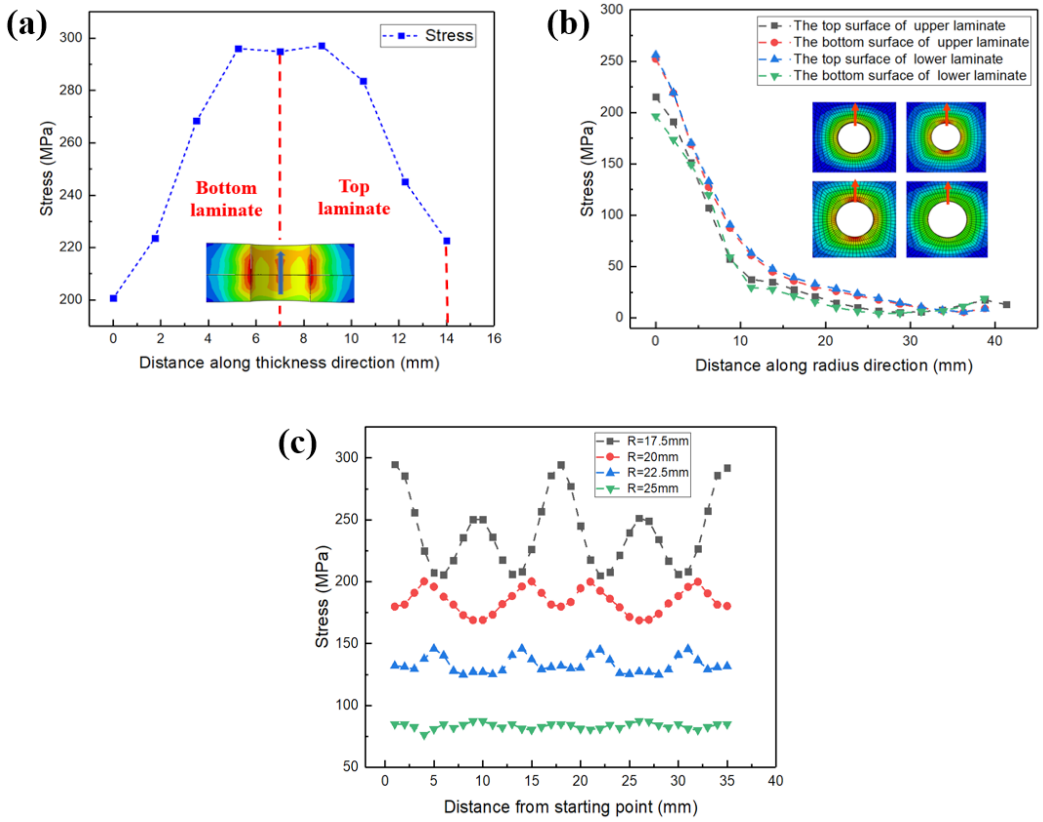

Fig.5 The stress of laminates without embedment along various paths: (a) stress along the thickness direction, (b) stress along radius direction, (c) stress along circumference direction.

4.1.2 Stresses distribution of laminates without embedment

Fig. 6 and Fig. 7 presented the stress distribution of laminates with embedment. The maximum pressure was 56.87 MPa, which didn't exceed the fiber and matrix strength. Thus there wasn't damage to the laminates. As depicted in Fig. 6(a) and (b), the stress S11 and S22 were distributed symmetrically along the X-axis and Y-axis respectively. The stress concentration mainly occurred on the upper area of the bottom laminate, which was due to the pressure from the rivet head-side larger than the pressure from the rivet nut-side. And the frictional force between the two laminates could lead to the stress concentration area. In Figs. 6 (a-b) and Figs. 7 (a-b), the stress of the blue region was negative because this area existed internal tension which was generated during riveting and the direction of tension was opposite from the positive direction of the X-axis and Y-axis. The inner tension expanded from the central hole to the side of the laminates and decreased gradually. The value of stress S12 was too small to affect the whole stress distribution from Fig. 6 (c) and Fig. 7(c). The stress S33 has distributed the direction of 45°and -45°, and the stress was small extremely.

The stress of laminates with embedment along various paths is illustrated in Fig. 8.

4.1.3 Stress distribution of embedment

Fig. 9 showed the stress distribution of the embedded part. The maximum stress was 431.3 MPa, which was far less than the ultimate load of aluminum. So using metal embedded parts could offset contact main contact stress thus reducing the damage of CFRP. From Figs. 9(a-c), the surface stress spread radially from the central hole to the sides, which was verified in Fig. 10. In Fig. 9(d), the position of maximum stress was located in the lower region of the bottom laminate as a result of the hard contact between the bottom laminate and pulling rivet-head.

To present the path effect on the stress distribution, the stresses along the radius and thickness direction of laminates were plotted in Fig. 10. In the radius direction, the stress decreased with the radius increased from the center hole. In Fig. 9(b), zone A was the stress concentration area and zone B was the safety region and the area of safety was more than half of the area of embedded parts, so the embedment could sure that large values of stress were not transferred to the laminates. In the thickness direction, there was little difference in stress, which indicated contact stress distribution of embedded part was homogenous.

4.2 Local deformations of laminate around the rivet hole

Fig. 11(a) gave the deformations of laminates without laminates. The maximum deformation was the same position as the maximum stress. On the whole, the deformation of the lower plate was greater than the upper plate as illustrated in Fig. 11(a), which was the pressure from the rivet-head was higher than the pressure from the rivet-sleeve. In the clamping loading process, the top laminate's deformation increased slower than the bottom laminate.

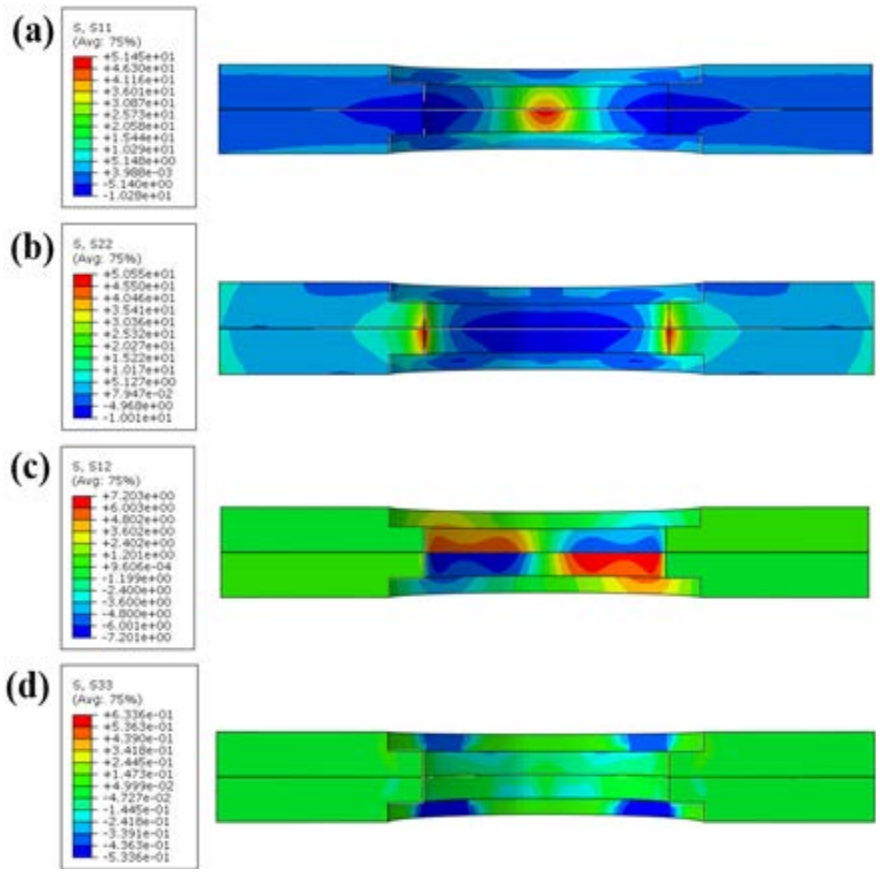

Fig.6 Stress profile view of laminate with embedment: (a) S11, (b) S22, (c) S12, (d) S33.

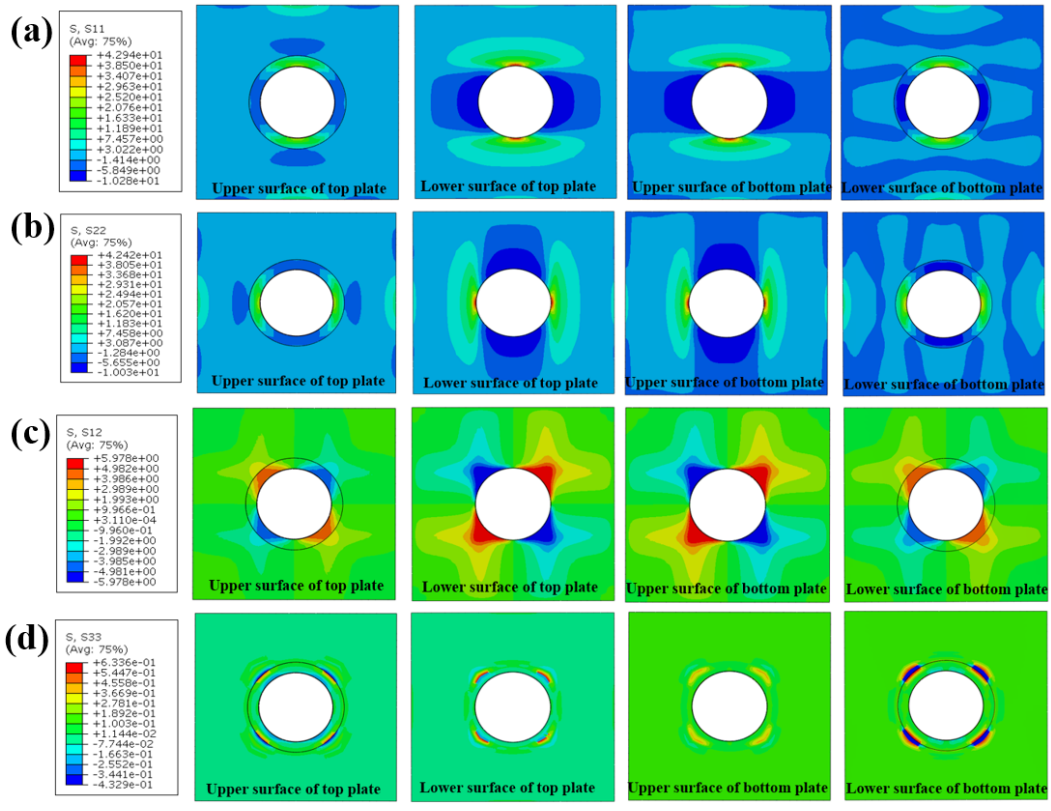

Fig.7 Surface stress distribution diagram of laminates with embedment in different directions: (a) S11, (b) S22, (c) S12, (d) S33.

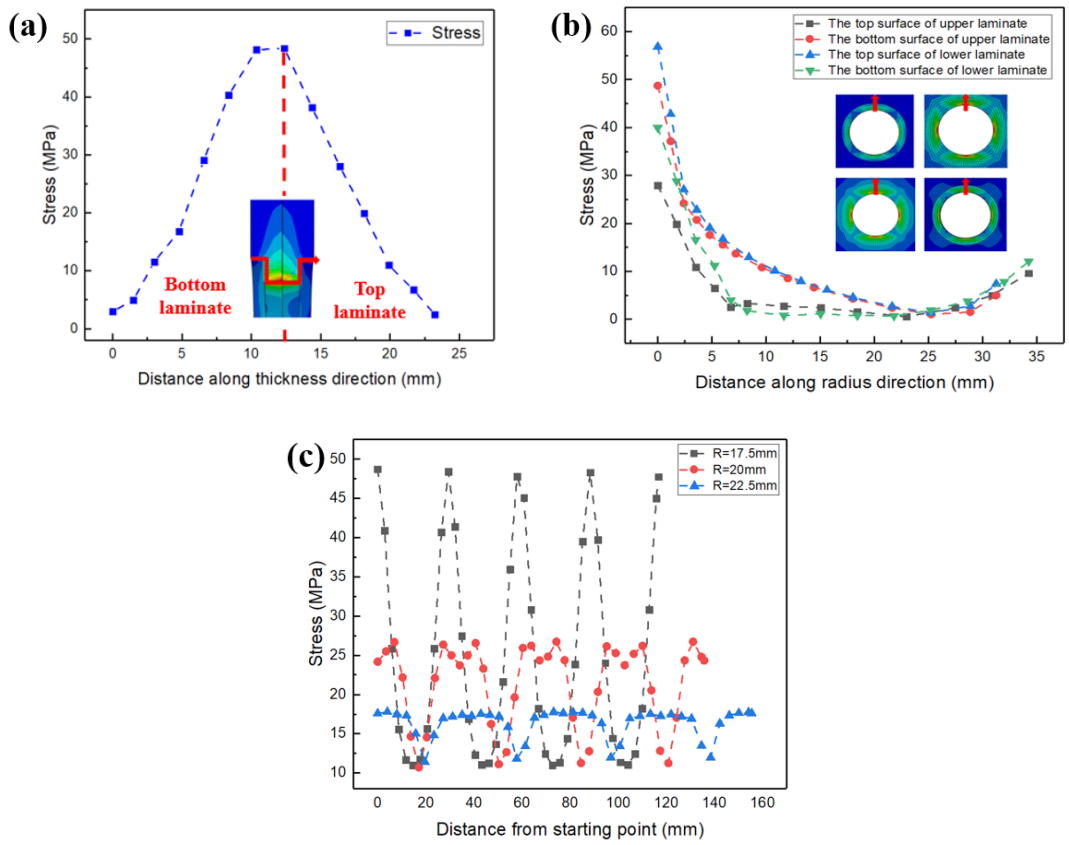

Fig.8 The stress of laminates with embedment along various paths: (a) stress along thickness direction, (b) stress along radius direction, (c) stress along circumference direction.

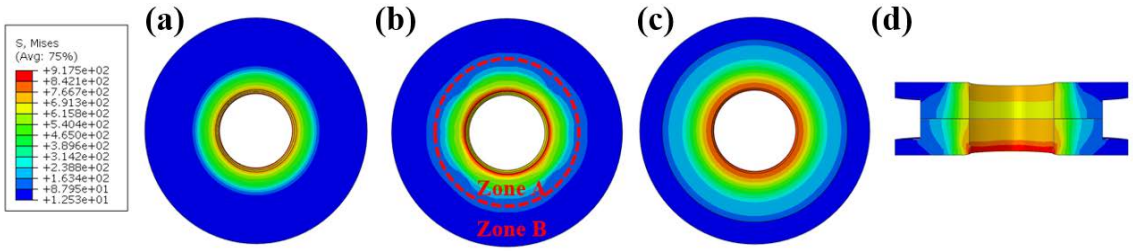

Fig.9 The stress of embedment: (a) top surface, (b) bottom surface, (c) contact surface of two laminates, (d) profile view of embedment.

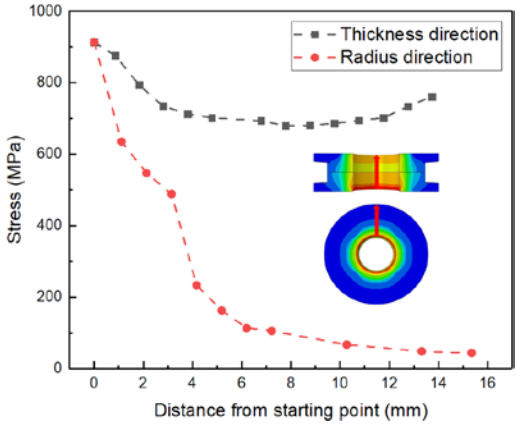

Fig.10 Stress distribution of embedment along a different path.

The top laminate contacting with rivet sleeve and bottom laminate contacting with pulling rivet-head was sinking due to clamping action from the pre-tightening force. The sinking direction was towards the middle. In the meanwhile, warping deformation occurred on the sides of laminates. In Fig. 11(b), the deformation of each position in the laminates was far less than the laminates without embedment. The maximum deformation position didn't occur in the central hole because the embedment bears most of the deformation. The sides of laminates with embedment also had warping deformation, but the value of deformation far lower than the deformation of laminates without embedment. Zone D exhibited a negative deformation state since the deformation direction was towards the negative direction of the z-axis, while the deformation of zone C was positive because the deformation direction with the z-axis's positive direction was consistent.

The deformation along different paths was shown in Fig.12. From Fig. 12, we could see the distance between top laminate and bottom laminate getting larger and larger as the distance increased. The schematic diagram of riveting finished was shown in Fig. 14. Due to the clamping force, there was a gap between the two plates. It could be seen that the radial deformation of the first half changed almost linearly from Fig.12 (a), which indicated that the deformation of the first half was uniform. And the curves of laminates along the radius were almost symmetric. For top laminate, the largest relative radial deformation was smaller than bottom laminate. The maximum distances of laminates without embedment and laminates with embedment were 0.11mm and 0.022mm respectively illustrated in Fig. 12. The value of the maximum distance between laminates decreased by 80%. Thus it could be seen that embedment played a significant role in reducing layer deformation.

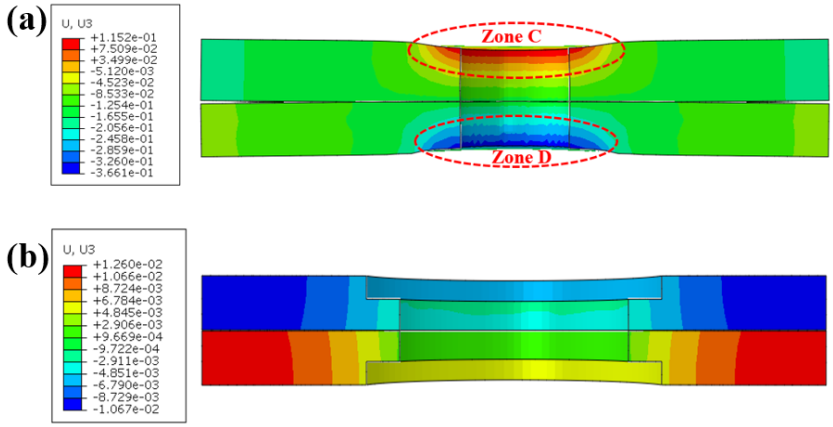

Fig.11 Relative deformation of laminates: (a) without embedment, (b) with embedment.

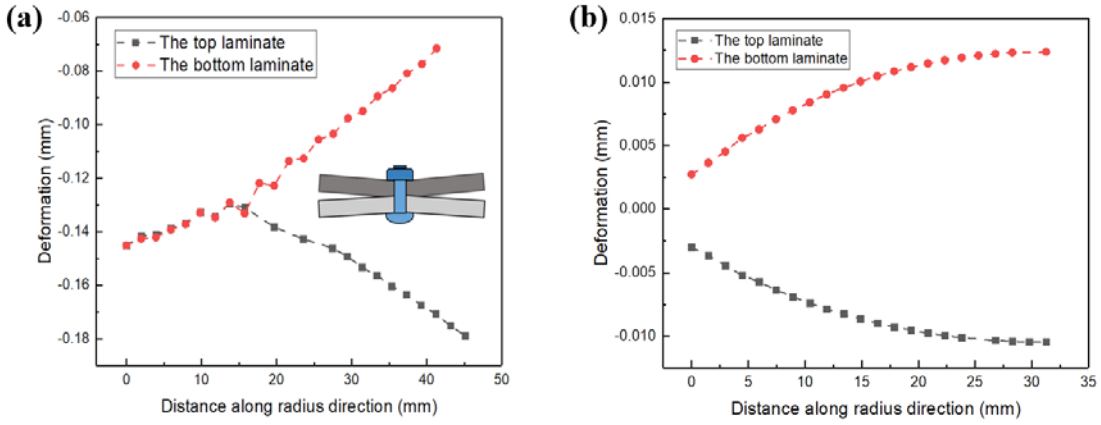

Fig.12 Relative deformation of contact area between top laminate and bottom laminate: (a) without embedment, (b) with embedment.

4.3 Local damages of laminate around the rivet hole

The damage of laminates without embedment is illustrated in Fig. 13. It could be observed that damage occurs near the wall of the hole due to the stress concentration feature and the hole was radially compressed and expanded circumferentially. Fiber and matrix compressive damage generated initially closed to the surface of laminates due to contact stress between laminates and fasteners. Damage extended afterward to the contact area of the two plates along the hole wall until the pulling riveting process was

completed. The variation trend of in-plate damage was consistent with the variation of stress. In contrast, there wasn't damage in the CFRP laminates with embedment due to the embedment took most of the stress from Fig. 13. The embedment could inhibit the damage of CFRP laminates during the riveting process.

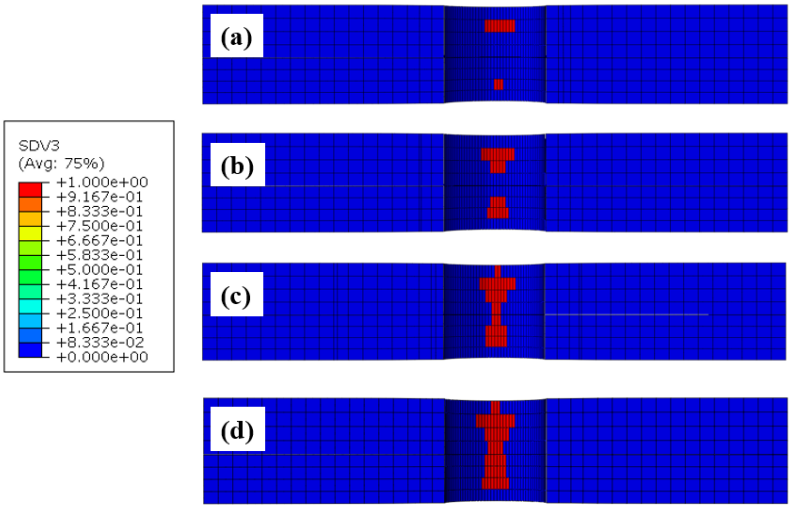

Fig.13 Progressive failure evolution of laminates: (a) damage initiation, (b) ultimate load, (c) damage propagation, (d) failure.

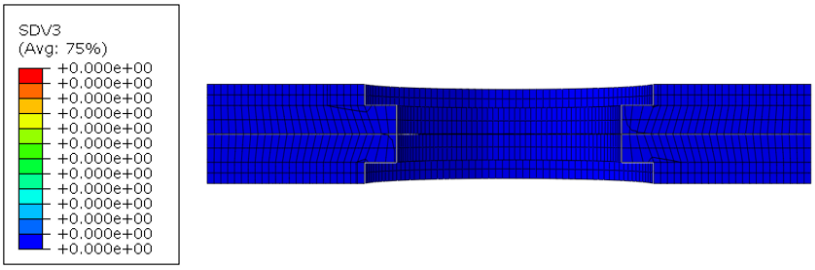

Fig.14 Damage condition of laminates with embedment.

5 Conclusions

This paper investigated the stress, deformation, and failure mechanism of pulling riveted joints when connecting CFRP laminates. The simulation results could be applied to the automotive industry to improve the mechanical properties and reliability of CFRP, which also helped to further understand the progressive failure process and fracture mechanism of CFRP-CFRP joints made with different joining methods and design parameters. The following conclusions can be drawn from the above study.

(1) During the pulling riveting process, stress concentration occurred close to the central hole and led to the failure of the laminates as a result of excessive clamping force.

(2) The simulation results showed that embedment embedded in the CFRP laminates reduced the stress concentration and damage near the hole-wall. About 64% of the maximum stress was reduced by using the designed embedment.

(3) Progressive failure process of riveted joint indicated that clamping load led to crack initiation and propagation on the edge of the hole of CFRP laminates. Fracture of the adhesive layer was predicted before the mechanical failure of the rivet.

References

[1] V Krishnaraj, R Zitoune, F Collombet. Comprehensive review on drilling of multi material stacks. J Mach Forming Technol 2010(2):1–32.

[2] C Campbell. Structural assembly. In: Campbell FC,. Manufacturing technology for aerospace structural materials. Oxford: Elsevier Science; 2006.

[3] Y Rhee, J Yang. A study on the peel and shear strength of aluminum/CFRP composites surface-treated by plasma and ion assisted reaction method. Compos Sci Technol 2003(63):33–40.

[4] F. Lambiase, D Ko. Feasibility of mechanical clinching for joining aluminum AA6082- T6 and Carbon Fiber Reinforced Polymer sheets, Mater. Des. 2016 (107): 341–352.

[5] J Hu, K Zhang, Q Yang, H Cheng, S Liu, Y Yang. Fretting behavior of interference between CFRP and coated titanium alloy in composite interference-fit joints under

service condition. Mater Des 2017 (134):91–102.
[6] F Lambiase. Mechanical behavior of polymer-metal hybrid joints produced by clinching using different tools. Mater Des 2015(87):606–18.
[7] T Kim, J Kweon, J Choi. An experimental study on the effect of overlap length on the failure of composite-to-aluminum single-lap bonded joints. J Reinf Plast Comp 2008; 27(10):1071–81.
[8] N Tsouvalis, V Karatzas. An investigation of the tensile strength of a composite-to-metal adhesive joint. Appl Compos Mater 2011, 18(2):149–63.
[9] J Esteves, S Goushegir, J Santos, et al. Friction spot joining of aluminum AA6181-T4 and carbon fiber reinforced poly (phenylene sulfide): effect of process parameters on the microstructure and mechanical strength. Mater Des 2014, 66(4):437–45.
[10] B Frank, W Guntram, E Dietmar. Ultrasonic metal welding of aluminium sheets to carbon fibre reinforced thermoplastic composites. Adv Eng Mater 2010, 11(1–2):35–9.
[11] F Smith. An innovation in composite to metal joining. Mater Process Rep 2004, 20(2):91–96.
[12] A Pisano, P Fuschi. Mechanically fastened joints in composite laminates: Evaluation of load bearing capacity [J]. Composites Part B: Engineering, 2011, 42(4):949-961.
[13] F Irisarri, F Laurin, N Carrere, et al. Progressive damage and failure of mechanically fastened joints in CFRP laminates – Part I: Refined Finite Element modelling of single-fastener joints [J].Composite Structures, 2012, 94(8):2269-2277.
[14] T Qin, L Zhao, J Zhang. Fastener effects on mechanical behaviors of double-lap composite joints [J]. Composites structures, 2013(100):413-423.
[15] A Pramanik, A K. Basak, Y Dong, et al. Joining of carbon fibre reinforced polymer (CFRP) composites and aluminium alloys – A review [J]. Composites Part A: Applied Science and Manufacturing, 2017(101):1-29.
[16] G Lim, K Bodjona, K Raju, S Fielding, V Romanov, L Lessard. Evolution of mechanical properties of flexible epoxy adhesives under cyclic loading and its effects on composite hybrid bolted/bonded joint design, Compos. Struct. 2018 (189) :54–60.
[17] Y Yang, X Liu, Y Wang, et al. A progressive damage model for predicting damage evolution of laminated composites subjected to three-point bending. Composites Science and Technology 2017 (151):85-93.
[18] S Gómez, J Oñoro, J Pecharromán. A simple mechanical model of a structural hybrid adhesive/riveted single lap joint, Int. J. Adhes. Adhes. 2007 (27) 263–267.
[19] A Pirondi, F Moroni. Clinch-bonded and rivet-bonded hybrid joints: application of damage models for simulation of forming and failure, J. Adhes. Sci. Tech. 23 (2009) 1547–1574.
[20] N Chowdhury, J Wang, W Chiu, P Chang. Experimental and finite element studies of thin bonded and hybrid carbon fibre double lap joints used in aircraft structures, Compos. Part B-Eng. 2016 (85):233–242.
[21] T Sadowski, E Zarzeka-Raczkowska. Hybrid adhesive bonded and riveted joints – influence of rivet geometrical layout on strength of joints, Arch. Metall. Mater. 2012 (57):1127–1135.

Viser Technology Pte. Ltd.
Mechanical Engineering Science
DOI: 10.33142/mes.v3i1.4336

Research Article Open Access

Influence of Curve Geometric Parameters on Curving Performance of Sub-frame Radial Bogie

Chunlei YANG[1]*, Yunhua HUANG[2], Junjun DING [2]

1. School of Information Engineering, Hubei Minzu University, Enshi 445000, Hubei, China;
2. School of Mechanical Engineering, Southwest Jiaotong University, Chengdu 610031, Sichuan, China

***Corresponding Author:** Chunlei YANG, School of Information Engineering, Hubei Minzu University, Enshi 445000, Hubei, China 2015017@hbmy.edu.cn*

Abstract:
Based on the theory of vehicle-track coupling dynamics, the coupling dynamic model of the freight car mounted with the sub-frame bogies and the numerical model of curved track were established, utilizing the fast numerical integration method, the curving performance of the vehicle was simulated to study the influence of the curve geometric parameters such as curve radius, transition curve length and superelevation of outer rail on the wheel-rail dynamic interaction. The simulation results indicate that: (1) Increasing the curve radius can decrease the wheel-rail wear, but the effect will weaken while the curve radius is greater than 800m. (2) If the transition curve length is less than 30m, vibrations will appear at the transition-circle connecting point, and the smaller the transition length, the bigger the vibrations, the worse the wheel-rail wear, but when the length is bigger than 50m, its further variation has very little effect on wheel-rail wear. (3) The superelevation of outer rail can affect the distribution and difference of the inner and outer wheel-rail forces, and too large deficient or excessive superelevation will worsen the wheel-rail wear either. However, an appropriate deficient superelevation of outer rail (e.g. <20mm) is helpful to reduce the wheel-rail wear, which is consistent with the engineering practice of settling a certain deficient superelevation value.

Keywords: *heavy-haul freight car; sub-frame radial bogie; curve geometric parameters; wheel-rail wear*

Heavy-haul transportation is an effective way to enhance the railway transport capacity, but the problem of wheel-rail wear and rail fatigue defects caused by heavy load is a common engineering challenge for all operating heavy-haul railway transport countries, and the wheel-rail wear of curve segment is particularly serious [1]. From the actual operation results of Chinese Da-Qin and Shuo-Huang coal transport lines, with the increase of axle load, the side abrasion, corrugation and peeling and dropping of rail occurred often, and the damage of wheel and rail was significantly increased [2-3]. Predictably that the wheel-rail wear will be more serious with the increase of axle load to 27-30t in China.

Aiming at the wheel-rail abrasion, many scholars and engineers have conducted a lot of researches and experimental explorations, and made some certain achievements [4-7]. However, most of researchers focused on the high-speed railway and urban rail system in China [8-12], paid less attention to the heavy-haul railway, while which had more serious wheel-rail abrasion problems. Besides, most of the dynamic researches were usually simulated by foreign commercial software such as SIMPACK, NUCARS or UM etc [13-19].

The wheel-rail abrasion is caused by many factors, such as wheel-rail matching profile, wheel-rail contact state, parameters of vehicle and track etc., it is the result of the comprehensive interaction between the vehicle and track, so it is necessary to analyze from the perspective of overall vehicle-track coupled system, while it has little effects by analyzing the performance of vehicle or track separately. Therefore, based on the actual structures of 27t axle load freight wagon and heavy-haul track in China, the vehicle-track coupled dynamic model and the mathematical model of curved track were established, and applying the Hertz nonlinear contact theory and Kalker linear wheel-rail creep theory [20], adopting the fast numerical integration method [21], the curving performance of the heavy load vehicle was simulated to mainly explore the influence law of geometric parameters such as curve radius, transition curve length and superelevation of outer rail on wheel-rail wear, to provide certain technical support for the design and type selection of the heavy-haul railway vehicle and track in

Received 28 March 2021; Accepted 26 May 2021

China.

1 Simulation model

1.1 Heavy-haul vehicle-track coupled dynamic model

$C80_F$ type wagon is a 27t axle load gondola developed in China, mounted with two sub-frame radial bogies. The front and the rear wheelset of the bogie are connected with a u-shaped sub-frame and an elastic crossing bar. Its primary suspension adopts a rubber-metal pad, and the second suspension consists of several sets of two-stage stiffness springs and a combined friction wedge [22]. Considering the specific structural characteristics of heavy-haul freight car and its nonlinear links, the vehicle-track coupled dynamic model is established and shown in Fig. 1.The model is mainly composed of the car body, bolsters, side frames and wheelsets. Between the car body and the bolsters, the rotary moments of the central plates and the friction moments of the elastic side bearings are considered. The whole vehicle suspension system consists of the primary and the secondary suspension system. The primary suspension is mainly the three-direction stiffness and damping provided by the rubber-metal pad, the secondary suspension is the three-direction stiffness provided by the two-stage stiffness springs and the nonlinear friction damping characteristics of the combined wedge, the connecting crossed rod is simulated with the longitudinal and lateral stiffness. The track is simulated as a three-layer continuous elastic discrete points supporting infinite long Euler beam model. Considering its vertical, transverse and torsional degrees of freedom of the rail, the sleeper is regarded as a rigid body, considering its vertical, lateral and rotation movement, the ballast is discretized into rigid mass blocks, connected by the shear stiffness and shear damping elements, and the ballast bed and roadbed are connected by linear springs and damping elements, and only consider the vertical vibration of the ballast bed. The whole degree of freedom of the vehicle-track coupled model is 56 (shown in Table 1). The detailed descriptions of symbols in Fig. 1 and Table 1 can be found in the reference [23].

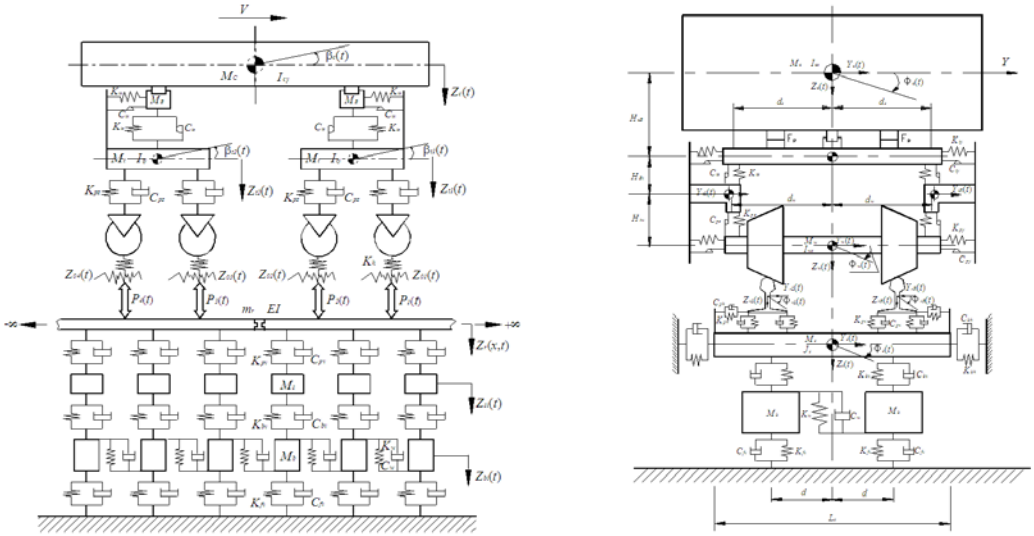

(a)Front view (b) End view

Fig.1 Heavy-haul vehicle-track coupled dynamic model

Table 1 DOFs of heavy-haul vehicle-track coupled dynamic model

DOFs	Longitudinal	Lateral	Vertical	Rolling	Yawing	Pitching
Car body	Xc	Y_c	Z_c	φ_c	ψ_c	β_c
Bolster(i=1,2)	X_{Bi}	Y_{Bi}	Z_{Bi}	φ_{Bi}	ψ_{Bi}	—
Side-frame(i=1,2)	$X_{t(L,R)i}$	$Y_{t(L,R)i}$	$Z_{t(L,R)i}$	—	$\psi_{t(L,R)i}$	$\beta_{t(L,R)i}$
Wheel set(i=1~4)	—	Y_{wi}	Z_{wi}	φ_{wi}	ψ_{wi}	β_{wi}
Rail	—	$Y_{r(L,R)}$	$Z_{r(L,R)}$	$\varphi_{r(L,R)}$	—	—
Sleeper	—	Y_s	Z_s	φ_s	—	—
Ballast	—	—	$Z_{b(L,R)}$	—	—	—

1.2 Mathematical model of heavy-haul curved track

The typical curved track plane is shown in Fig. 2 [25], generally is composed of straight line--transition curve--circular curve--transition curve--straight line. When the vehicle enters the curve with a radius of R_0 (shown in fig. 2) from a straight line, the curvature changes from zero to k_0 (k_0=1/R_0), and an outward inertial centrifugal force will appear. To reduce or balance this centrifugal force, a certain superelevation (h_0) of the outer rail is needed. In order to maintain the smoothness of vehicle curve negotiating and

alleviate the impact caused by the superelevation of the outer rail and the sudden change of the curvature, between the straight line and the circular curve, a space curve (called transition curve) with continuous changes of curvature and superelevation is usually provided. The transition curve is generally divided into the cubic and the high order spiral line, while Chinese railway usually adopts the cubic type as the transition curve [16].

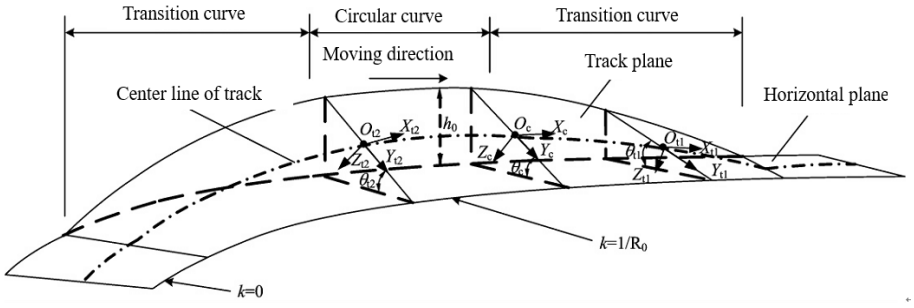

Fig.2 Schematic diagram of curved track

The linear slope requires both the superelevation (h) of outer rail and the curvature (k) of transition curve should change linearly with the length of transition curve, means that:

$$h = \frac{l}{l_s} h_0 \tag{1}$$

$$k = \frac{l}{l_s} k_0 = \frac{l}{l_s R_0} \tag{2}$$

Where l is the vehicle running distance on transition curve, l_s is the total length of transition curve, h_0, R_0 and k_0 are the superelevation, radius and curvature of the circular curve. Then, the plane equation of the cubic spiral line can be derived as:

$$\begin{cases} x = l - \dfrac{l^5}{40R^2 {l_s}^2} \\ y = \dfrac{l^3}{6Rl_s} - \dfrac{l^7}{336R^3 {l_s}^3} \end{cases} \tag{3}$$

At the junction point of transition and circular curve:

$$\begin{cases} x_0 = l_s - \dfrac{{l_s}^3}{40{R_0}^2} \\ y_0 = \dfrac{{l_s}^2}{6R_0} \end{cases} \tag{4}$$

Where R is the radius of transition curve.

From the force analysis of the vehicle passing through a curve, the formula of the superelevation of outer rail is given by:

$$h = \frac{s}{g}\frac{v^2}{R} \tag{5}$$

Where s is the gauge of the track, g is the constant acceleration of gravity. For Chinese 1435mm standard gauge, while the units of speed v, superelevation h and radius R are respectively km/h, mm and m, then the formula can be simplified as:

$$h \approx 11.8\frac{v^2}{R} \tag{6}$$

If the actual superelevation is greater or less than this calculated value, then it is considered that the vehicle runs at an excessive or inadequate superelevation. *Chinese railway works regulations* rules that the maximum designed superelevation is 150mm.

Due to the superelevation of outer rail and the curve curvature change, the track plane will be distorted, to cause the additional longitudinal, lateral, vertical, rolling, yawing and pitching movement of the rigid body parts of vehicle, lead to relative displacement and relative velocity happen at each suspension point, thus to affect the suspension forces [24-25].The specific calculation method of relative displacement and relative velocity caused by the variations of superelevation and curvature is detailed in the ref. [24].

2 Simulation conditions and calculation method

Based on the specific structure and actual parameters of 27 t axle load freight wagon mounted with two sub-frame radial bogies, the simulation parameters are chosen according to its actual parameters, e.g. the wheel profile is LM wear type tread, and the diameter of wheel is 915mm. The track parameters are obtained using the parameters provided in appendix 4 of ref. [20]. Curve parameters are chosen according to the first level mix railway of passenger and cargo transport in China, and some requirements for Chinese new heavy-haul railway line in *the design specifications for heavy-haul railway* (TB 10625-2017). In order to clearly compare the influence of curve geometric parameters on wheel-rail wear, the track geometric irregularities excitation is not considered in the calculation. The detailed simulation conditions is shown in Table 2.

Table 2 Simulation conditions of the curve line

Simulation conditions	Curve radius (m)	Superelevation of outer rail (mm)	Length of transition curve (m)	Length of circular curve (m)	Running speed (km • h^{-1})
1	350~1400	$h = 11.8v^2/R$	75	50	
2	800	95	20-150	50	80
3	800	5-150	75	50	

Due to a large number of nonlinear factors and degrees of freedom in the vehicle-track coupled model, it is difficult to solve analytical solutions directly. Therefore, using the numerical integration method is a common effective way. Based on the vehicle-track coupled dynamic model and curve mathematical model, the forces on the moving parts of the system were analyzed and the motion equations of the parts were established. The wheel-rail normal forces are solved by Hertz nonlinear contact theory, the wheel-rail creep forces/torques are solved by Kalker linear creep theory, and revised by "Shen's theory" [20], while the suspension forces are calculated by the system coordinate transforming method [24]. The wheel-rail wear can be compared and analyzed with the common evaluation indexes such as the wheel-rail vertical force, wheel-rail lateral force and wheel-rail wear power (defined as the product of wheel-rail creep force and wheel-rail creepage) [20].

3 Simulation results

3.1 Effects by the curve radius

Fig.3 shows the comparative variations of some dynamics indicators between the leading and trailing axle of the 27t axle load sub-frame radial bogie as the curve radius increases. As shown in Fig.3 (a), the lateral displacement of wheelset decreases as the curve radius increases, and that of the leading axle is slightly greater than that of the trailing one(< 1mm). The directions of angle of attack of the leading and trailing axle are opposite, the amplitudes of them become smaller especially within the curve radius of 600m as the curve radius increases, but after the curve radius is greater than 600m, they change very slightly (Fig. 3(b)). The lateral axial force and vertical force decrease as the curve radius increases, especially change very fast within the curve radius of 500m. After that, the variations and magnitudes of the lateral and vertical force of the both axles have only slightly differences, but the values of the trailing axle are corresponding greater than that of the leading axle at the whole range (Fig.3 (c) and (d)). Fig.3 (e) and (f) indicate that the wheel/rail wear decreases as the curve radius increases, and the magnitude of decline is more significant on more severe curves. However, after the curve radius is greater than 1,000 m for the leading axle, 500m for the trailing axle, the changes slow down obviously. Comparing the two wear indexes between the leading and the trailing axle of the bogie, both of the leading axle are always greater than that of the trailing one, which means that the leading wheelset will wear faster and have relatively shorter service life.

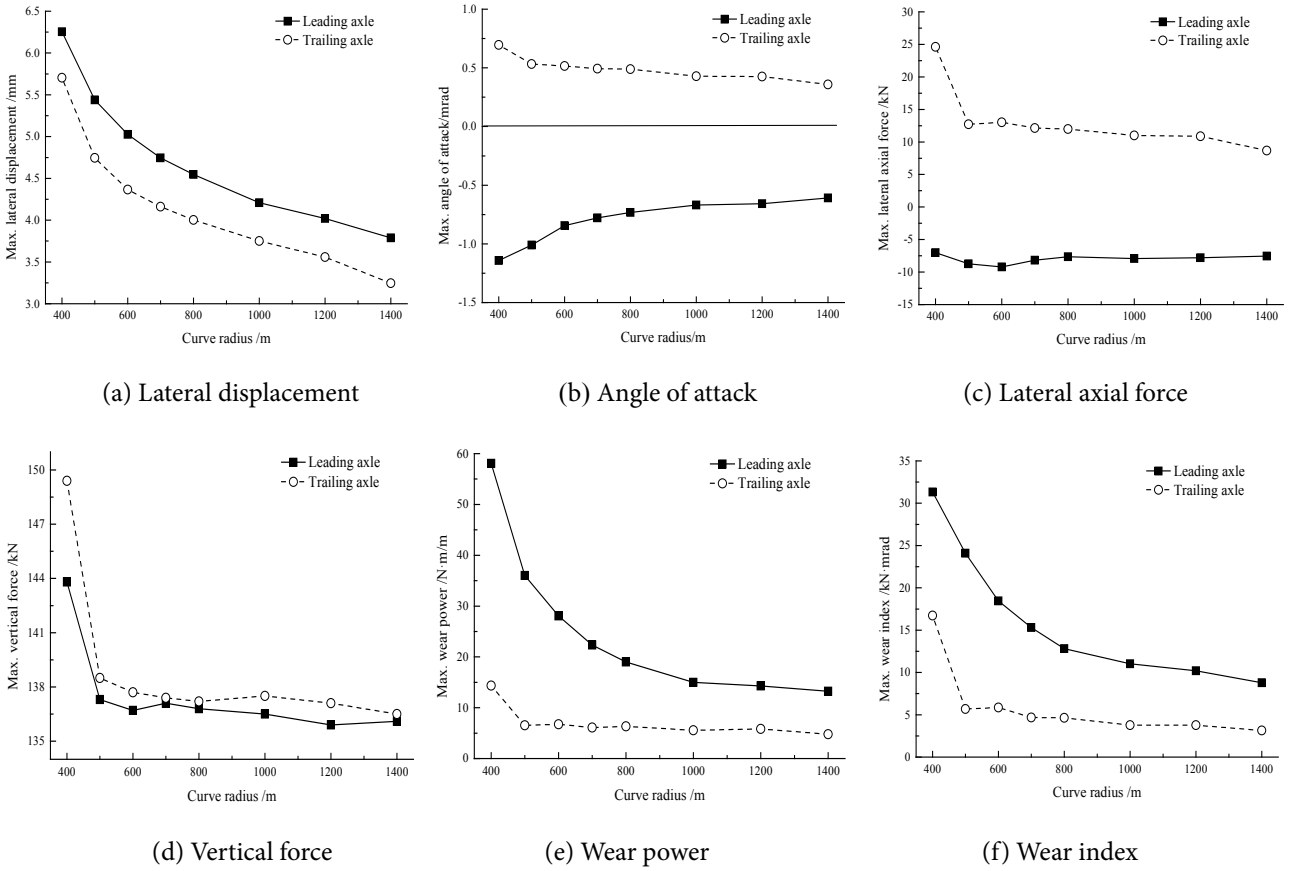

(a) Lateral displacement (b) Angle of attack (c) Lateral axial force

(d) Vertical force (e) Wear power (f) Wear index

Fig.3 Effects of curve radii to wheel-rail dynamic interaction

3.2 Effects by the transition curve length

The influence of length of transition curve on the dynamic interaction of the bogie is shown in Fig.4. The lateral displacements and the angles of attack of both the leading and the trailing wheelset decrease as the length of transition curve increases within 60m, but they change

little after the length is greater than 60m (Fig.4 (a) and (b)). The lateral axial forces of both wheelset decrease slowly with the increase of the length of transition curve. But after the length of transition curve is greater than 90m, the lateral axial force of the leading axle change little, and that of the trailing has very slightly variations when the length is longer than 30m (Fig.4 (c)). The length of transition curve has much effects on the vertical force: as seen from Fig. 4 (d), the vertical forces of the leading and the trailing wheelset decrease rapidly with the increase of length of transition curve especially at the range of 45m and 30m separately, but they decrease slowly after the length is greater than 90m and 60m accordingly. The wear power and the wear index of both wheelsets continuously decrease with the increase of the length of transition curve, and they decrease relatively faster within the transition curve length of 90m. Between the two wheelsets, the wheel/rail wear of the leading wheelset is obviously larger than that of the trailing, indicates that the leading wheelset of the bogie is easier to be worn (Fig.4 (e) and (f)). From the above, it can be concluded that properly increasing the transition curve length within a certain range is useful to reduce the wheel/rail wear. To this sub-frame radial bogie, generally the minimal length of transition curve should be 90m, and preferably not less than 60m even in a difficult engineering practice.

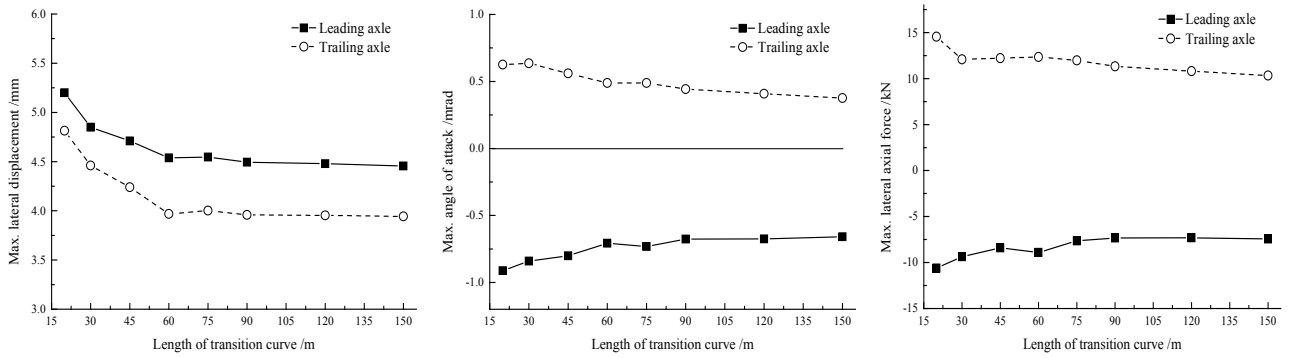

(a) Lateral displacement (b) Angle of attack (c) Lateral axial force

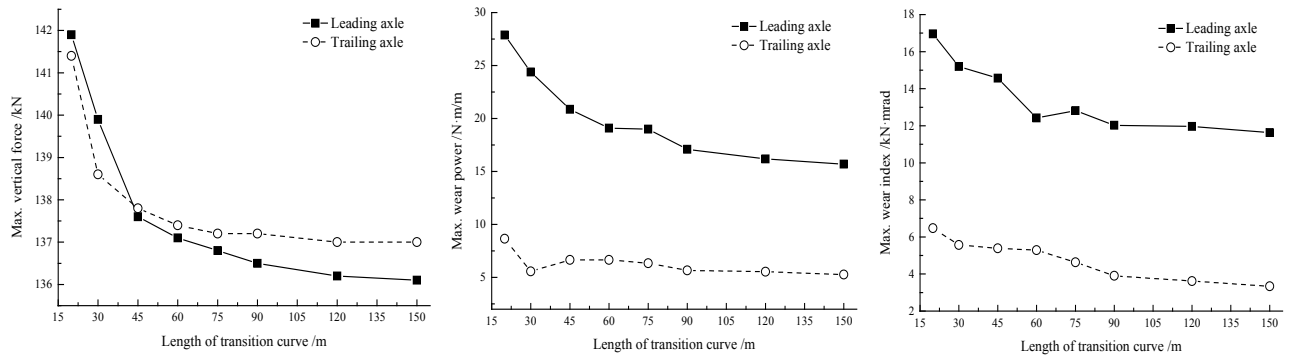

(d) Vertical force (e) Wear power (f) Wear index

Fig.4 Effects of transition curve length to wheel-rail dynamic interaction

3.3 Effects by the superelevation of outer rail

The influence of rail superelevation on dynamic interactions is shown in Fig.5. It can be seen that: the lateral displacement of wheelset decreases as the rail superelevation increases, that of the leading axle is larger than that of the trailing one, and the higher the superelevation, the greater the difference (Fig.5 (a)). With the increase of rail superelevation, the angle of attack of the leading axle increases, while the trailing one decreases accordingly, and they almost both change with a similar linear gradient (Fig.5 (b)). The two changing curves of the lateral forces of the leading and the trailing axle are shown as an approximately "X" shape (Fig.5(c)), that of the leading axle decreases with the increase of rail superelevation within 65mm (deficient superelevation -30mm), then converts to rise continuously, while that of the trailing axle continuously decreases. Within the deficient superelevation range, the lateral force of the trailing axle is greater than that of the leading one, but at the range of surplus superelevation, the lateral force of leading axle is larger conversely. The vertical force curves of the leading and the trailing axle are shown as a "V" shape (Fig.5 (d)), each curve has a turning point, before this point, the vertical force decreases with the increase of superelevation, after this point, it converts to increase. Thus, nearly at the turning point, the vertical force is minimal. For the leading axle, the turning point is about at the deficient superelevation of -15mm, for the trailing one, it is about at the zero (equilibrating superelevation). The wear power

curve with the superelecation shows a parabolic shape, at the range of deficient superelevation, the wear power of the leading decreases slowly, while that of the trailing decreases faster relatively; at the range of surplus superelevation, that of the leading begins to increase, and changes obviously rapidly, while that of the trailing converts to increase at the surplus superelevation of 20mm (Fig.5 (e)). At the range of deficient superelevation, the wear index of the leading axle increases slowly with the increase of the superelevation, but that of the trailing axle decreases significantly. At the range of surplus superelevation, the wear index of the leading increases faster, that of the trailing decreases slowly, even when the surplus superelevation is greater than 20 mm, it begins to increase with the superelevation (Fig.5 (f)). Therefore, comprehensive analysis of all these evaluating indicators, much too deficient or surplus superelevation can both worsen the wheel/rail interactions, but a proper deficient superelevation (about -20~0mm) is relatively beneficial to lessen the wheel/rail dynamic response, especially to that of the leading wheelset.

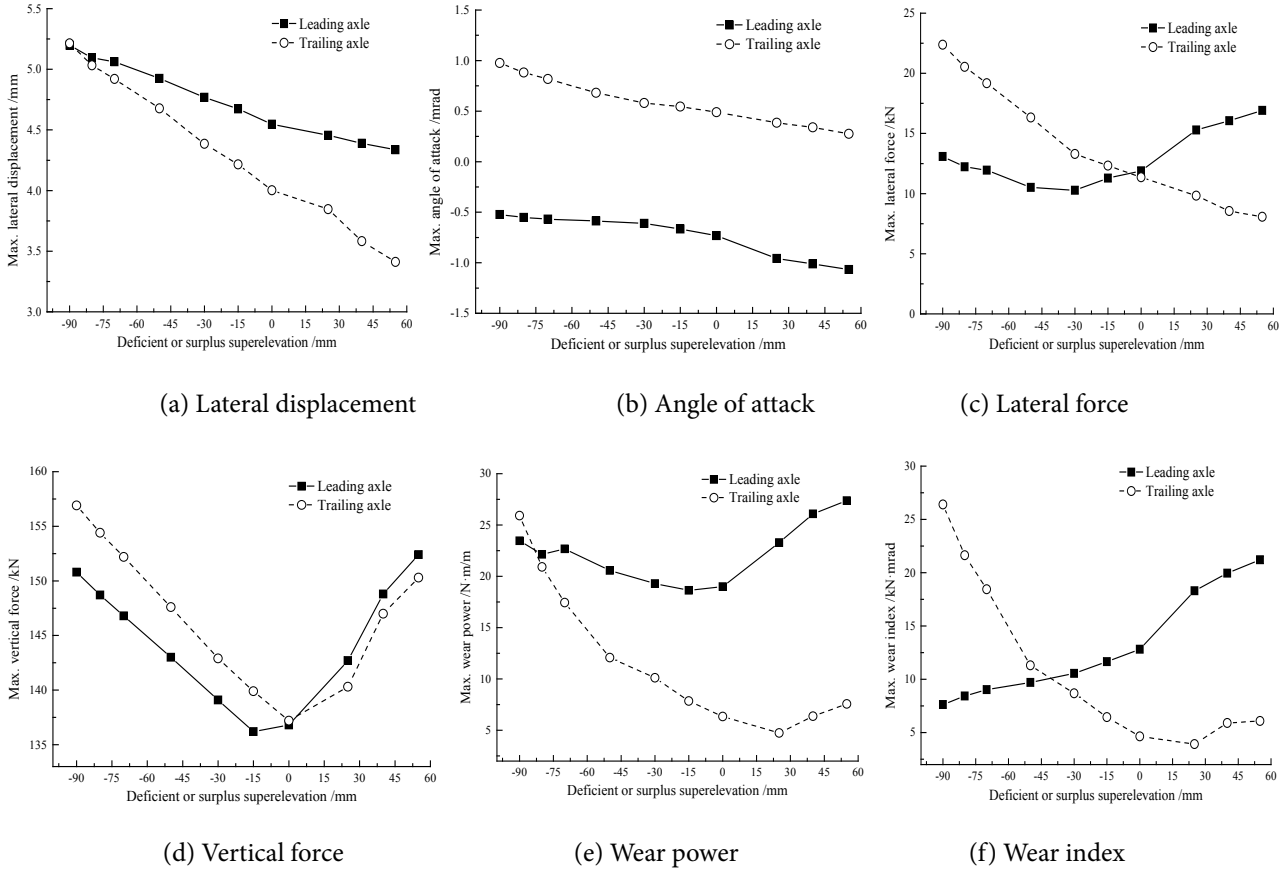

(a) Lateral displacement (b) Angle of attack (c) Lateral force

(d) Vertical force (e) Wear power (f) Wear index

Fig.5 Effects of superelevation of outer rail to wheel-rail dynamic interaction

4 Conclusions

By establishing the vehicle-track coupled dynamic model and the curve track mathematical model, adopting numerical calculation method to program to simulate the influence of geometric parameters such as curve radius, transition curve length, and superelevation of outer rail on the dynamic interaction performance of the heavy-haul freight wagon, and to analyze and evaluate the curving performance of vehicle by the wheel-rail vertical force, wheel-rail lateral force and wheel-rail wear power. Based on the calculation results, the following conclusions can be drawn:

(1) Increasing the curve radius can reduce the wheel-rail wear, but with the increase of the curve radius, the effect is gradually weakened. According to its influence level and effect, the curve radius can be divided into three segments: the sharply descending segment (<400m), transition segment (400~800m) and moderating segment (>800m).

(2) Too small transition curve length (e.g. <20m) will arouse vehicle vibration at the transition-circle connection point, thus increase the wheel-rail dynamic interaction and wheel-rail wear. Increasing the transition curve length can reduce the wheel-rail wear, however, when the length is greater than 50~60m, its change has little influence on the wheel-rail wear.

(3) Too large deficient or excessive superelevation will increase the wheel-rail dynamic interaction and wear, but an appropriate deficient superelevation (e.g. <20mm) is conducive to reduce the wheel-rail wear, which is consistent with the engineering practice of setting a certain deficient superelevation value.

Acknowledgments: This work was supported by the National Natural Science Foundation of China (No.

51965016), the National Key Research & Development Funded Project (No. 2016YFB1200501) and the Doctoral Research Start-up Funded Project (No. MY2015B009).

References

[1] Zhai Wanming, Zhao Chunfa. Frontiers and Challenges of Sciences and Technologies in Modern Railway Engineering [J]. Journal of Southwest Jiaotong University, 2016,51(2) : 209-226.

[2] Hu Haibin, Lv Kewei, Shao Wendong, etc. Research on Wheel Wear of Freight Cars on Datong-Qinhuangdao Railway Line [J]. Journal of China Railway Society, 2010, 31(1): 30-37.

[3] Chen Zhaoyang, Zhang Yinhua, Liu Fengqing, etc. Analysis on the Formation Cause of Spalling and Damage of the Heat-Treated Low Rail on Shuohuang Railway Curve [J]. China Railway Science, 2008, 29(4): 28-34.

[4] Krzysztof Zboiński, Piotr Woźnica. Optimization of the Railway Transition Curves' Shape with Use of Vehicle-track Dynamical Model [J]. THE ARCHIVES OF TRANSPORT, 2010, (3) : 387-407.

[5] SADEGHI J., AKBARI B. Field investigation on effects of railway track geometric parameters on rail wear [J]. Zhejiang University SCIENCE A, 2006, 7(11):1846-1855.

[6] Lei Wu, Xuesong Yao, Joel VanderMarel, etc. Effects of curve radius and rail profile on energy saving in heavy haul achieved by application of top of rail friction modifier [J]. Wear, 366-367(2016)279-286.

[7] Kaiyun Wang, Chao Huang, Wanming Zhai, etc. Progress on wheel-rail dynamic performance of railway curve negotiation [J]. Journal of Traffic and Transportation Engineering(English Edition), 2014, 1(3) :209-220.

[8] Wei Qingchao, Zang Chuanzhen, Lie xinlu, etc. Dynamic Influence of Profile Parameters on LIM Train [J]. Journal of Railway Engineering Society. 2018, (1):42-48.

[9] Qian Yao, Wang Ping, Su Qian, etc. Effect Analysis of Rail Cant on the Wheel-rail Contact Behavior of High-speed Railway [J]. Journal of Railway Engineering Society. 2018, (3):18-25.

[10] Chen Peng, Gao Liang, Hao Jianfang. Simulation study on parameters influencing wheel /rail wear in railway curve [J]. China Railway Science, 2007, 28(5): 19-23.

[11] Zhou Suxia, Xue Rui. Influence of transition curves act on subway wheel-rail wear [J]. Journal of Beijing Jiaotong University, 2015, 39(3): 24-29.

[12] Xiong Jiayang, Cao Yabo, Xiao Xinbiao, Wen Zefeng, Jin Xuesong. Effect of curved track parameters on curving performance of linear induction motor metro vehicle [J]. Journal of Mechanical Engineering, 2017, 53(18): 131-137.

[13] Zhao Guotang, Zeng Shugu. Effect of curve radius and off-balance superelevation on side wear of high rail on curved track [J]. China Railway Science, 1995,16(3) : 90-95.

[14] Li Wei, Ma Zhaiguo, SI Daolin. Study on influence of the curve geometrical parameters to rail wear [J]. Railway Engineering, 2013, (6) :130-134.

[15] Li Hengli, Li Fu, Fu Maohai, Huang Yunhua. Influence of curve geometric parameters on the curve negotiation performance of freight car bogies [J]. China Railway Science, 2008,29(1) : 70-75.

[16] Zhang Jianquan, Huang Yunhua, Li Fu. Influence of transition curves on dynamics performance of railway vehicle [J]. Journal of Traffic and Transportation Engineering, 2010, 10(4): 39-44.

[17] Chen Xu. Key influences of curve superelevation on design of railway engineering [J]. Journal of Railway Engineering Society, 2011, (11) : 6-12.

[18] Gao Liang, Wang Pu, Cai Xiaopei, XIAO Hong. Superelevation modification for the small-radius curve of Shen-shuo railway under mixed traffic of passenger and freight trains [J]. Journal of vibration & shock, 2016, 35(18) :222-228.

[19] Sun Haifu. Study on the minimum curve radius of heavy haul railway [J].Journal of Railway Engineering Society, 2016, (1): 36-41.

[20] Zhai Wanming. Vehicle-Track Coupled Dynamics(Fourth Edition) [M].Beijing: Science Press, 2015.

[21] Zhai W M. Two simple fast integration methods for large-scale dynamic problems in engineering [J]. International Journal for Numerical Methods in Engineering, 1996, 39(24):4199-4214.

[22] Wu Chang, Wang Yungui, Luo Hanjiang. Development of 27t axle load sub-frame radial bogie. Rail Transportation Equipment and Technology, 2014, (3) : 5-7.

[23] Yang Chunlei. Research on Matching Relationship between Axle Load and Running Speed of Heavy Haul Freight Wagon [D]. Chengdu: Southwest Jiaotong University, 2013.

[24] Wang Kaiyun, Zhai Wanming. Calculation of displacements of vehicle suspension on tangent and curved tracks [J]. Journal of Southwest Jiaotong University, 2003, 38(2) : 122-126.

[25] Liu Pengfei, Zhai Wanming, Wang Kaiyun, Feng Quanbao. The dynamic Characteristics of Suspension System and Wheel Load for Rolling Stock Passing through Transition Curve [J]. China Railway Science, 2013, 34(1): 67-73.

Viser Technology Pte. Ltd.
Mechanical Engineering Science
DOI: 10.33142/mes.v3i1.4337

Research Article Open Access

Deformation Analysis and Fixture Design of Thin-walled Cylinder in Drilling Process Based on TRIZ Theory

Fulin WANG[1]*, Bo SHENG [2] , Yongwen WU[1], Jiawang LI[1], Zhou XU[2], Zhaoxia ZHU[2]

1. College of Mechanical and Vehicle Engineering, Hunan University, Changsha, Hunan;
2. AECC South Industry Limited company, Zhuzhou, Hunan

***Corresponding Author:** Fulin WANG, College of Mechanical and Vehicle Engineering, Hunan University, Changsha ,China; wangfulin_01@163.com*

Abstract:
Thin-walled cylindrical workpiece is easy to deform during machining and clamping processes due to the insufficient rigidi. Moreover, it's also difficult to ensure the perpendicularity of flange holes during drilling process. In this paper, the element birth and death technique is used to obtain the axial deformation of the hole through finite element simulation. The measured value of the perpendicularity of the hole was compared with the simulated value to verify then the rationality of the simulation model. To reduce the perpendicularity error of the hole in the drilling process, the theory of inventive principle solution (TRIZ) was used to analyze the drilling process of thin-walled cylinder, and the corresponding fixture was developed to adjust the supporting surface height adaptively. Three different fixture supporting layout schemes were used for numerical simulation of drilling process, and the maximum, average and standard deviation of the axial deformation of the flange holes and their maximum hole perpendicularity errors were comparatively analyzed, and the optimal arrangement was optimized. The results show that the proposed deformation control strategy can effectively improve the drilling deformation of thin-walled cylindrical workpiece, thereby significantly improving the machining quality of the parts.

Keywords: *Thin-walled cylindrical parts; Fixture; Deformation analysis; Drilling; TRIZ theory*

1 Introduction

The thin-walled cylindrical parts made by high-temperature alloy have been widely used in the aerospace due to their compact structure, high specific strength and high temperature resistance. However, the thin-walled cylindrical parts have weak rigidity and poor processing characteristics, which make them easily deformed during the manufacturing process, and it is difficult to guarantee the machining accuracy. Therefore, it is of great significance to analyze and control the deformation of this typical kind of parts during machining. Some methods are commonly used to control deformation of parts, such as improving the structural machinability of the workblank, improving the fixture scheme, revising the tool path, and optimizing the process parameters, etc [1-8]. Among them, with properly positioning, clamping and supporting of the parts, the deformation can be effectively reduced, and the processing quality of the parts can be improved.

So far, many experts and scholars have carried out comprehensive study on the deformation control and the drilling quality of thin-walled parts, and also have achieved some research results. Wang et al. [9] established a finite element optimization model for the milling of thin-walled arc-shaped parts. With optimizing the clamping position, the elastic deformation in machining of the part was reduced. The influence of three factors such as clamping position, clamping order and loading method on the deformation of frame-type thin-walled parts in the clamping process was simulated by Dong et al. [10], and the optimal clamping scheme was selected. Qin et al. [11] analyzed the clamping deformation generated by different clamping order and position of location, optimized the clamping scheme based on the neural network and genetic algorithm, which effectively reduced the deformation of thin-walled parts. Necmettin [12] developed an improved genetic algorithm to optimize the layout of fixtures, the result showed that the deformation of part and the computational cost were obviously cut down. Selvakumar et al. [13] proposed an experimental design algorithm based on an artificial neural network to acquire the optimal fixture layout, and the maximum elastic deformation of designed part caused by the clamping force and cutting force was reduced. Croppi

Received 1 March 2021; Accepted 9 May 2021

et al. [14] proposed a fixture optimization method for drilling thin-walled parts. Based on the workpiece geometry and tool path, the optimal fixture design is obtained through the combination of finite element model, geometric error model and chatter model.

It is difficult to ensure the machining accuracy by the general drilling and clamping method for thin-walled cylindrical parts. The trial and error method is generally used in fixture design, which is inefficient and ineffective. At present, the theory of inventive problem-solving (TRIZ) has been introduced into the field of fixture design by researchers. Ren et al. [15] proposed the innovative design of reconfigurable fixture based on TRIZ conflict resolution principle. Huang et al. [16] combined axiomatic design (AD) theory with inventive problem solving (TRIZ) theory, and proposed an axiomatic design method of machining fixture scheme integrating TRIZ. The design of adaptive support fixture for thin-walled cylinder parts based on TRIZ theory in drilling process can improve the efficiency of fixture design process and enhance the scientificity of design process.

In this paper, finite element simulation analysis was performed on drilling of the flange of thin-walled cylindrical part. An adaptive fixture is developed based on TRIZ theory, which can enhance the stiffness of the parts, and thus significantly reduce the hole perpendicularity error caused by drilling deformation.

2 Drilling deformation analysis

The structure of a thin-walled cylindrical part is shown in Fig. 1. The material of part is a nickel-base superalloy and the cylinder diameter is 384 mm. The upper flange has a width of 18 mm and a thickness of 3.5 mm. The flange has a circumferential hole system with 46 small holes and four grooves. The diameter of these holes is 5 mm and the distance between the hole centers and the outside of the cylinder wall is 13 mm. The perpendicularity errors of these flange holes based on the bottom end surface of the cylindrical part are Φ0.035 mm. However, the perpendicularity of holes is out of tolerance after processing.

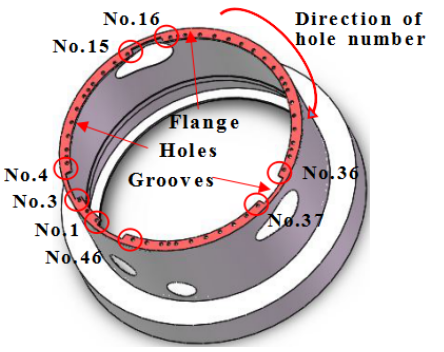

Fig. 1 The structure of a thin-walled cylindrical part

The ratio of diameter to thickness of the flange is up to 110, which is a typical weak stiffness structure. The grooves divide the flange into four independent plates with different sizes, so that the flange is easily deformed when subjected to an axial force, which further reduces the rigidity of the flange. Therefore, there is a strong correlation between the poor hole perpendicularity on the flange and processing deformation of the flange.

2.1 Finite element analysis of drilling deformation

The drilling process of thin-walled cylindrical part is simulated by ABAQUS software. The axial force and the torque are applied to 46 holes on the flange in turn. In order to simulate the actual processing condition, each force is exerted on different analysis step, and the element birth and death technique is used to remove the material in holes with the axial force adding gradually. According to the material parameters of the parts and processing parameters, it can be deduced that the drilling axial force is 152 N, and the drilling torque is 1 N·m with the formula for drilling theory [17].

Fig. 2 shows the deformation cloud image of the part during drilling the first hole. It is seen that the cylinder wall is circumferential closed structure, and the deformation of the cylinder produced by the drilling wall is much smaller than the deformation of the flange. The maximum deformation occurred near the edge of the first hole with the value of 0.61 mm. Since the drilling force acts perpendicularly on the flange end surface, the axial deformation of the flange is much larger than the tangential deformation and radial deformation. The axial deformation at the center of each small hole is shown in Fig. 3. It is seen that the deformation of these holes (Hole No.1, No.3, No.4, No.15, No.16, No.36, No.37, and No.46) at the edge of the groove shows a local peak because the groove makes the rigidity at these small holes worse.

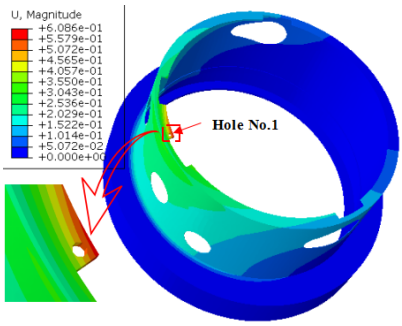

Fig. 2 The deformation during drilling the first hole

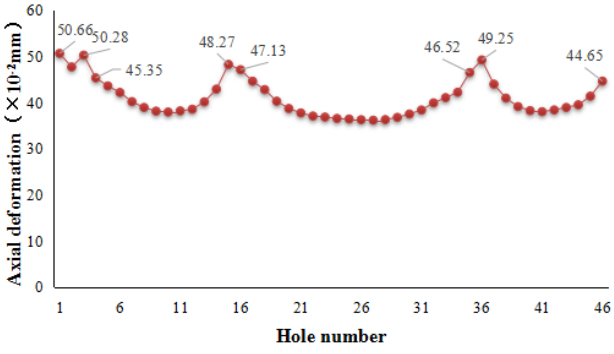

Fig. 3 The axial deformation at the center of each hole

2.2 Simplified calculation of hole perpendicularity error

Since the deformation of the cylinder wall is relatively small, the side of the flange near the cylinder wall is approximately considered as a fixed constraint. Under the action of the drilling force, the flange is bent and deformed.

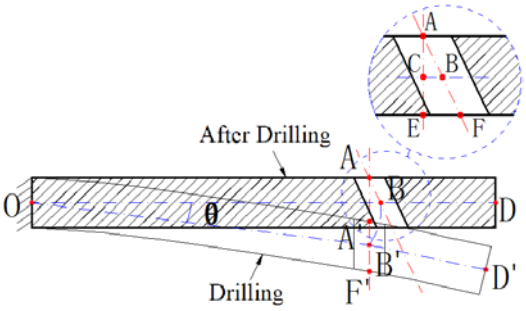

Fig. 4 The schematic diagram of drilling deformation of the flange

The drilling axial force initially acts at point A, and during the drilling process, the tool is regarded as a rigid body. Therefore, the drilling action point is always on the same vertical line. After drilling, the point A', B', F', and D' will return to the point A, B, F, and D, respectively. A'F' and AF are the centerline of the hole during drilling and after drilling. OD' and OD are the centerline of the thickness of the flange section during drilling and after drilling. The point B' is the intersection of A'F' and OD', and point B is the intersection of AF and OD. The point E is the intersection of the vertical line through the point A after drilling and the bottom edge of the flange section. The point C is the intersection of AE and OD.

As the elastic deformation disappears, the central axis of the hole is inclined. As a result that the center layer is not stretched or compressed after drilling, the lengths of the line OB and the line OB' are equal. In the case of small deformation, the line OB' can be approximated as a straight line. According to their geometric relations, the lengths of line CB and line EF can be expressed as:

$$l_{CB} = l(\sec\theta - 1) \tag{1}$$

$$l_{EF} = 2l_{CB} \tag{2}$$

Where l is the horizontal distance of the line OA, which is the radial distance between hole center and cylinder wall; θ is the angle between the line OB and OB'. Then

$$\theta = \arctan(h/l) \tag{3}$$

Where h is the vertical distance between point B and B', which can be regarded as the axial deformation of flange at holes.

The simplified calculation formula for the perpendicularity error of hole caused by the elastic deformation of flange is as follows:

$$t = 2l_{EF} = 4l(\sec\theta - 1) \tag{4}$$

2.3 Comparison of the perpendicularity errors

In the corresponding analysis step of the finite element simulation model, the axial deformation at the center of the hole is obtained. The perpendicularity error of each small hole can be obtained by equations (3) and (4). Due to the large deformation of the eight small holes at the edge of the groove, the perpendicularity errors of these special small holes are selected for analysis. The measured value of the perpendicularity error is obtained under the Coordinates Measuring Machine (CMM), and the comparison between measured and simulated values is shown in Fig. 5. The simulated value ranges from 0.031 mm to 0.039 mm, and the measured value varies from 0.037 mm to 0.047 mm. The relative error is between 9.3% and 18.2%, and the average relative error is 14.0 %. Compared with the vertical error simulation value and measured value of each hole, the simulation value is less than the measured value. In the actual drilling process, the verticality of the hole is affected by machine vibration, drilling heat and other factors. In the drilling simulation, these factors are simplified, and the influence of the main factors of drilling force and torque is only considered, so there was a certain error between the simulation value and the measured value.

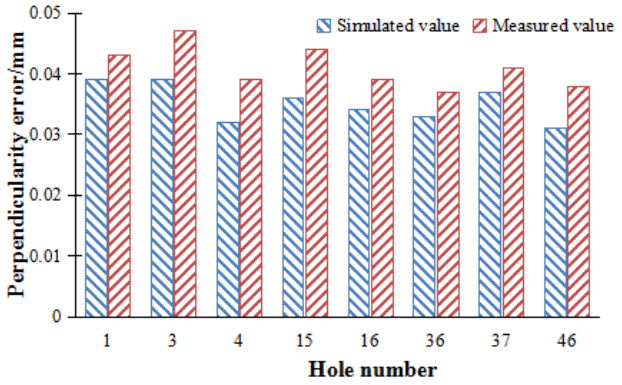

Fig. 5 The comparison of the perpendicularity errors

3 Design of fixture scheme based on TRIZ theory

Since the thin-walled cylindrical workpiece is easy to deform during the drilling process, a special fixture is necessary to reduce deformation.. TRIZ is a theory for product innovation design, which systematically put forward solutions to problems in design and effectively solve various conflicts in product design.

3.1 Analysis of deformation based on TRIZ theory

The case shell needs to be clamped in the drilling process. Since the casing is a weak rigid part, too large clamping force will lead to deformation of the workpiece, on the other hand, too small clamping will lead to vibration of the workpiece. Therefore, in order to ensure the position of the cylinder end flange in the drilling process, it is necessary to provide appropriate clamping force. Improving clamping force requires changing fixture structure, which will increase system complexity. The contradictory parameters and the original understanding of the invention can be obtained by TRIZ analysis, as shown in Table 1.

Table 1 Contradiction matrix

Improved parameters	Deterioration parameters	the principle of invention
Clamping force (10 Force)	Complexity of clamping system (36 Complexity of system)	Principle 10 : Prior action ; Principle 18 : mechanical vibration ; Principle 26 : replication ; Principle 35 : Changes in physical or chemical parameters

As shown in Table 1, Principle 10 refers to pre-action and auxiliary supports can be designed to provide pre-support for thin-walled cylinder parts to improve the stiffness of the workpiece. Principle 18 refers to mechanical vibration. According to this principle, a spring shock absorber is designed to reduce vibration during drilling process. Principle 26 refers to duplication. Replaceable fixture parts are used in the design of the drilling fixture, and the cost is reduced by copying and replacing the fixture parts that are easy to wear. Principle 35 refers to the change of physical or chemical parameters, namely the redesign of the original structure, which is not applicable to the solution of this problem and can be ignored.

3.2 Fixture design based on TRIZ

According to the above solutions, To reduce the verticality error of the small holes in the flanges of thin-walled cylinder parts, an adaptive support fixture scheme was proposed. The structure of the adjustable self-adaptive support fixture is shown in Fig. 6. The fixed support rod 4 is connected to the base of the fixture and keeps relatively fixed. When the setting screw 2 is not tightened, the spring 3 is in a compression state under the action of the gravity of the workpiece and the movable support rod 1. Tighten the locking screw 2, can make the movable support rod 1 fixed.

In this way, the supporting fixture and the inner surface of the workpiece are always attached to each other, so as to provide better support, increase the process stiffness of the workpiece, and reduce the axial deformation caused by drilling force in the processing process.

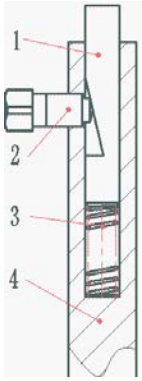

1. Movable support rod 2. Set screw 3. Spring 4. Fixed support rod

Fig. 6 The support rod of fixture

The overall design of the fixture is shown in Fig. 7. The assembly of the parts and fixtures is shown in Fig. 8. The support structure consists of a support ring 1 and four support bars 2. There are 46 avoidance holes and four avoidance grooves on the support ring. The fixture is located inside the thin-walled cylinder.

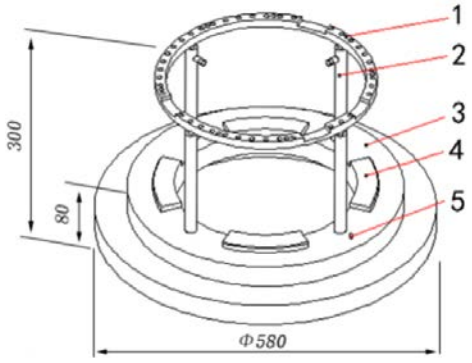

1. Support ring 2. Support rod 3. Pedestal 4. Limit **Table 5**. *Angle pin*

Fig.7 The fixture structure

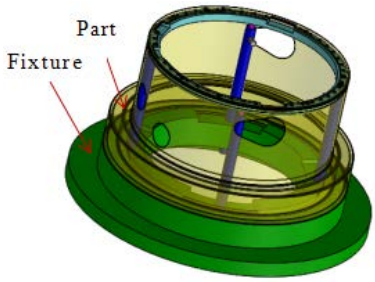

Fig. 8. The 3D assembly model of part and fixture

3.3 Numerical analysis of drilling deformation

To reduce the perpendicularity error, the axial deformation of flange must be controlled. In order to meet the requirements of processing accuracy and simplify the operation, the bottom surface of the flange needs to be tightly supported by an adaptive support fixture. When the fixture is vacant, the simplified force model is shown in Fig. 6, and the distributed force q is generated by the gravity F_1 of the support ring itself. The support ring gravity F_1 and the spring force F_3 reach a force balance. The equation is shown as follows:

$$F_1 - 4F_3 = 0 \tag{5}$$

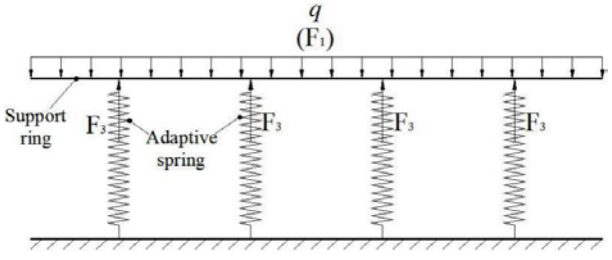

Fig. 6 Simplified force model when the fixture is vacant

When not processed, the simplified force model of the fixture is shown in Fig. 7. The distributed force q is generated by the gravity F_1 of the support ring itself and the force F_2 transmitted from the casing gravity G to the support ring. F_1, F_2 and the spring force F_3 reach a force balance. The equation is shown in Equation 6.

$$F_1 + F_2 - 4F_3 = 0 \tag{6}$$

where, $F_2 \le G$。

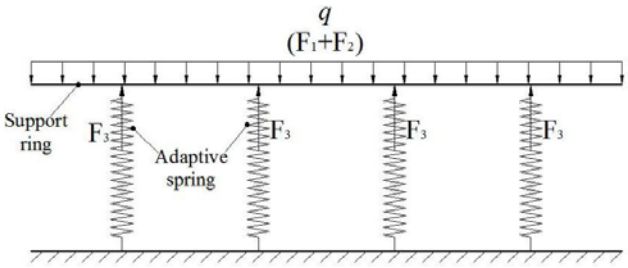

Fig. 7 Simplified force model of when not processed

According to Hook's law:

$$F_3 = k\Delta x \tag{7}$$

where, k is the spring stiffness and Δx is the deformation of the spring.

The change range of the spring deformation Δx is:

$$\frac{F_1}{4k} \le \Delta x \le \frac{F_1 + F_2}{4k} \tag{8}$$

when $F_2 = G$, there is

$$(\Delta x)_{\max} = \frac{F_1 + G}{4k} \tag{9}$$

At this time, the spring force is just balanced with the weight of the support ring and the weight of the casing, which is ideal.

The maximum working stroke h of the designed spring:

$$(h)_{\max} = \frac{G}{4k} \tag{10}$$

In this paper, the gravity of the casing is about $G = 108N$, so the maximum working stroke of the spring and its stiffness need to meet:

$$(h)_{\max} = \frac{27}{k} \tag{11}$$

4 Optimization of support layout

The position distribution of four support rods in the fixture affects the overall deformation of part. According to the idea of the uniform distribution of the support structure and the targeted support at the weak rigidity, three schemes are proposed for the position distribution of the support rods (as shown in Fig. 11). In Scheme 1, four support rods are respectively placed under the Hole No.7, No.19, No.32, and No.44, with a distribution angle of 90° between them. In Scheme 2, four support rods are respectively placed under the Hole No.2, No.14, No.25, and No.37, with a distribution angle of 90° between them. In Scheme 3, four support rods are distributed on the weak rigid position of the thin-walled cylindrical part to achieve targeted support, which are respectively placed under the Hole No.4, No.16, No.36, and No.46.

The designed support rod has good rigidity and the deformation of the support ring and its contact area is negligible, so full restraint can be exerted to these areas. The upper surface of the support ring and the lower surface of the flange of the part are set with the contact pair, and the magnitude of load and the method of application are consistent with those of the finite element model in the case of no fixture.

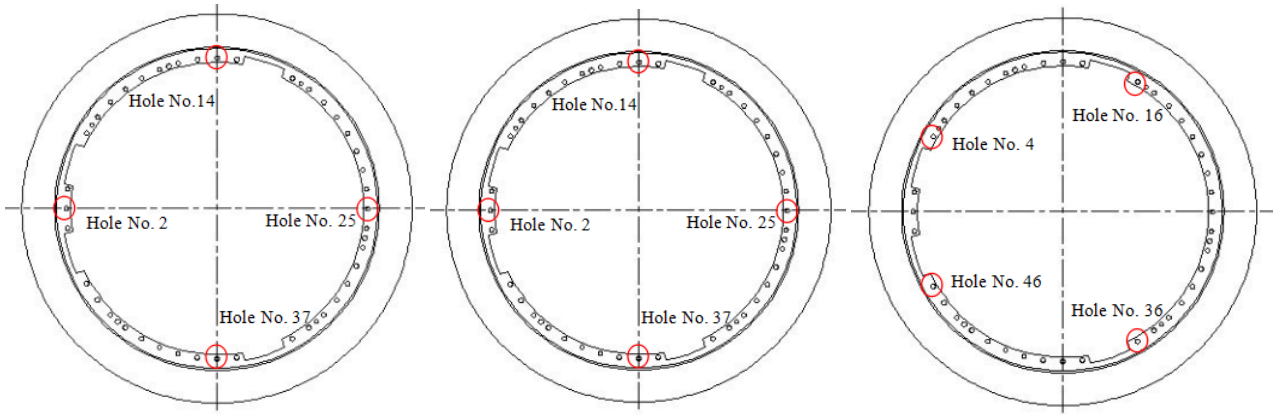

(a) The Scheme 1 (b) The Scheme 2 (c) The Scheme 3

Fig. 11 The position distribution scheme of support rods

4.1 Comparative analysis of drilling deformation in different scheme

Fig. 12 show deformation distribution contours when the Hole No.1 on the flange is drilled in three fixture supporting layout schemes. Compared with the deformation in the case of no fixture in Fig. 2, the maximum deformation was not observed near the Hole No.1 but recorded on the support ring. Due to the

different layout of the support rods, the position where the maximum deformation occurs in each scheme will be shifted to different degrees. Comparing Fig. 2 and Fig. 12, the three fixture support schemes can reduce the maximum deformation of the part from 0.61 mm to 0.1 mm, 0.03 mm and 0.04 mm respectively when drilling the Hole No.1.

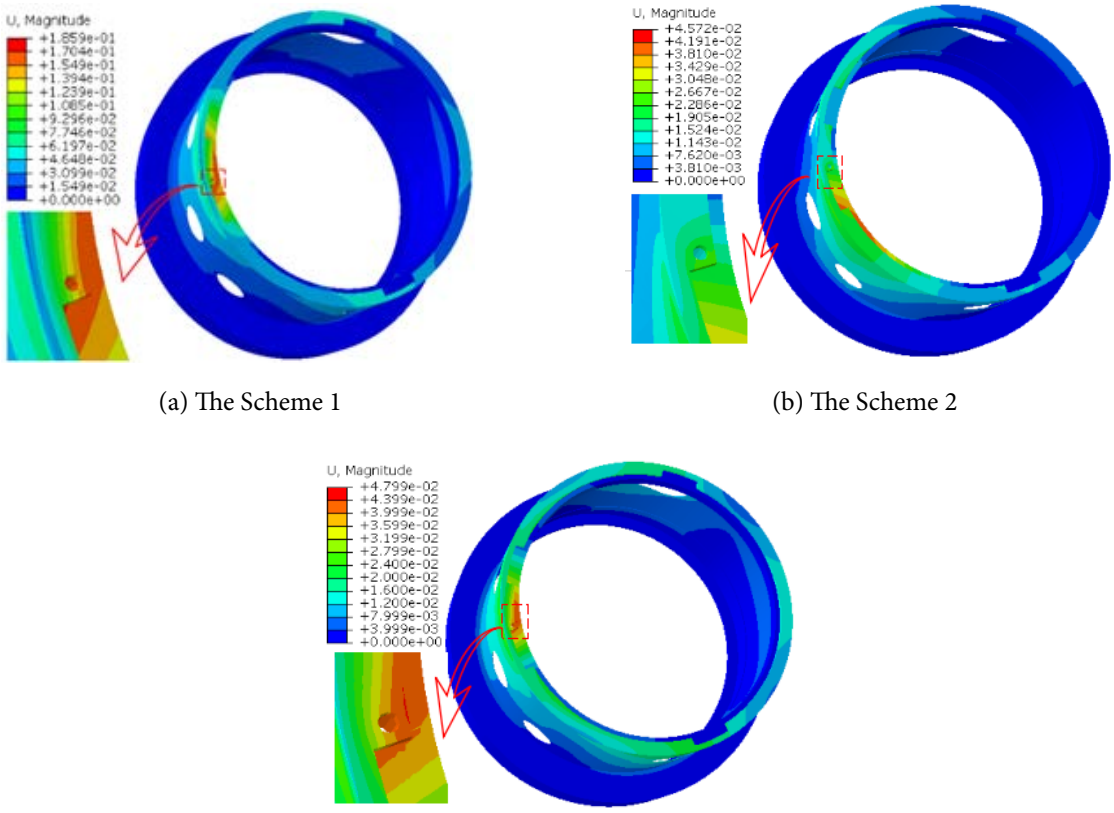

(a) The Scheme 1

(b) The Scheme 2

(c) The Scheme 3

Fig. 12 The deformation distribution contours when drilling the Hole No.1 in three fixture supporting layout schemes

Fig. 13 shows the axial deformation at the center of each small hole in three fixture supporting layout schemes. It can be seen that in these schemes, the axial deformation at the center of the hole shows a wave-like undulation respectively. The main reason is that the smallest deformation of the part occurs near the support rod during drilling process, and the deformation of the part gradually increases as the drilling position deviates from the support rod.

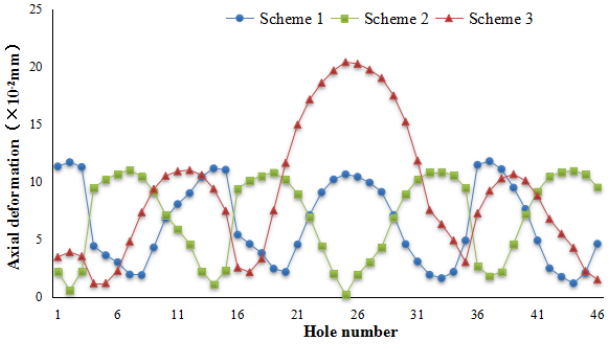

Fig. 13 The axial deformation at the center of each small hole in three fixture support schemes

Table 2 shows the comparison of axial deformation at hole center in each scheme. It can be seen that the mean value of axial deformation is 0.41 mm without fixture. The mean value of axial deformation in Scheme 1 and Scheme 2 is almost equal, decreasing to about 0.06 mm. However, the standard deviation of the axial deformation in the Scheme 2 is 1.4% smaller than in the Scheme 1, and its deformation fluctuation value is also smaller. In Scheme 3, the support rods are unevenly distributed. Its maximum axial deformation, mean value and standard deviation are 45%, 33.3% and 37% larger than those of the Scheme 2, respectively.

Table 2 The comparison of axial deformation at hole center in each scheme

	Maximum (mm)	Mean (mm)	Standard deviation
Without fixture	0.51	0.41	4.10×10^{-2}
Scheme 1	0.12	0.06	3.72×10^{-2}
Scheme 2	0.11	0.06	3.67×10^{-2}
Scheme 3	0.20	0.09	5.83×10^{-2}

4.2 Comparative analysis of the maximum perpendicularity error of holes

The maximum perpendicularity errors of the small

holes without fixture and in three fixture supporting layout schemes are calculated, as shown in Fig. 14. When there is no fixture, the perpendicularity error of Hole No.1 is the largest, which value is 3.9×10^{-2} mm. But in the other three schemes, the holes that produce the maximum perpendicularity error are Hole No.37, No.7, and No.25, respectively, and the error values are 1.5×10^{-3} mm, 1.3×10^{-3} mm, and 4.2×10^{-3} mm. Compared with the no-fixture scheme, the machining quality of the part has been improved obviously.

In Scheme 2, according to the structural characteristics of the flange surface of the part, the weak rigid position adjacent to the two grooves is taken as the starting point, and the support rods of the fixture are evenly distributed, so that the axial deformation fluctuation is small. The drilling deformation of the part is more effectively improved, and the perpendicularity error of the hole is reduced to the greatest extent. Therefore, it is determined that Scheme 2 is the optimal scheme in the proposed schemes.

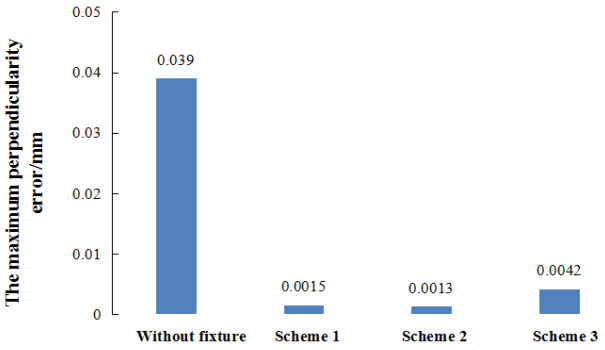

Fig. 14 The maximum perpendicularity error of holes

5 Conclusions

(1) The drilling of the flange hole of a thin-walled cylindrical part used in aerospace is analyzed by ABAQUS software. Comparing the simulated and the measured value of the perpendicularity error, the rationality of the simulation model is verified. The result shows that the drilling deformation of flange seriously affects the perpendicularity accuracy of the small hole.

(2) A drilling fixture is proposed based on TRIZ theory. The height of the supporting surface can be adjusted adaptively by the fixture. By comparing and analyzing the maximum deformation of flange in the presence or absence of fixture, it's found that the machining deformation of the thin-walled cylindrical part can enormously reduce by using the fixture, and the rationality of fixture is verified.

(3) Aiming at the position distribution of support rods in the fixture, three layout schemes are proposed and the finite element simulation is carried out. The result shows that the deformation fluctuation of scheme 2 is smallest, and the hole perpendicularity error is minimized, so that the perpendicularity accuracy of holes meets the design requirements. Therefore, the Scheme 2 is the optimal layout.

The fixture design ideas and the numerical simulation method for supporting layout optimization in this paper can provide reference for the processing deformation control of thin-walled cylindrical parts.

References

[1] Yin SH, Zhang Z, Hu T, et al. Experimental research on micro-drilling applying turbine-driven air spindle [J]. Journal of Hunan University: Natural Sciences 2017; 44(8): 1-7.

[2] Zhen LY, Wang SC. Approaches to improve the press quality of thin-walled part in NC machining [J]. Acta Aeronautica ET Astronautica Sinica 2001; 05: 424-428.

[3] Wan XJ, Hua L, Wang XF, et al. An error control approach to tool path adjustment conforming to the deformation of thin-walled part [J]. International Journal of Machine Tools and Manufacture 2011; 51(3): 221-229.

[4] Scippa A, Grossi N, Campatelli G. FEM based Cutting Velocity Selection for Thin Walled Part Machining [J]. Procedia CIRP 2014; 14: 287-292.

[5] Ivanov V, Mital D, Karpus V, et al. Numerical simulation of the system "fixture-workpiece" for lever machining [J]. The International Journal of Advanced Manufacturing Technology 2017; 91(1-4): 79-90.

[6] Karuppanan B R C, Saravanan M. Optimized sequencing of CNC milling toolpath segments using metaheuristic algorithms [J]. Journal of Mechanical Science and Technology 2019; 33(2): 791-800.

[7] Xiao GJ, Huang Y. Adaptive belt precision grinding for the weak rigidity deformation of blisk leading and trailing edge [J]. Advances in Mechanical engineering 2017; 9(10).

[8] Emel K, Babur O. Optimization of machining parameters during micro-milling of Ti6Al4V titanium alloy and Inconel 718 materials using Taguchi method [J]. Proceedings of the Institution of Mechanical Engineers, Part B: Journal of Engineering Manufacture 2015; 231(2): 228-242.

[9] Wang YQ, Mei ZY, Fan YQ. Finite element optimization of machining fixture layout of thin-walled arc part [J]. Chinese Journal of Mechanical Engineering 2005; 06: 214-217.

[10] Dong HY, Ke YL. Finite element simulation for optimal clamping scheme of thin-walled part in milling process [J]. Journal of Zhejiang University (Engineering) 2004; 01: 18-22.

[11] Qin GH, Zhao XL, Wu ZX. Optimization of multi-fixturing layout for thin-walled part based on neural network and genetic algorithm [J]. Chinese Journal of Mechanical Engineering 2015; 01: 203-212.

[12] Kaya N. Machining fixture locating and clamping position optimization using genetic algorithms [J]. Computers in Industry 2006; 57(2): 112-120.

[13] Selvakumar S, Arulshri K P, et al. Design and optimization of machining fixture layout using ANN and DOE [J]. The International Journal of Advanced Manufacturing Technology 2013; 65(9-12): 1573-1586.

[14]Croppi L,Grossi N,Scippa A, et al. Fixture Optimization in Turning Thin-wall Components[J]. Machines, 2019, 7(4): 68.

[15] REN G C, TIAN C, WANG C, et al. Research on innovative design of reconfigurable fixture based on TRIZ [J]. Modular Machine Tool & Automatic Manufacturing Technique, 2016.

[16] HUANG B, ZHOU LS, AN LL, et al. Configuration axiomatic design method for the machining fixtures integrating TRIZ. Chinese [J]. Journal of Scientific Instrument, 2017, 38(4): 1031-1040.

[17]Yang SZ, Li B, Zhou FR. Handbook of Machining Technologist[M]. Bei Jing: Machinery Industry Press, 2010.

Publisher: Viser Technology Pte. Ltd.

URL: www.viserdata.com

Add.:21 Woodlands Close, #08-18,

Primz Bizhub SINGAPORE (737854)